Protein Encapsulated Gold Nanoclusters for Biological Applications

A Thesis submitted to the University of Strathclyde for the degree of

Doctor of Philosophy

By

Ben A. Russell

Photophysics Research Group

Department of Physics

University of Strathclyde

Glasgow

2017

‘This Thesis is the result of the author’s original research. It has been composed by the author and has not been previously submitted for examination which has led to the award of a degree.’

Signed:

Date:

Abstract

Sensing and imaging at the nanoscale using fluorescence based techniques has advanced the fields of biology and medical science. However there remain shortfalls with currently used fluorescent probes. One such problem is the lack of biologically inert fluorophores which emit in the red regime of the visible spectrum with good brightness. A class of newly developed fluorophores which have shown promise in fitting the required criteria are protein encapsulated gold nanoclusters (AuNCs). They have been shown to be non-toxic, red emitting, long-lived fluorophores however their low brightness has hindered their widespread use. The complexity of protein encapsulated AuNCs' fluorescence mechanism also remains poorly understood

Fluorescence based techniques, Molecular Dynamics simulations and physicochemical characterisation techniques have been employed to uncover important information critical to improving the fluorescence characteristics of protein encapsulated AuNCs. The AuNCs nucleation site within Human Serum Albumin (HSA) has been discovered which will allow for the intelligent modification of the fluorophores with the aim of improving their fluorescence intensity and low quantum yield. The effects of AuNCs on natural protein function have also been studied; indicating that the major drug binding site of HSA is blocked upon AuNCs synthesis. Further studies of the physicochemical changes in HSA upon AuNCs synthesis uncovered that the protein adopts a dimer state which could lead to complications when using as an *in vivo* sensor. Lysozyme encapsulated AuNCs displayed similar behaviour, forming dimers after AuNCs synthesis. Interestingly, the isoelectric point of this fluorophore was found to be the same as HSA encapsulated AuNCs, suggesting that protein encapsulated AuNCs share common features. Lysozyme encapsulated AuNCs displayed similar adsorption properties as native lysozyme; suggesting that in the future, unmodified AuNCs could be used to observe the formation of lysozyme fibrils which are a major bio-marker for currently incurable brain diseases such as Alzheimer's and Parkinson's.

Acknowledgements

Firstly, I would like to say thank you to my supervisor, Dr. Yu Chen, the experience of undertaking a PhD has not only allowed me to grow as a scientist, but also as a person as well. In both accounts her guidance and support have been invaluable to me and I'll be forever grateful. Also, thank you to the Photophysics research group where I undertook my PhD. David, Olaf and Jens; I couldn't have found a friendlier group where everyone's door was always open to give advice during my stay.

Thank you also to my supervisor Dr. Paul Mulheran, our discussions were always interesting and fruitful, and without you I would not have had the opportunity to work in Krakow as an Erasmus student. Thank you also to Dr. Barbara Jachimska and her group, who were incredibly welcoming during my Erasmus study.

I must also give special thanks to Dr. Philip Yip and Dr. Karina Kubiak-Ossowska whom without their knowledge and expertise in fluorescence spectroscopy and Molecular Dynamics I would not have been able to complete this work.

Now to the friends who suffered my presence in the office every day… I couldn't have met a better bunch to suffer with during my 3 years of study! I've no doubt you'll find all the happiness and success that each one of you deserve. Chloe, Hazel Julie-ann and Alastair… don't let things get too boring once I'm gone! And of course, Gordon, it will be strange moving onto a new place without you just down the corridor. I will miss you all very much.

To my family, thank you for the support you gave me during my study, without which I would not have been able to finish. And to my amazing girlfriend, how lucky we were that our paths crossed during our studies, over the last 4 years I have met some amazing people but none as unique as you and I can't wait to see what the future brings for us both!

Publications

B. A. Russell, K. Kubiak-Ossowska, P. A. Mulheran, D. J. S. Birch and Y. Chen, "Locating the nucleation sites for protein encapsulated gold nanoclusters: a molecular dynamics and fluorescence study", *Phys. Chem. Chem. Phys.*, 2015, **15**, 21935-21941.

B. A. Russell, P. A. Mulheran, D. J. S. Birch and Y. Chen, "Probing the Sudlow binding site with warfarin: how does gold nanocluster growth alter human serum albumin?", *Phys. Chem. Chem. Phys.*,2016, **18**, 22874-22878.

B. A. Russell, B. Jachimska, I. Kralka, P. A. Mulheran and Y. Chen, "Human serum albumin encapsulated gold nanoclusters: effects of cluster synthesis on natural protein characteristics", *J. Mater: Chem. B*, 2016,**4**, 6876-6882.

B. A. Russell, B. Jachimska, P. Komorek, P. A. Mulheran and Y. Chen, "Lysozyme encapsulated gold nanoclusters: effects of cluster synthesis on natural protein characteristics", *Phys. Chem. Chem. Phys.*, 2017, **19**, 7228-7235.

Manuscripts in preparation

B. A. Russell, A. Garton and Y. Chen, "Proof that the Sudlow II binding site of human serum albumin remains available after gold nanocluster synthesis", *in submission*, 2017.

Conference Proceedings

B. A. Russell, K. Kubiak-Ossowska, P. A. Mulheran, D. J. S. Birch and Y. Chen, "Gold fluorescent probes for use in biological imaging: probing the nucleation sites for protein encapsulated gold nanoclusters", Poster Presentation, 2015, MAF 14, Wurzburg.

B. A. Russell, K. Kubiak-Ossowska, P. A. Mulheran, D. J. S. Birch and Y. Chen, "Improving gold fluorescent probes for use in biological imaging: probing the nucleation sites for protein encapsulated gold nanoclusters", Poster Presentation, 2015, Horyzonty Nauki, Krakow.

K. Kubiak-Ossowska, B. A. Russell, P. A. Mulheran, D. J. S. Birch and Y. Chen, "Understanding gold nanocluster growth within bovine serum albumin using Molecular Dynamics", Oral Presentation, 2015, Workshop Bioinformatics, Torun

K. Kubiak-Ossowska, B. A. Russell, P. A. Mulheran, D. J. S. Birch and Y. Chen, "Understanding gold nanocluster growth within bovine serum albumin using molecular dynamics", Oral Presentation, 2015, ARCHIE Meetings 21, Glasgow

B. A. Russell, K. Kubiak-Ossowska, P. A. Mulheran, D. J. S. Birch and Y. Chen, "Locating the nucleation sites for protein encapsulated gold nanoclusters: a molecular dynamics and fluorescence study", Poster Presentation, 2016, ARCHIE Workshop, Glasgow.

B. A. Russell, K. Kubiak-Ossowska, P. A. Mulheran and Y. Chen, "Observing the formation of fluorescent gold nanoclusters within proteins via molecular dynamics and fluorescence spectroscopy", Poster Presentation, 2016, Nanomaterial for Technology Workshop, Glasgow.

B. A. Russell, A. Garton, D. J. S. Birch and Y. Chen, "Probing the Sudlow binding sites in human serum albumin encapsulated gold nanoclusters for future application as a biomolecular sensor", Poster Presentation, 2017, Fluorofest, Glasgow.

Abbreviations

ADOTA – Azadioxatriangulenium

APC – Allphycocyanin

AuNCs – Gold Nanoclusters

BSA – Bovine Serum Albumin

CD – Circular Dichroism

DAPI - 4,6-diamindino-2-phenylinode

DNA – Deoxyibonucliec Acid

EEMs – Emission/Excitation Matrices

FRET – Förster Resonance Energy Transfer

FTIR – Fourier Transform Infra-red Spectroscopy

GFP – Green Fluorescent Protein

GNRs – Gold Nano Rods

HPAC – High-Performance Affinity Chromatography

HSA – Human Serum Albumin

IFP – Intrinsic Fluorescent Protein

LDV – Laser Doppler Velocimetry

MCA – Multi-Channel Analyser

MCS – Multi-Channel Scaling

MD – Molecular Dynamics

MM – Molecular Mechanics

mRNA – messenger Ribonucliec Acid

NMR – Nuclear Magnetic Resonance

PAH – Polyallylamine hydrochloride

PMT – Photo Multiplier Tube

POPOP –1,4-bis[5-phenyl(oxazolyl)]- benzene

QCM – Quartz Crystal Microbalance

TAC – Time to Amplitude converter

TCSPC – Time Correlated Single Photon Counting

TOA - tetraoctylammonium

TRES –Time Resolved Emission Spectroscopy

XPS – X-ray Photoelectron Spectroscopy

Table of Contents

1 Introduction

1.1 Current Fluorophores used in Biological Imaging and Sensing

Fluorescence based imaging and sensing has long been used in the fields of biology and medicine to further understand the complexities of protein function and biomolecule interaction[1]. With a more complete understanding of the complexities of protein-protein interactions on the nanoscale it is hoped that currently unpreventable or incurable diseases can be better understood and new approaches to treatment can be developed[2]. With this aim in mind this thesis presents work that furthers the understanding of the recently developed, protein encapsulated AuNCs type fluorophore, which has shown promise as a non-invasive probe for biological sensing and imaging.

One method of observing biological behaviour on the nanoscale is fluorescence based microscopy. It provides a powerful tool which allows users to gain a strong understanding of physiological processes which take place in living cells on the sub cellular level. Biological cells of interest are illuminated either extrinsically, by staining or attaching a fluorescent molecule (fluorophore) to the cell, or intrinsically, by exciting a fluorophore naturally present in the cell[3]. A light source, such as a monochromatic scanning laser used in confocal microscopy[4,5] or white light sources such as a Xenon arc lamps or supercontinuum lasers used in wide-field epifluorescence microscopy[6,7] is used to excite the fluorophore and the resulting emission from this molecule is captured, building an image of the surrounding cell. Typically, intrinsic fluorophores are primarily derived from the amino acids; tryptophan, tyrosine and phenylalanine but also from bio engineered Intrinsic Fluorescent Proteins (IFPs) and vitamin derivatives such as riboflavin or retinol[8]. It is preferable to use intrinsic fluorescence if possible since no modification to the cell of interest is needed and the cell remains as close to its natural state as possible[9]. Intrinsic fluorophores have been used to image a variety of different biological cells. It has been shown that it is possible to image single protein molecules which contain high amounts of tryptophan residues[10]. 24-meric hemocyanin, a repertory protein from spiders containing 148 tryptophan residues per molecule was successfully

imaged by Lippitz *et. al.* The relatively large number of fluorophores per protein allowed for images to be generated before photobleaching (the effect of damaging and altering a fluorophore via repeated excitation to the point where the original structure can no longer support the absorption and emission of a photon) of the molecule could take place. Photobleaching can therefore become a major hindrance when imaging cells with low amounts of intrinsic fluorophores present. Another technique often undertaken since the discovery of intrinsically fluorescent proteins is the manipulation and engineering of IFP labels onto proteins of interest without changing the biological function[11]. IFPs have been successfully employed in live cell imaging of many subcellular structures of plant cells. The position and dynamics of the Centromere subcellular structure was probed in living *Arabidopsis* plants utilizing histone 3-green fluorescent protein (GFP) by Fang *et. al.* This provided information on the organization of chromatin among the various cells within the organism[12]. Wang *et. al.* also utilized a GFP derivative, GFP-Talin, to label actin filaments (F-actin) within growing *Arabidopsis* plants, to visualise the cytoskeleton of cells during plant development[13]. The third type of intrinsic fluorophore commonly used for bio imaging is vitamin derivatives. Riboflavin has been used to image defects in human cornea which lead to visual impairment, allowing for a better understanding of how the irregularities in corneal shape forms[14]. The intrinsic fluorescence of collagen has also been utilized to study cells in 3D *in vitro* collagen matrices[15]. Collagen matrices are commonly used to study various cellular processes, so the matrix composition is of critical importance to mimicking *in vivo* conditions so that cell behaviour imaged in these matrices is as close to the natural behaviour as possible. By imaging these matrices using intrinsic fluorescence bio engineers can gain more information on the matrix system and alter the composition to the desired characteristics[16].

The shorter wavelength of light needed to excite some typical intrinsic fluorophores (in the UV-blue regime, 270 - 300 nm) such as tryptophan and tyrosine can be damaging to the cell and the use of two or three photon excitation, using longer wavelengths of light require a complex and costly experimental setup. The possible image depth using intrinsic fluorophores is limited due to the shorter wavelength emitted (tryptophan emission maximum of 300 - 350 nm, depending on the solvent

environment) by the fluorophore, becoming scattered by the sample. Auto fluorescence (the natural emission of light from biological structures) from other intrinsic fluorophores can also be problematic when imaging samples with a low intensity. Fluorescence from the intrinsic fluorophore of interest[17] can obscured by auto fluorescence; much in the same way light from weakly emitting stars is not visible in cities with large amounts of light pollution.

In cases where imaging with intrinsic fluorophores is not viable, the availability of extrinsic fluorophore molecules for labelling biomolecules which are bright, stable, non-toxic and can emit at different wavelengths of the emission spectrum becomes vital. Three approaches are used when imaging a biological cell with extrinsic fluorophores. Firstly, is the introduction of a fluorophore internally in a cell with no specific affinity for a site within the cell. This is the simplest of the three approaches as the only requirements of the fluorophore is that it does not react to the presence of any chemical or molecule and that it can be easily internalized and pass through the cell wall. The second technique is more complex as it deals with the imaging of particular sites within the cell or a certain molecule present. Typically referred to as "targeted bio imaging", the fluorophore utilized for this task must have an engineered functionalized surface using molecules that can recognize the part of the cell of interest. This typically culminates in the fluorophore surface being modified by attaching the correct antibody, oligomer or ligand which will attach to the correct counterpart molecule which is of interest. Thirdly is the use of extrinsic fluorophores which are sensitive to certain changes in the cellular environment such as increases in temperature, changes to pH or an increase in certain ions such as calcium or zinc ions. Typically, this approach is carried out in living cells when the function of the cell is being studied under different conditions. Multiple extrinsic fluorophores have been developed since the widespread deployment of fluorescence microscopy, however all can be categorised into two distinct different classes[18]. Either as fluorescent nanomaterials and nanoparticles such as carbon dots[19], reduced graphite oxide nanostructures[20], nanodiamonds[21], semiconductor quantum dots[22,23], up-conversion nanoparticles[24], noble metal nanoparticles[25,26] and noble metal nanoclusters[27,28]. Or as molecular fluorophores, labels and probes such as fluorescent proteins used to label cells extrinsically rather than engineered to be intrinsically

present in a cell[29], organic fluorescent dyes derived from the Fluorescein[30] or Rhodamine[31] molecular families, cyanine derived dyes[32], the negatively charged and hydrophilic Alexa Fluor dyes[33], DNA stains such as 4,6-diamidino-2-phenylindole (DAPI)[34] and Hoechst derived dyes[35]. Both categories of fluorophores have their own advantages and disadvantages during fluorescent imaging. Fluorescent nanomaterials are more robust than fluorescent dyes; they are not so easily photo-bleached and can go through more excitation and emission cycles than fluorescent dyes. Fluorescent nanomaterials are less affected by changes to their surface chemistry in comparison to some fluorescent dyes allowing them to undergo more modification for use in targeted bio imaging. The fluorescent characteristics of nanomaterials are also much easier to tune in comparison to fluorescent dyes. Fluorescence emission wavelength can be tuned by altering the dimension of a fluorescent nanomaterial[36] or by introducing more or less atoms to the unit[37]. Another current drawback is the complexity of synthesizing fluorescent nanomaterials due to their complex structure. This complexity results in lower reproducibility and higher costs in comparison to more simplistic fluorescent dyes. Some nanomaterials can be toxic to cells limiting their use without further modification; quantum dots for example generally contain some heavy metal ions such as cadium[38] in their structure. The argument of how toxic nanomaterials are to the human body is still ongoing[39]. Fluorescent dyes on the other hand have a lower toxicity in comparison to quantum dots. The fluorescence characteristics of fluorescent dyes are also better defined due to their more simplistic structure and the relative ease in which molecules can be synthesised. The fluorescence lifetime of fluorescent dyes are much shorter, in the time range of around 1 - 10 ns[40], however some examples exist with lifetimes longer than 10 ns such as Azadioxatriangulenium[41] (ADOTA). Quantum yields of fluorescent dyes on average are much higher than fluorescent nanomaterials apart from Quantum dots which can have quantum yields of 0.80 and above[42]. An example of high quantum yield can be seen from the Rh-101 Rhodamine derived dye, which has emission in the orange part of the visible spectrum and a quantum yield of 0.913 at room temperature[43] (under extreme cooling at temperatures of 153 K, Rh-101 has a quantum yield of exactly 1.000). Another example of high quantum yield molecular fluorophore is l,4-bis[5-

phenyl(oxazolyl)]-benzene (POPOP), emitting in the violet part of the visible spectrum (407 nm)[44], with a quantum yield of 0.93. Low quantum yield is a major factor limiting the use of some fluorescent nanomaterials. Up-converting nanomaterials and noble metal nanoclusters currently have low quantum yields of around 1-10 %, with much effort being made to improve this factor limiting their wider spread use in fluorescence imaging[45,46].

1.2 Fluorescent Gold Nanoclusters

AuNCs have seen much interest in the field of fluorescence imaging and sensing due to their unique properties in comparison to currently used fluorophores. AuNCs unlike larger, more commonly studied gold nanoparticles do not exhibit surface plasmon resonance absorption due to their small size (less than 2 nm diameter) but instead fluoresce in the visible/near IR region, which arises from quantum confinement effect of free electrons and the separation of discrete electronic energy levels. In comparison to traditional fluorescent dyes they have extremely long fluorescence lifetimes in the μs regime. They are also extremely stable and bio-compatible due to the low reactivity of gold itself. AuNCs also do not suffer from photobleaching like biological dyes as they are not damaged upon re-excitation making them suitable for imaging and sensing nanoscale phenomena which takes place over longer time scales. They are also easily produced in large quantities with good reproducibility in the laboratory. The fluorescence properties of AuNCs are highly dependent on their size as well as the molecule used to stabilise them. The advantage of having a large selection of ligand and proteins to stabilise the AuNCs is that it is possible to develop fluorophores with selective sensing depending on the scaffold used.

Three main approaches have been developed for the synthesis of AuNCs. The first involves etching small clusters from larger gold nanoparticles using thiol compounds, the second involves the chemical reduction of chloroauric acid and stabilised by thiol compounds, the last involves reduction and stabilisation by the ligand or protein used to stabilise the AuNCs.

Etching has seen less popularity in comparison to the reduction method, possibly due to the more complex nature of the synthesis method. Essentially the gold atoms on the nanoparticle surface are dissolved by the thiols until the reaction stops and a stable, thiol capped nanocluster is formed. For the etching to be strong the pH of the solution must be greater than 12.0 typically. This allows for the final product to be monodisperse resulting in stable clusters of uniform fluorescent features. One advantage of this method is that the size of the AuNCs can be controlled by the thiol compound used to stabilise the cluster[47].

Chemical reduction synthesis can be more complex than the other methods. Typically, a methanol solution is mixed with chloroauric acid and a thiol compound. The solution is then frozen in an ice bath for a period. A solution of sodium borohydride (sodium borohydride is a commonly used reducing agent which will reduce most organic carbonyls) is then mixed rapidly under stirring and allowed to react for another set period. The resulting precipitate can then be cleaned and centrifuged to remove unreacted materials leaving thiol capped AuNCs[48,49]. Correct temperature and mixing of the solution is critical for the reproducibility of these AuNCs as well as the separation of unused material from the final product. Another disadvantage of this method is the size distribution of gold nanocluster capped thiols; the cluster size yielded from this method is polydisperse[50]. Size of the AuNCs plays a critical role in the fluorescent characteristics; the most desirable synthesis method would produce uniform sized AuNCs, which in turn would give uniform fluorescence emission from each fluorophore complex. Another undesirable factor is the use of sodium borohydride during the synthesis. Sodium borohydride while an excellent and versatile reducing agent is highly toxic to the environment when not correctly disposed of.

Of most interest to this thesis is the reduction and stabilization of AuNCs via proteins and ligands. This method of synthesis benefits from many advantages in comparison with the two previously discussed methods. Firstly, is the simplicity of the method. It is highly reproducible and simplistic in nature due to it effectively being a “one-pot” synthesis[51]. Typically, a solution of Chloroauric acid is mixed with a protein or ligand for a short amount of time at body temperature (37 °C) before adding sodium

hydroxide and stirring at 37 °C for a period. The protein or ligand acts as a reducing agent at high pH and as such there is no requirement for a chemical reducing agent such as sodium borohydride. For a ligand or protein to reduce Au^{3+} tyrosine residues must be present within the primary structure of the molecule. Tyrosine becomes highly reducing at pH above 10.0 due to the pH being higher than the Pk_a of tyrosine. For the AuNCs to become stabilised there must also be cysteine residue in the primary structure of the ligand or protein. The cysteine residues contain sulphur molecules which readily bind to gold forming strong, stable bonds. Several proteins and ligands have been used including: insulin, pepsin, proline, human transferrin, lysozyme and serum albumin to synthesis AuNCs, each with similar fluorescent properties indicating the AuNCs is similar in size in each case[52–55]. The serum albumin family of proteins have most commonly been used to synthesise AuNCs, particularly of the bovine strain, due to their low cost, availability and the correct residue makeup of their primary structure. Serum albumin is the most abundant protein found in mammalian plasma; consisting about 50 % of all serum proteins in humans. Its function in the body is primarily that of a transport protein. Its typical cargo consists of fatty acids, steroids and thyroid hormones; however, it also shows a strong affinity for binding to several different drug molecules and less commonly metal ions such as iron. It also has a large effect on stabilizing blood pressure via colloid osmotic pressure. This in turn results in smaller mammals which typically have a lower blood pressure to have a smaller percentage of serum albumin make up the total protein count in their blood plasma. The structure of albumin is reasonably large, with a molecular weight of 65.5 kDa. The protein structure is split into 3 distinct domains; of which each is split into 2 subdomains. The protein has a mainly helical secondary structure which is supported by 17 disulphide bridges (sulphur-sulphur bonds between cysteine residues cross linking the primary structure) offering the protein rigidity. The protein is typically monomeric at natural body pH (pH 7.4) with an overall negative surface charge. In unusual cases, some diseases can cause proteins to form dimers. HSA dimerization is a symptom of liver cirrhosis in patients resulting from sulphur-sulphur bonding between two free cysteine at position 34 of the serum albumin polypeptide backbone[56].

Another protein which is studied in this body of work is lysozyme. Lysozyme is smaller in size in comparison to serum albumin with a molecular weight of 18.6 kDa and a polypeptide chain of 164 amino acid residues; however, the AuNCs produced when lysozyme is used as a stabilizing molecule are very similar in characteristics to human serum albumin (HSA) and BSA. The protein functions mainly as an anti-bacterial agent, attacking the protective cell walls of bacteria by breaking the carbohydrate chains which make up the bacteria's skin. Upon destroying a section of the bacteria's protective layer the high osmotic pressure in the centre causes the bacteria to burst. The most common and inexpensive source of lysozyme is found in the egg whites of hen eggs. In this case the lysozyme is situated so it can protect the proteins and fats which nourish the chick as it grows within the egg. Increased concentrations of lysozyme and the aggregation of lysozyme to hinder the formation of toxic amyloid-β are both indicators of the onset Alzheimer's disease in patients[57]. The increase in lysozyme concentration is believed to be triggered by the immune system to counteract increased levels of amyloid-β within the brain. Labelling lysozyme with a robust, stable fluorescent marker which is aggregation sensitive would allow for the monitoring and detection of early stage Alzheimer's.

1.3 Gold Nanoclusters in Fluorescence Imaging and Sensing

To date protein encapsulated AuNCs uses have been primarily utilized in fluorescence sensing, however there have also been some successful studies into using them also in fluorescence imaging techniques. They have been shown to be highly sensitive to heavy metal ions; which are highly polluting and toxic to both humans and the environment[58]. In particular, concern for the increased amounts of mercuric ions polluting the environment has risen[59]. Therefore, the sensing of mercuric ions, using BSA-AuNCs, has seen much development recently. Hu *et. al.* first demonstrated the sensing ability of BSA-AuNCs to be sensitive to Hg^{2+} molecules in the nM scale[60]. BSA-AuNCs can sense Hg^{2+} ions in solution as a decrease in AuNC fluorescence emission as the Hg^{2+} ion acts as an effective quencher in the presence of BSA-AuNCs. The quenching was reported to take place via a metal-metal interaction between the mercury and AuNC surface. It was

demonstrated that the water quality from different sources, based on Hg^{2+} concentrations, was clearly able to be determined using BSA-AuNCs. Shang *et. al.* developed this method of Hg^{2+} sensing as a means of imaging mercuric ions in live cells using fluorescence imaging[61]. Rather than using BSA as the encapsulating method, DHLA was used. The report successfully labelled living HeLa cells and confirmed the AuNCs were localised inside the cells via fluorescence spinning disc laser microscopy. Upon the addition of low concentrations of Hg^{2+} the fluorescence intensity of the AuNC emission was seen to decrease indicating the metal ions had been uptaken and were also localised within the HeLa cells. This study had the benefit of not only proving the ability of AuNCs to act as an in vitro label for metal ion imaging inside cells but also the relative ease at which they are uptaken by cells making AuNCs an attractive prospect as an alternative to other traditionally used fluorophores in fluorescence microscopy techniques. More recently Bothra *et. al.* have developed chemically modified cellulose paper strips utilizing pyridoxal conjugated BSA-AuNCs for cost effective and easy detection of Hg^{2+} in any water source[62].

Similar studies have been undertaken using BSA-AuNCs as a means of imaging the presence of Cu^{2+} ions in live HeLa cells[63]. Copper plays a prominent role in many biological processes; however, Cu^{2+} within cells can lead to cell apoptosis[64]. Durgadas *et. al.* found that Cu^{2+} similarly quenches BSA-AuNC emission however the mechanism is different to that of Hg^{2+}. The Cu^{2+} ion binds to the BSA surface allowing the quenching to be reversible in the presence of glycine, a Cu^{2+} chelator. This allows for selective imaging of Cu^{2+} in cells via the switching off and on of BSA-AuNC fluorescence in the presence of Cu^{2+} and glycine respectively. The early detection of Cu^{2+} in cells allows for the prevention of Prion diseases, where the presence of Cu^{2+} results in Prion protein misfolding[65]. This sensing technique is of use due to the low number of techniques available for sensing copper ions in live cells[66].

More complex sensing strategies have been developed based around encapsulating AuNCs using an active agent. Wen *et. al.* encapsulated AuNCs using active horseradish peroxidase in the detection and sensing of Hydrogen Peroxide[67].

Detection of H_2O_2 in solution is again observed via a large decrease in the fluorescence emission of the AuNC however the mechanism of quenching is different to the previous examples. Upon the addition of H_2O_2, sulphur-gold bonding between the enzyme and AuNCs are oxidised, due to the catalytic reaction of H_2O_2 by the active enzyme, causing the AuNC to detach from the enzymes and aggregate. This aggregation results in a larger gold nanoparticle forming and the loss of the AuNCs ability to fluoresce. This method was found to be able to detect H_2O_2 at the μM range, showing that active, functional encapsulation of AuNCs is possible and the method could be used as a method of monitoring biologically important targets in cells.

Cyanide ions have also been successfully detected in real world water samples by Liu *et. al.* utilising BSA-AuNCs[68]. It was shown that AuNCs can detect cyanide concentrations at a level 14 times lower than the maximum permitted level set by the world health organisation[69]. The fluorescence of AuNCs was reported to be quenched in the presence of cyanide ions due to etching of the AuNCs, stripping their gold atoms away and thus losing their ability to fluoresce. The method itself was shown to have a high specificity to the cyanide ions due to the quenching mechanism. Other ions were found to decrease the fluorescence of the AuNCs, however, they could negate the effects of other ions by introducing a chelating agent or other masking reagents which returned the fluorescence intensity of the AuNCs to their original levels. This method is novel to cyanide sensing as it does not require lengthy analysis times, nor a high level of skill[70] or difficult synthesis methods required to carry out[71], while offering a detection limit well below what is required to detect unsafe levels of cyanide in water supplies.

AuNCs have also seen use as a fluorescent detection method of trypsin, a commonly found protease[72]. Typically, the detection of high levels of trypsin in the human body can be linked to pancreatic diseases such as cystic fibrosis; therefore, detection can become useful in clinical diagnosis of these diseases. As with previous examples, trypsin is detected via fluorescence quenching of the AuNC. The quenching mechanism in this case is due to the BSA encapsulating the AuNCs being cleaved at points within the BSA peptide chain containing lysine and arginine. The method was

carried out in a clinical trial testing patient's urine samples for trace levels of trypsin. The group could differentiate between healthy participants and patients with pancreatic diseases, with a detection limit of 86 pM.

Encapsulated AuNCs have been shown to be a very simple, clean and cost effective method for sensing water pollution and in the detection of disease biological markers in clinical situations, however there is much more scope for this new type of fluorophore in fluorescence imaging due to their non-photobleaching, red emission and low toxicity properties. One recent report discusses the use of egg-white encapsulated AuNCs which could be activated in living tumor cells in vitro, while remaining switched off in healthy cells. Tian et. al. used a similar method to Hu et. al.; utilising mercury ions as a quencher to keep the AuNCs in a "switched off" state, which becomes unquenched and in a "switched on" state in the presence of intracellular reduced gluthathione[73]. Since the cancerous cells used, HepG2 are high in gluthathione[74], whereas healthy HeLa cells are not, it is possible to differentiate between the healthy and cancerous cells under fluorescence imaging; since only the cancerous cells will be seen to fluoresce. While this study was undertaken *in vitro* conditions, it proves that protein encapsulated AuNCs can determine cancerous cells from healthy cells in a non-destructive manner and shows there is possibility for their use as an early detection method for cancer.

BSA-AuNCs have also been used in a "switchable" manner to image folate expressed tumour cells based on the recovery of fluorescence in the presence of these cells. Li et. al. used folic acid to attach and modify the BSA-AuNCs surface to render the AuNC quenched and unable to fluoresce[75]. Folic acid assembled BSA-AuNCs were found to stay quenched when incubated with normal cells since no folic acid receptors are present to compete with the binding of folic acid to the BSA surface. In the presence of these receptors on the cancerous cells, the folic acid is stripped from the BSA-AuNC surface, allowing it to fluoresce and be imaged using fluorescence microscopy. This method of imaging is interesting as it shows the versatility of BSA-AuNCs as a platform for carrying out fluorescence imaging of different cancer cells using different methods which are selective for the cancer cell of interest.

Clearly the use of protein encapsulated AuNCs have much potential in both fluorescence sensing and imaging, particularly within the fields of water quality testing and cell imaging, with cell imaging leaving a lot of scope for the modification of protein encapsulated AuNCs for specific targeted imaging.

1.4 Thesis Summary

The overall aim of this thesis is to provide vital information regarding protein encapsulated AuNCs which will aid in the modification of AuNCs to provide brighter emission, and to highlight potential issues with utilising protein encapsulated gold nanoclusters as an *in vivo* sensor. It also highlights information which must be considered if AuNCs are to be utilised for observing protein aggregation.

In Chapter 2 details of the technical and underlying theoretical information regarding the fluorescence, computer simulation and physicochemical characterisation techniques employed to carry out this body of research as well as the background knowledge of proteins required for interpretation of the results are discussed.

Chapter 3 uncovers the location of AuNCs nucleation within serum albumin and unveils important information on how AuNCs form in proteins and the environment AuNCs are likely to form in.

Chapter 4 discusses the effects of AuNCs synthesis on natural HSA function and shows that the major drug binding site Sudlow I does not function as it does in natural HSA using the common fluorescent drug warfarin as a probe.

Chapter 5 characterises the HSA-AuNCs complex to uncover to what extent AuNCs alters the natural state of HSA. It was found that the protein exists in a dimer state upon AuNC synthesis and is highly sensitive to pH induced aggregation, raising questions to its use as an *in vivo* sensor.

Chapter 6 continues by characterising Ly-AuNCs to understand the common features of protein encapsulated AuNCs. It was found that the isoelectric point of lysozyme was shifted from 10.0 to 4.0 upon AuNC synthesis – like that of HSA-AuNCs. It was

also found that Ly-AuNCs also exist in a dimer form and are pH sensitive in terms of large aggregates forming. It was found that at body temperature Ly-AuNCs have similar adsorption characteristics; allowing the use of Ly-AuNCs as a means of observing lysozyme aggregation.

2 Theory

2.1 Principles of Photophysics

2.1.1 Photoluminescence

In terms of physical processes the emission of light from a molecule or atom can be divided into two categories; luminescence and incandescence. Incandescence describes the emission of light from matter which is heated whereas luminescence arises when an atom or molecule receives energy from sources other than heating[76]. The physical mechanism which all types of luminescence can be described by is the spontaneous emission of a photon from an excited electronic state of a molecule or atom[77]. Photoexcitation is the mode of excitation which this body of work concerns and can be described as the direct absorption of light by electrons in a relaxed ground state. Photoluminescence occurs by two primary forms: fluorescence and phosphorescence.

Fluorescence can be described by the relaxation of an electron from the S_1 singlet state. An electron excited to the S_1 electronic level can easily return to the ground state (S_0) since it possesses an opposite spin value to that of the ground state electron; thus, there is no violation of the Pauli Exclusion Principle upon relaxation[78]. Phosphorescence differs in that a ground state electron is excited to a singlet state but undergoes intersystem crossing from the S_1 state to the excited triplet (T_1) state. The electron spin changes so the triplet state has a symmetrical spin state to that of a ground state electron. It is therefore forbidden to relax from T_1 to T_0 under the Pauli Exclusion Principal and must undergo intersystem crossing to relax to the singlet ground state. Intersystem crossing is more likely to take place when the vibrational levels of the singlet and triplet state overlap; due to only a small amount of energy being lost in the transition.

One of the main distinguishing physical factors between fluorescence and phosphorescence is the time each spends in their excited states. This is known as the

fluorescence lifetime[79]. A Jablonski diagram can be utilised to show the physical steps involved with photoluminescence, as seen in Figure 2.1.

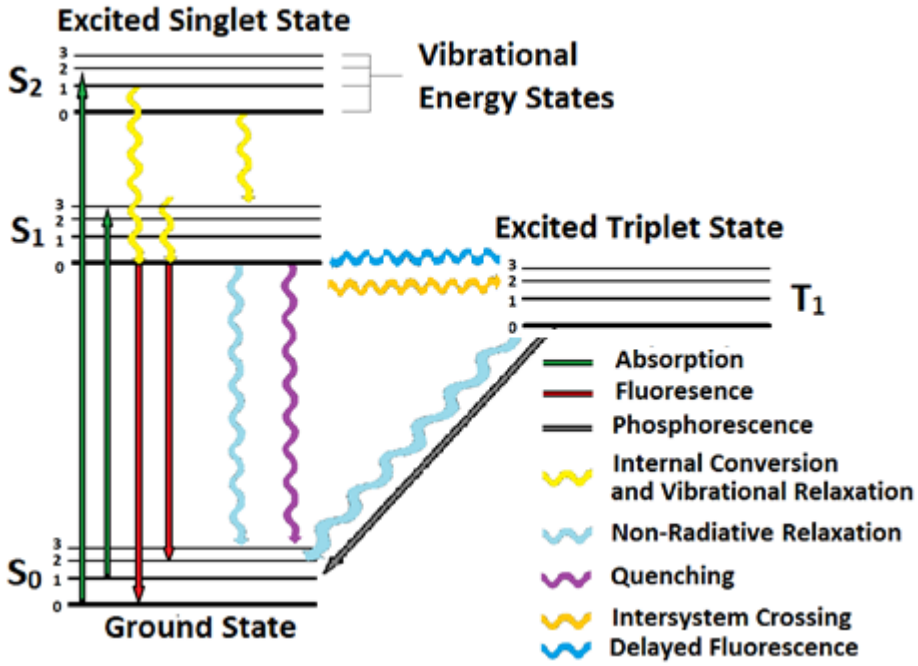

Figure 2.1 - Jablonski Diagram of physical processes which take place during fluorescence or phosphorescence.

After the absorption of a photon a molecule will quickly dissipate energy so that the excited electron is in the lowest vibrational level of the S_1 singlet state. This dissipation of energy is described as internal conversion where the excess energy is lost to the molecules surroundings over a time scale of 10^{-14} s – 10^{-11} s. This is extremely fast in comparison to the fluorescence (10^{-9} s – 10^{-7} s) and phosphorescence (10^{-6} s – 10^{-1} s)[80] process timescales (see Figure 2.2) and results in the emitted photon energy being less than that of the absorbed photon; since not all energy absorbed is emitted as a photon.

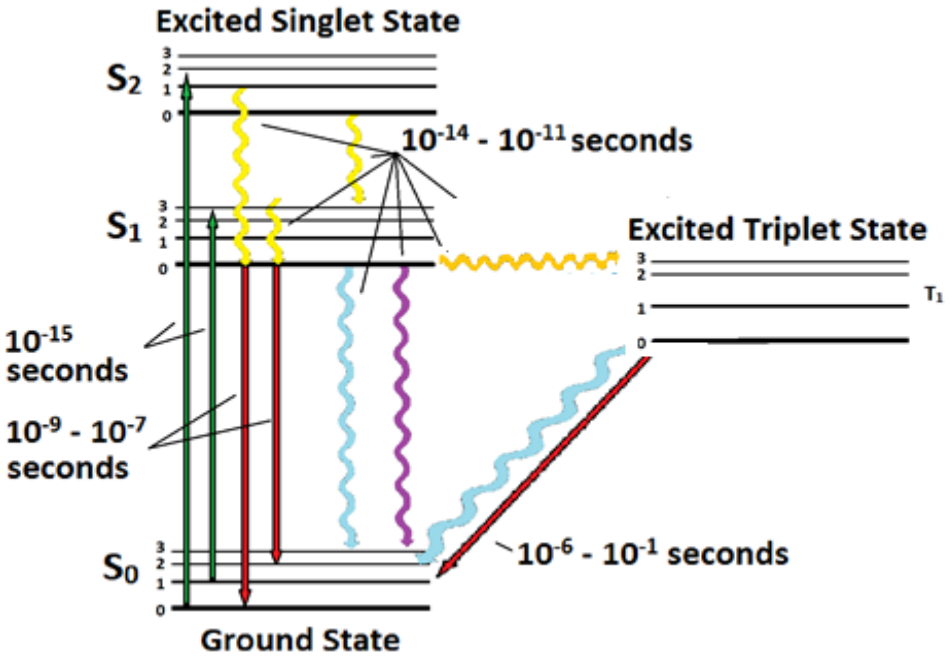

Figure 2.2 – Jablonski Diagram showing the time scale associated with each process.

This phenomenon is known as Stokes' shift which can be observed via an emission spectrum's peak wavelength 'red-shifting', as seen in Figure 2.3, compared to the excitation wavelength[79].

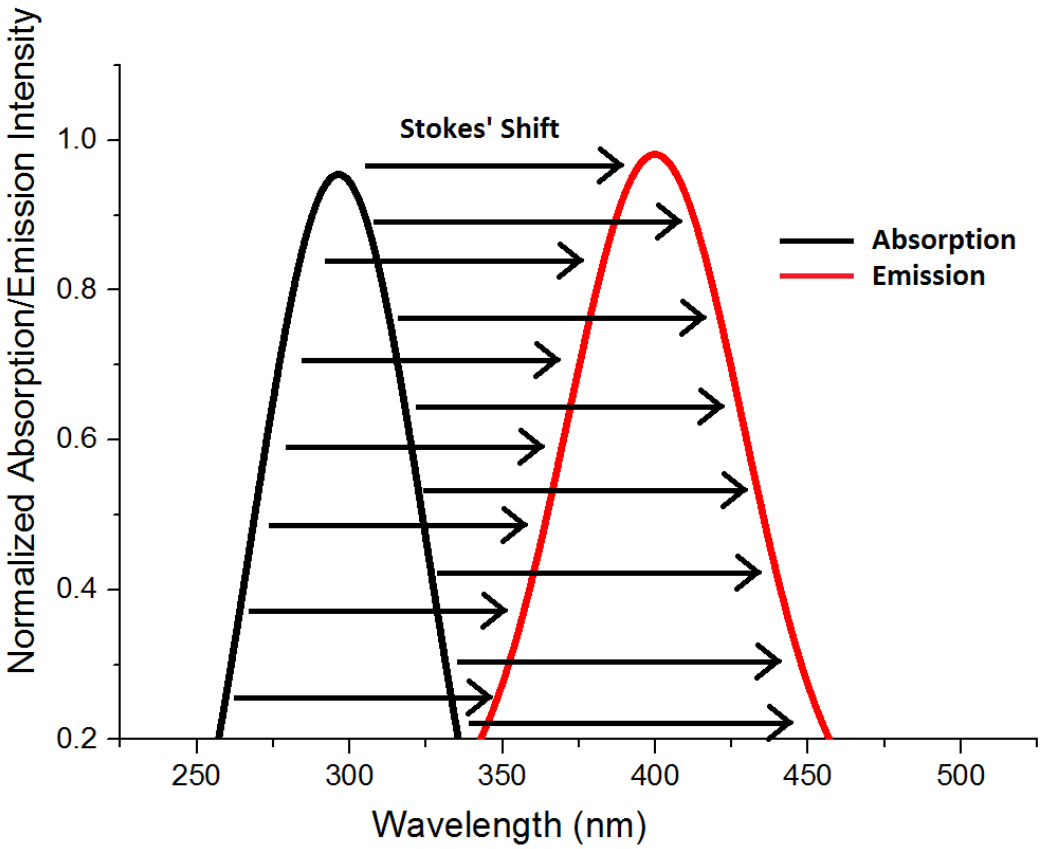

Figure 2.3 – Stokes' shift of Warfarin absorption and fluorescence. Emission spectrum can be seen to broaden due to thermal effects at the atomic scale.

2.1.2 Quantum Yield and Fluorescence Lifetime

Quantum Yield describes the ratio of emitted photons from a fluorophore to the absorbed photons. The ratio can be well defined if both radiative and non-radiative processes are considered[79]; as seen in Equation 2.1.

$$\Phi = \frac{k_r}{k_r + k_{nr}} \qquad [2.1]$$

Where: Φ = quantum yield

k_r = radiative emission rate [s^{-1}]

k_{nr} = non-radiative emission rate [s^{-1}]

It is important to note that quantum yield is defined by the rate of fluorescence and not the rate of absorption, such that it can be described as independent of the wavelength of excitation[81]. To fully understand this phenomenon, Kasha's rule must also be described[82]. This principle declares that the significant majority of photons emitted through photoluminescence occur from the lowest excited state of an electronic excited state[83]. Thus, the wavelength of excitation only affects the likelihood of absorption of a photon by a fluorophore; not the quantum yield.

The conditions under which excitation occurs for any molecular system can be well defined for either: the steady state excitation by a continuous light source of a given population of fluorophores (photostationary conditions)[84]; or the pulsed excitation by a light source of negligible pulse duration of a given population of fluorophores (transient conditions)[85]. The rate of excitation of a population of molecules for photostationary conditions can be described by Equation 2.2.

$$\frac{d[^1M]}{dt} = I_0 - (k_r + k_{nr})[^1M] \qquad [2.2]$$

Where: $[^1M]$ = concentration of excited state molecules

I_0 = intensity of light [$W.m^2$]

k_r = radiative emission rate [s^{-1}]

k_{nr} = non-radiative emission rate [s^{-1}]

To describe the rate of excitation of a population of molecules under transient conditions it is important to first understand the mathematical definition of fluorescence lifetime in terms of radiative and non-radiative rates (see Equation 2.3).

$$\tau_m = \frac{1}{k_r + k_{nr}} \qquad [2.3]$$

Where: τ_m = fluorescence lifetime [s]

k_r = radiative emission rate [s^{-1}]

k_{nr} = non-radiative emission rate [s^{-1}]

Since the time a single fluorophore will spend in the excited state is random, the fluorescence lifetime of any molecule must be defined as an average time a system spends in the excited state, rather than the absolute time. If for a system the quantum yield is equal to 1, i.e. there are no non-radiative decays; then the fluorescence lifetime can be considered intrinsic; since no outside factors are altering the time a fluorophore stays in the excited state, it can be defined by Equation 2.4.

$$\tau_n = \frac{1}{k_r} \qquad [2.4]$$

Where: τ_n = intrinsic lifetime [s]

k_r = radiative emission rate [s^{-1}]

Transient conditions refer to the creation of an initial group of excited state molecules at a time of t = 0 via a light pulse with a delta function waveform. The rate of depopulation of excited states after t = 0 can be described by Equation 2.5.

$$\frac{d[^1M]}{dt} = (k_r + k_{nr})[^1M] \qquad [2.5]$$

Where: [^{1}M] = concentration of excited state molecules

k_r = radiative emission rate [s^{-1}]

k_{nr} = non-radiative emission rate [s^{-1}]

The fluorescence response function of a fluorophore can be defined as the fluorescence at any time t after the initial excitation, shown in Equation 2.6.

$$i(t) = k_r e^{-t/\tau_m} \quad [2.6]$$

Where: i(t) = fluorescence response function

k_r = radiative emission rate [s^{-1}]

t = time after excitation [s]

τ_m = fluorescence lifetime [s]

Equation 2.6 is the archetypical model of fluorescence describing decays from a single excited state in a homogenous solution[86–88]. In a simple one exponential system, the lifetime is essentially the time it takes for the population of excited states to be 1/e (36.8 %) of the total excited states at t = 0. However, in many cases the fluorescence lifetime of a system cannot be simply explained with the one exponential model but may need 2, 3 or 4 exponentials within the model to fully describe more complex fluorescent behaviour[89–92]. In the case of more complex fluorescence behaviour the correct number of exponentials must be chosen; it is easy for a mathematical function with many parameters to correctly fit real experimental observations, but have no real meaning. Fitting fluorescence lifetime decay curves are discussed in more detail in section 2.2.4.

2.1.3 Fluorescence Quenching

Fluorescence quenching describes the decrease in the fluorescence intensity of a fluorophore due to many different physical processes[93]. Both static and dynamic fluorescence quenching arise from fluorophore interactions with another molecule in its surrounding environment. Dynamic quenching describes the physical molecular interaction between a quencher molecule and an excited state fluorophore. Static quenching differs in that the fluorophore and quenching molecule undergo the formation of a complex which no longer fluoresces. During collisional quenching, the quencher molecule encounters a fluorophore and causes an excited electron to relax to the ground state without emitting a photon. The energy held in the excited

state is released as heat energy and is dispersed into the fluorophores' surroundings. The collision between the two molecules will cause no lasting changes to each since no chemical reaction takes place during the process. Collisional quenching can be a useful tool to probe the accessibility of a fluorophore to quenching molecules[94]. This can be applied to locating fluorophores within proteins and macromolecules[95–97]. Due to the nature of dynamic quenching, temperature and pressure of the fluorophores' environment is linked to this process. An increase in either factor allows for the quenching molecule to travel over a longer distance while the fluorophore is in the excited state. The larger a distance a quencher can travel, the more likely it is to encounter the fluorophore and knock it out of the excited state. Similarly, fluorophores with longer fluorescence lifetimes are more likely to experience dynamic quenching due to the simple fact the quencher molecules have a longer time to diffuse before the emission of a photon takes place[79]. The sensitivity of a fluorophore to a quenching molecule can be described by the Stern-Volmer equation[98], seen in Equation 2.7.

$$\frac{I_0}{I} = 1 + k_Q \tau_m [Q] \qquad [2.7]$$

Where: I_0 = fluorescence intensity in absence of quencher [cps]

I = fluorescence intensity in presence of quencher [cps]

k_Q = bimolecular quenching constant

τ_m = fluorescence lifetime in absence of quencher [s]

Q = concentration of quencher [mols]

The Stern-Volmer quenching constant, k_Q, identifies the sensitivity. If the value of k_Q is low, then the fluorophore is typically not accessible by either water or water-soluble molecules; however, a high value of k_Q is an indication that the fluorophore molecule is easily accessible and most likely resides on the surface of a larger molecule. Many examples of collisional quenchers can be found, however, the more commonly found are oxygen[99–102], metallic ions[103–105] and electron-deficient

molecules such as halide ions[106,107] or acrylamide[94,108] all of which are water soluble quenchers of fluorescence.

2.1.4 Förster Resonance Energy Transfer (FRET)

A more complex method of fluorescence quenching that is used in fluorescence based sensing is the energy transfer to and from a fluorophore or fluorophore pairs. Of most interest to this thesis is Förster Resonance Energy Transfer (FRET). FRET takes place between two fluorophores over a distance between 2-10 nm, where energy absorbed by one fluorophore is transferred to another; this results in the absorbing molecule becoming quenched and causes the fluorophore which has received the energy to fluoresce. This phenomenon has been utilised in several ways using different types of fluorophore. One such method involves binding FRET fluorophores to proteins to study conformational changes under different conditions. The basic premise is that while in its natural state, energy will transfer to the acceptor fluorophore and its emission can be detected. Upon the protein undergoing conformation changes the separation of the donor-acceptor FRET pair changes, resulting in an increase or decrease in the acceptors emission intensity.

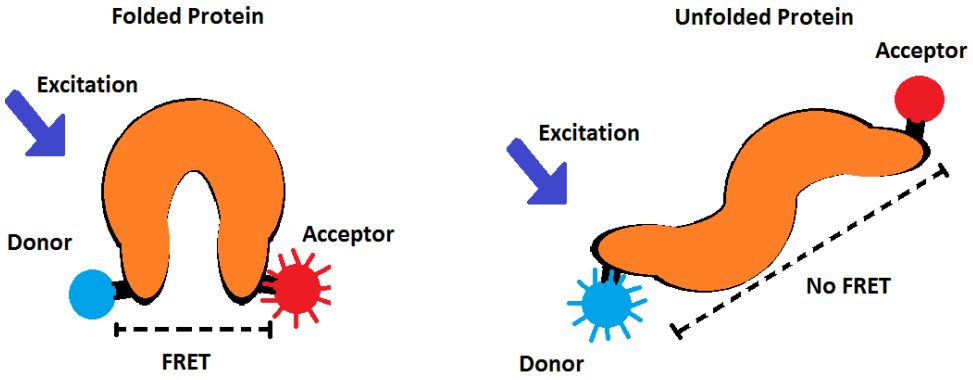

Figure 2.4: A pair of fluorophores which can undergo FRET are attached to different domains of a protein. When the protein is in its natural form the donor-acceptor pair is within close enough proximity that energy is transferred from the excited donor and emission from the acceptor is seen. Upon protein unfolding the separation between the FRET pair becomes such that energy is no longer transferred and the donor fluoresces.

Hong *et. al.* utilised this method to study the effects of heavy metal ion binding on protein conformation by monitoring the energy transfer between two Alexa Fluor dyes, each attached to one of two protein domains[109]. Another method of utilizing an increase in separation between FRET pairs involves the hybridization of hairpin Deoxyribonucleic acid (DNA) models attached to gold nano rods (GNRs) to sense messenger ribonucleic acid (mRNA)[110]. Zhang *et. al*. attached a donor fluorophore to the end of a hairpin DNA structure with a length shorter than the FRET separation needed for the donor fluorophore to transfer energy to the GNR. Upon interacting with mRNA, the hairpin unfolds, extending outwards from the GNR so that the separation between FRET pairs is so large that no energy transfer takes place and the fluorophore can fluoresce (see Figure 2.5). The detection of this fluorescence indicates the presence of mRNA.

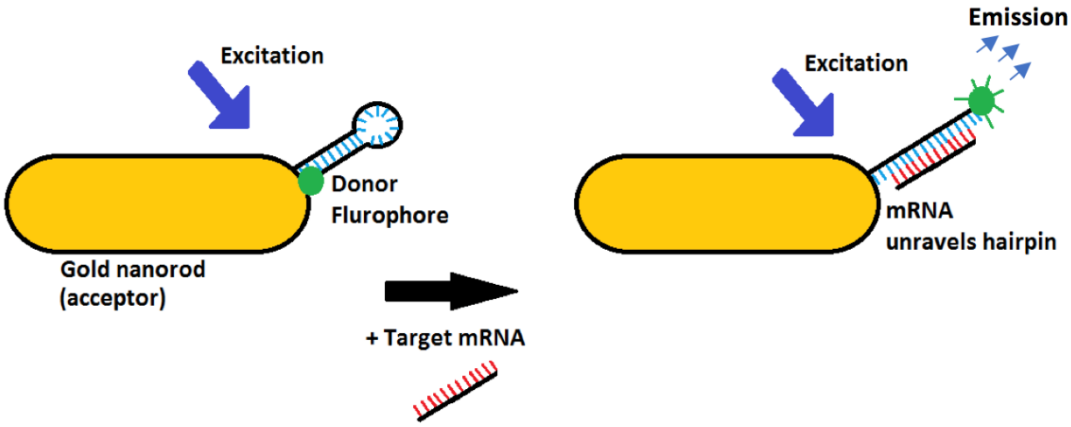

Figure 2.5: The gold nanorod acts as an acceptor for the donor fluorophore attached to the end of the hairpin DNA. While the DNA is still in its hairpin shape no fluorescence, emission is seen; upon interacting with the target mRNA the hairpin unravels creating a large separation between the fluorophore and GNR. This separation is large enough that FRET no longer takes place and the donor is seen to fluoresce.

FRET can also be utilized as a sensor for proteinase activity by attached a donor acceptor pair via a cleavable linker. In the presence of proteinase, the linker is cleaved causing the separation of donor acceptor pair and a loss in energy transfer. Huitema and Eltis successfully used variations of GFP in this manner to demonstrate the cleaving position of the cysteine proteinase of the hepatitis A virus[111].

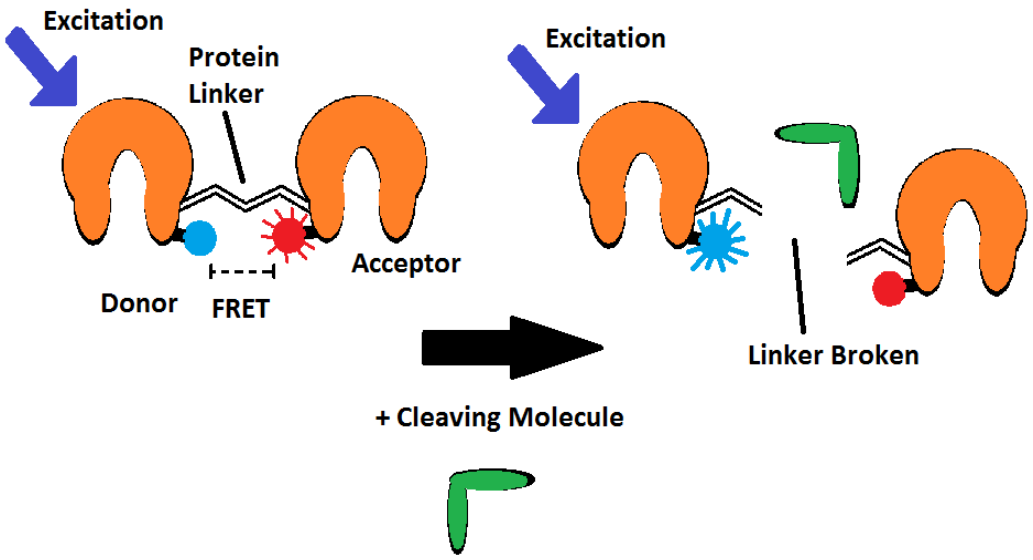

Figure 2.6: Two proteins are attached via a linker with a donor fluorophore attached to one protein and the acceptor fluorophore attached to the other. The separation of the pair is small enough that FRET takes place and the acceptor molecule fluoresces. Upon introduction of a cleaving molecule the linker which joins the proteins is broken. This creates a large separation between the FRET pair, resulting in no FRET taking place and the donor fluorophore fluorescing.

Another method of utilising FRET to quantify glucose concentration was developed by McCartney *et. al.* using con A, which has 4 binding sites for glucose[112]. Allphycocyanin (APC) is covalently attached to the con A molecule, which has dextran labelled with malachite green fluorophores bonded to it. While no glucose is present, the FRET takes place between the APC and malachite green fluorophores attached to the dextran; however, in the presence of glucose, dextran and glucose compete for the binding sites on the con A molecule, resulting in the dextran being displaced and replaced by glucose. The loss of dextran and its labelled fluorophore results in a decrease in FRET which can be measured via the emission intensity of APC and quantified with respect to glucose concentration.

While FRET based techniques for sensing are widely used to sense the presence and concentration of different molecules, it can also be utilised as a means of accurately measuring distance over a scale of 1 - 10 nm, since the rate of energy transfer between two fluorophores is proportional to the pairs' separation. With this technique, it is possible to measure distances at the single molecule level. Stein *et. al.* demonstrates the ability to measure at this scale using FRET using Rigid DNA origami blocks with predetermined binding sites on the surface at different separations for a pair of cyanine based fluorophores[113]. The same experiment was carried out using different lengths of double stranded DNA as a separator for the two fluorophores; this reproduced the same result as seen using origami blocks whereby energy transfer decreased as separation increased. This correlation was then used to calculate the separation distance based on the fluorescence intensity decrease of the acceptor fluorophore observed which matched the already known lengths of the DNA separator.

FRET does not share the same processes as either dynamic or static quenching. FRET differs in that it is a non-contact, non-radiative energy transfer between a fluorophore and a quenching molecule[79] as seen in Figure 2.7.

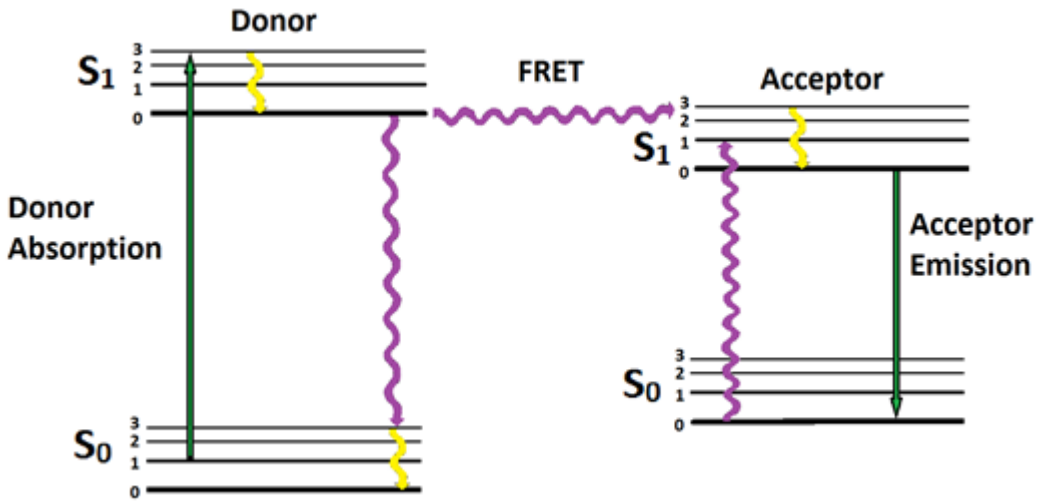

Figure 2.7: Jablonski diagram illustrating the energy processes taking place during FRET.

A donor fluorophore is excited via incident light and in the presence of an accepter molecule the energy is transferred to the donor fluorophore via a coupling of dipole moments[76]; this coupling makes the FRET process highly dependent on the separation between donor and acceptor, with the rate at which energy is transferred dropping off dramatically at distances greater than 10 nm[114,115]. It is also important to note that there is no thermal energy transfer between the donor-acceptor pair. The energy transfer results in a decrease in the fluorescence intensity of the donor, along with a decrease in the fluorescence lifetime as well. If the acceptor molecule is not quenched via other processes its fluorescence intensity will increase[116]. The energy transfer between donor and acceptor pair however is not solely due to the separation distance of the two molecules. Other factors which must be considered are the angular orientation of the dipole moments as seen in Figure 2.8, the spectral overlap between the fluorescence emission spectrum of the donor and the absorption spectrum of the acceptor as seen in Figure 2.9.

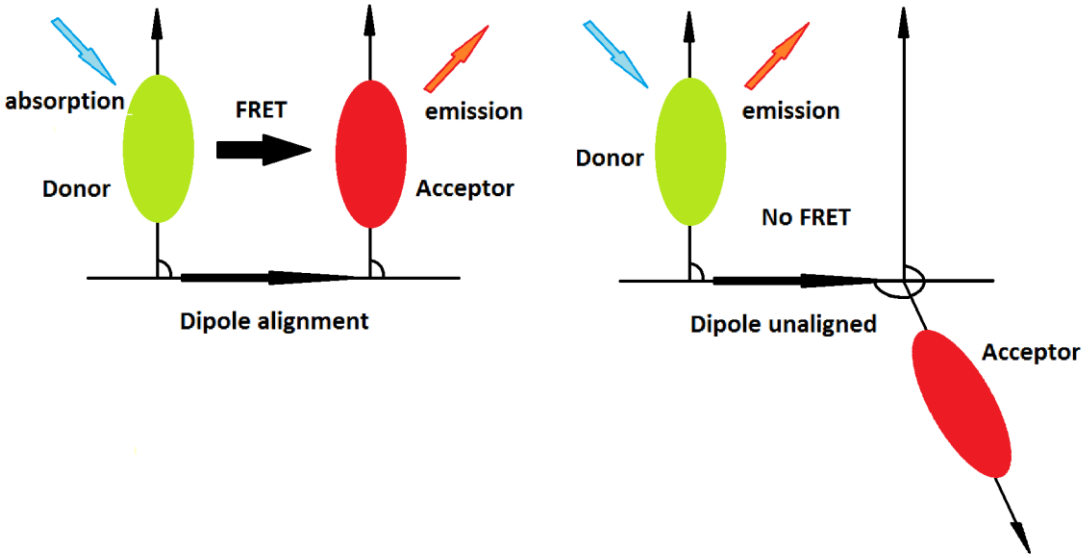

Figure 2.8: Shows the effect of dipole – dipole orientation on FRET efficiency. When dipoles are completely aligned the orientation factor is said to be κ = 1. When there is no alignment across the x and y planes then no FRET takes place and κ = 0.

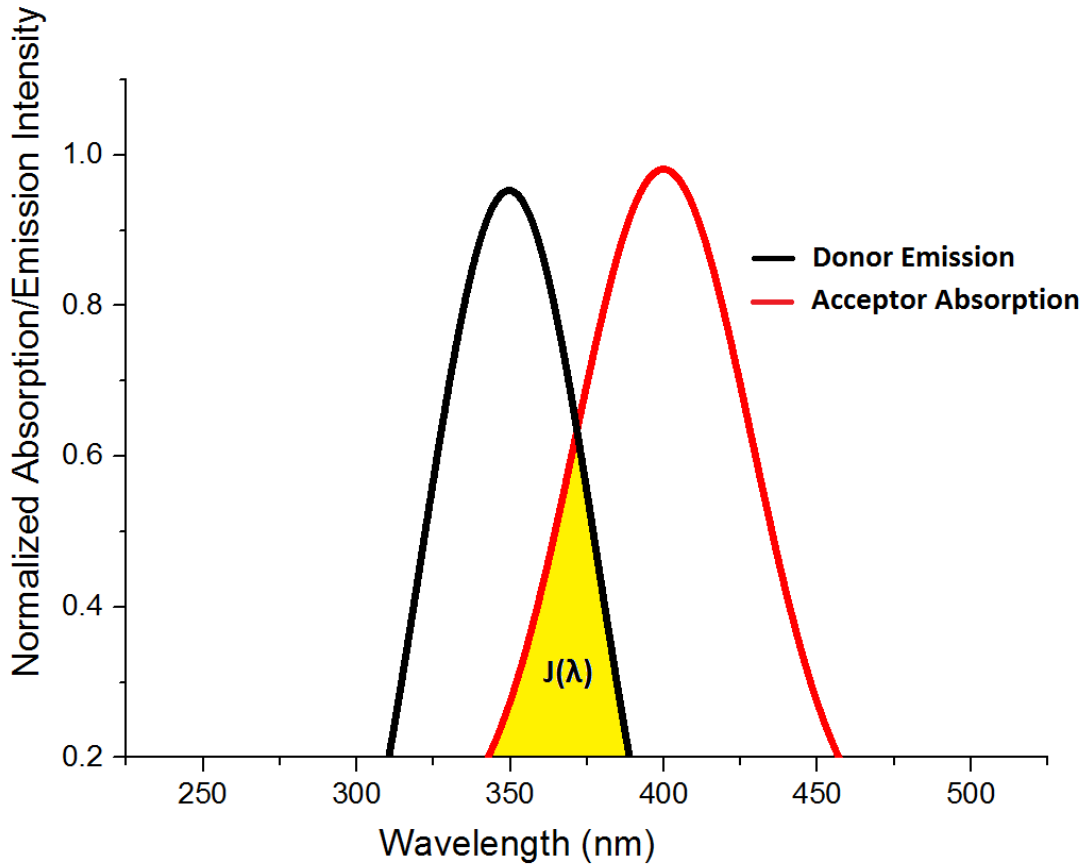

Figure 2.9: Illustration of the overlap required for FRET. The donor emission spectrum must overlap partly with the acceptor emission spectrum. More overlapping will result in a more efficient energy transfer.

To a lesser extent the natural quantum yield of the donor in the absence of the acceptor and the refractive index of the solution contributes to the efficiency of energy transfer. The efficiency of the energy transfer, first described by Förster[117], was found to be dependent on the inverse sixth-distance between donor acceptor pairs as seen in Equation 2.7.

$$E = \frac{1}{1+(r/R_0)^6} \quad [2.7]$$

Where: E = efficiency of the energy transfer

r = the separation between donor and acceptor [m]

R_0 = the Förster distance associated with the donor/acceptor pair [m]

The Förster distance R_0 describes the donor-acceptor separation at which the energy transfer efficiency is 50 %. As previously mentioned many factors are involved when determining the efficiency of FRET, which is directly correlated to R_0. The Förster distance can be described by Equation 2.8.

$$R_0 = 0.211(Q_D n^{-4} \kappa^2 J)^{1/6} \quad [2.8]$$

Where: R_0 = Förster distance [m]

Q_D = quantum yield of the donor fluorophore

n = index of refraction

κ = orientation between donor/acceptor dipoles

J = spectral overlap integral between donor (em) and acceptor (abs) spectra

The spectral overlap integral can be described by Equation 2.9, and is illustrated in Figure 2.9.

$$J(\lambda) = \frac{\int \varepsilon(\lambda) f(\lambda) \lambda^4 d\lambda}{\int f(\lambda) d\lambda} \quad [2.9]$$

Where: ε = extinction coefficient of acceptor molecule

f = emission spectrum

λ = wavelength [m]

FRET has often been described as a "nano-scale ruler"[118–120] due to the relationship between donor-acceptor separation and energy transfer efficiency. One problem in using FRET as a technique to measure Angstrom scale distances lies in the ability to distinguish between changes in the energy transfer rate. As seen in Figure 2.10 the change in energy efficiency is most apparent around the Förster distance while no change is visibly apparent at the extremities of the separation values.

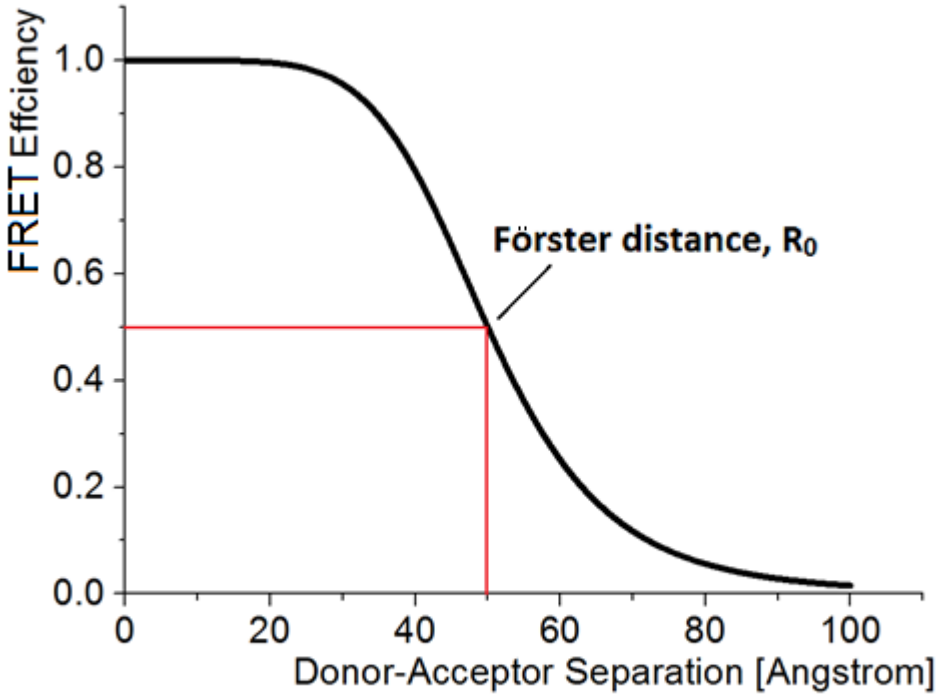

Figure 2.10: FRET efficiency plotted as a function of donor/acceptor separation distance. The Förster distance can be seen at a FRET efficiency of 0.5. Note that the change in energy efficiency is negligible between 0 – 30 nm and 80 - 100 nm in this case, thus making it extremely difficult to measure distances in those separation ranges.

The rate of energy transfer, or FRET efficiency, E, can be found by either observing the changes in the fluorescence emission intensity or fluorescence lifetime of the donor fluorophore in the presence and absence of the donor fluorophore[121–123]. FRET efficiency can be described by Equation 2.10.

$$E = 1 - \frac{\tau}{\tau_0} \qquad [2.10]$$

Where: τ = the fluorescence lifetime of the donor in the presence of the acceptor [s]

τ_0= the fluorescence lifetime of the donor in the absence of the acceptor [s]

If the observed differences between fluorescence spectra or fluorescence lifetime values are either too small or too large it is impossible to extract the correct value for donor-acceptor separation[122].

2.2 Fundamentals of Fluorescence Techniques

2.2.1 Fluorescence Spectroscopy

Fluorescence microscopy is one major area of use for fluorophores. However, it is also possible to study nanoscale phenomena without the need to directly image something to gain information on its behaviour and dynamics. Steady state fluorescence spectroscopy has been used to study nanoscale interactions by observing changes to a probes' emission spectrum. Changes to the emission spectrum with regards to wavelength position and intensity can reveal information in a variety of different fields; examples include the food processing industries[124], manufacturing[125], water treatment[126], medical and pharmaceutical industries[3,127] and geology[128], among others. One of the simplest methods of detecting molecules in solution is using direct fluorescence quenching. Fluorescence quenching is a phenomenon whereby the fluorescence intensity of a fluorophore decreases either due to non-radiative energy losses to its surrounding environment or forming a new

molecular complex which changes its ability to absorb light. The type of quenching can also be determined through measurement of the fluorescent lifetime – in this way both fluorescence emission spectroscopy and time domain fluorescence lifetime measurements can be used as methods of determining fluorescence quenching. Molecules that can affect a fluorophore's emission in such ways is referred to as a quencher. One group of molecules which are strong quenchers are the Halides. Halides are binary compounds where one halogen atom is bound to another element or radical which are less electronegative. Typical examples of a halide molecule are sodium chloride or hydrogen fluoride. Halides can be found physiologically. Most biological fluids partly consist of inorganic electrolytes, which halides function as. The concentrations of halides in different bodily fluids can act as a strong indicator to illness or disease; for example, cystic fibrosis can be characterised by a high concentration of chlorides in saliva and sweat[129]. The classical sweat test was developed by Gibson and Cooke using pilocarpine iontophoresis using electrodes placed on a patients' skin[130]. These tests are somewhat invasive for the patient and the equipment required is relatively costly. One possible test for high chloride concentration in sweat which has been suggested is the fluorescence quenching of acridinium and quinolinium dyes in solution with sweat. Both have been shown to be excellent detectors of Chloride halides due to their specificity to fluorescence quenching in their presence[131]. This fluorescence based test would not only remove the invasive aspect of the classical test, it would also be less expensive and the method itself would require less training to carry out correctly. Monitoring halides in consumer products such as cheese and other dairy products is critical to safety in the food industry. Industrial waste, especially water waste is important to monitor as high levels of halides since it can be potential disastrous to fresh water animal and fish species. While many laboratory methods are available for measuring halide concentration in ground water, there are only a few options for *in-situ* monitoring. One method of *in-situ* monitoring was developed by Cosentino *et. al.* consisting of a laser light source with fibre optics attached to a light sensor which utilises silver chromate strips. The strips reflect more light onto the sensor in the presence of chlorides[132]. This setup however is expensive, complex and could not be effectively used to monitor several sites in one area. A cheaper and more versatile method of *in-*

situ monitoring was developed by Sivaraman *et. al* utilising the catalytic effect of iodide on the reduction of ferric thiocyanate dyes[133]. The ferric thiocyanate in the presence of iodides forms non-fluorescent complexes and reduced fluorescence intensity from the dye can be measured and quantified to the iodide concentration. This method is much less complex than Cosentino's due to the availability of portable spectrophotometers and the selective nature of the experiment based on the dye which is used.

Two important experimental techniques to this thesis are UV-Vis Spectroscopy and Fluorescence Emission/Excitation Spectroscopy. It is useful to discuss both techniques together, since both techniques are complimentary to one another. UV-Vis spectroscopy essentially measures transitions from the ground state to the excited state across the ultraviolet-visible spectrum whereas Fluorescence Spectroscopy measures transitions from an excited state to a ground state across the same wavelength region.

The UV-Vis spectrometer makes use of 2 light sources; a halogen lamp for excitation between 300 - 1100 nm and a deuterium lamp for excitation between 190 - 350 nm (A Xenon flash lamp while less common can also be used to cover the range of 190 - 1100 nm removing the need for 2 separate light sources[134]). The light is passed through a monochromator, which is used to scan through a chosen wavelength range. The light from the monochromator passes through the sample chamber where the light is absorbed and continues onto a detector. The experimental setup for this apparatus is shown in Figure 2.11.

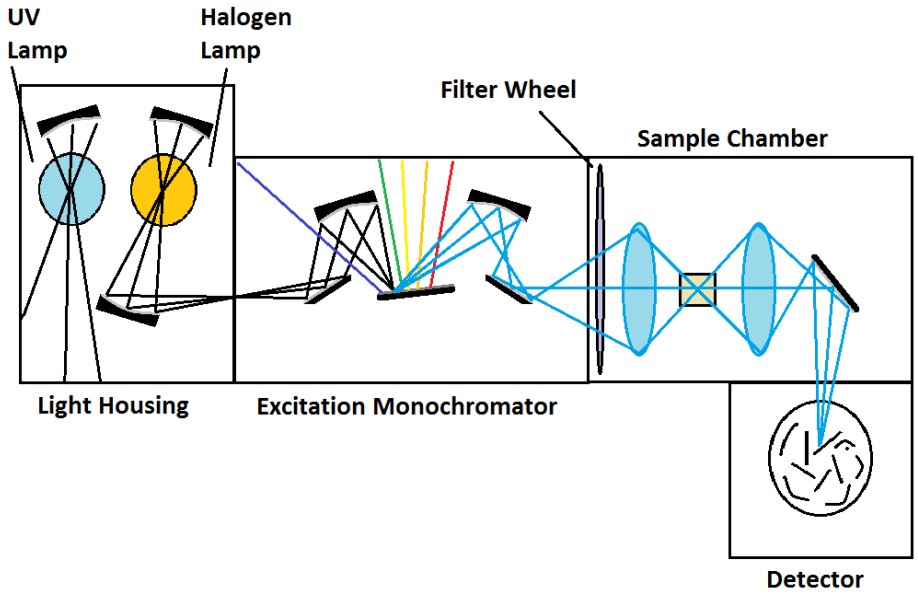

Figure 2.11: Schematic diagram of a typical UV-Vis Spectrometer apparatus setup.

The absorption spectrum is constructed by observing the difference between light intensity with and without a sample in the beam path at each wavelength. Some experimental setups will split the light beam equally and direct each new beam into separate sample chambers using a beam chopper or beam splitter. This allows a blank sample and sample can to be measured simultaneously[80]; however, the setup shown considers two measurements made sequentially with only one sample chamber. The light absorption of a sample can be written mathematically in terms of the excitation wavelength and absorbance (or transmittance), shown in Equation 2.11.

$$A(\lambda) = log_{10}\left(\frac{I_0}{I}\right) = -log_{10}T(\lambda) \quad [2.11]$$

Where: A(λ) = Absorbance of the material with respect to wavelength [Au]

I_0 = radiant flux received by the material [W]

I = radiant flux transmitted by the material [W]

T(λ) = Transmittance of the material with respect to wavelength [m]

While UV-Vis spectroscopy can be used to simply characterize a sample through the position of absorption peaks[135], it is also possible to determine the concentration of a known molecule through the Beer-Lambert Law; which states the absorbance efficiency of a solution is directly proportional to the path length (i.e. the length of solution the beam passes through; typically, 1 cm for a standard size cuvette) and the concentration of absorbing molecule[96] (as seen in Equation 2.12).

$$A(\lambda) = \varepsilon lc \quad [2.12]$$

Where: A(λ) = Absorbance of the material with respect to wavelength

ε = Molar absorption coefficient [$L.mol^{-1}.cm^{-1}$]

l = path length on incident light through solution [cm^{-1}]

c = concentration of solution [mol^{-1}]

There are cases however where the Beer-Lambert law does not hold true. The formation of aggregate particles in solution[136], high concentration[137] and other chemical and physical scattering phenomena[138–140]all cause derivations from the direct proportionality of absorbance efficiency and absorbing species concentration.

The Emission/Excitation spectrofluorometer has a similar apparatus setup to UV-Vis spectroscope. A broadband Xenon light source is used to excite a population of fluorophores in solution and the resulting fluorescence emission is captured by a

photo-detector. The light passes through monochromators both before and after passing through the sample; either one of which can be cycled through a range of wavelengths to yield either an excitation or emission spectrum. One difference in the experimental setup is the path in which the beam follows (see Figure 2.12).

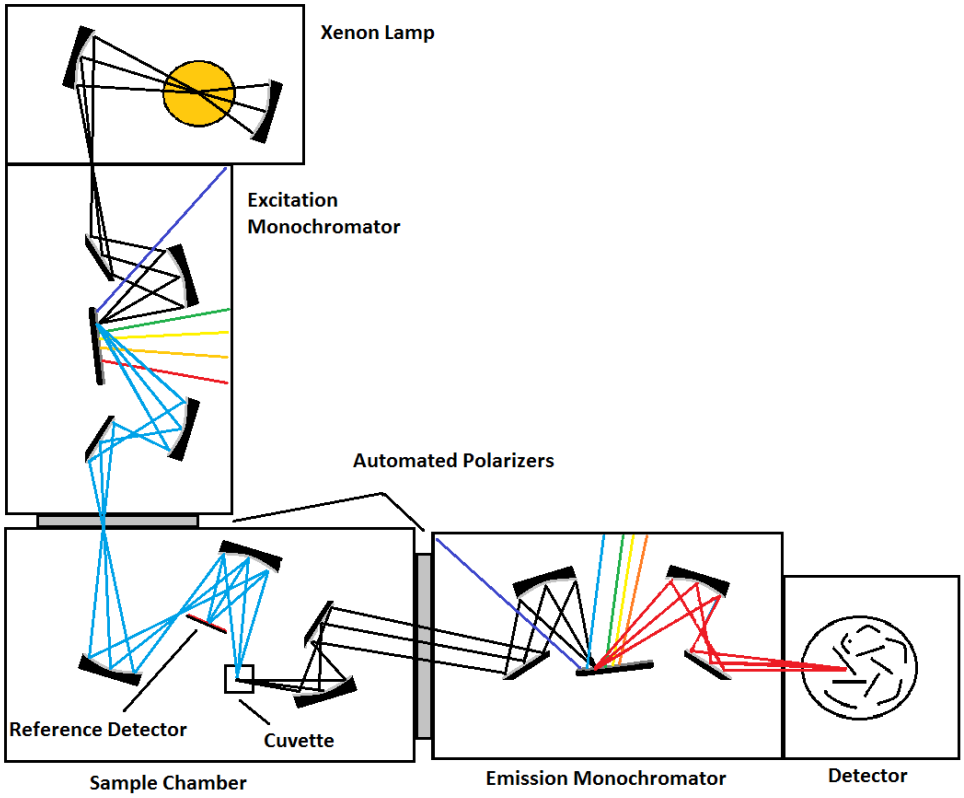

Figure 2.12: Schematic diagram of a typical Emission Spectrometer apparatus setup.

The light leaves the sample chamber perpendicular to the incident excitation light to decrease the amount of excitation light passing through to the detector, since it is only the fluorescence emission of the sample which is of interest. Another difference is that the fluorescence emission from a population of fluorophores is highly dependent on the intensity of the excitation light source. One problem that can arise from this technique involves fluctuations in the intensity output of the light source

over the measurement period. To rectify this problem, a secondary detector is placed in the sample chamber to monitor the overall power output of the light source. The sample detector signal can then be divided through by the light source detector to remove this bias from the final spectrum generated.

Fluorescence Emission/Excitation Spectroscopy can be used to characterize a sample in solution[141–143], as with UV-Vis Spectroscopy, the fluorescence emission of a molecule can be quenched or enhanced depending on the presence of other molecules[144,145] and also by physical changes to the solution such as changes in temperature[146] or pressure[147]; making Fluorescence Emission/Excitation Spectroscopy a powerful tool for probing interactions between proteins or macromolecules on the single molecule scale.

2.2.2 Fluorescence Lifetime Spectroscopy

Fluorescence lifetime spectroscopy concerns the measurement of the time a fluorophore stays in the excited state. There are currently two approaches to measuring the fluorescence lifetime of a molecule, frequency-domain lifetime measurements and time-domain lifetime measurements. Frequency-domain lifetime measurements yield information from a population of molecules by exciting the sample with a light source that is intensity modulated at a frequency similar in time to the reciprocal of the fluorescence lifetime being probed. This method of excitation causes the fluorescence emission to be modulated at the same frequency; albeit with a time delay and change to the overall amplitude in comparison to the excitation. The fluorescence lifetime is then extrapolated from the change in peak to peak height of the emission wave in comparison of the peak to peak height of the excitation wave. This method of measuring is not employed in this thesis and all emphasis will be placed on time-domain lifetime measurements from this point.

The Time Correlated Single Photon Counting (TCSPC) technique[148] is the main technique used to investigate changes to fluorescence lifetime in this work. The main apparatus setup for carrying out a TCSPC measurement can be seen in Figure 2.13.

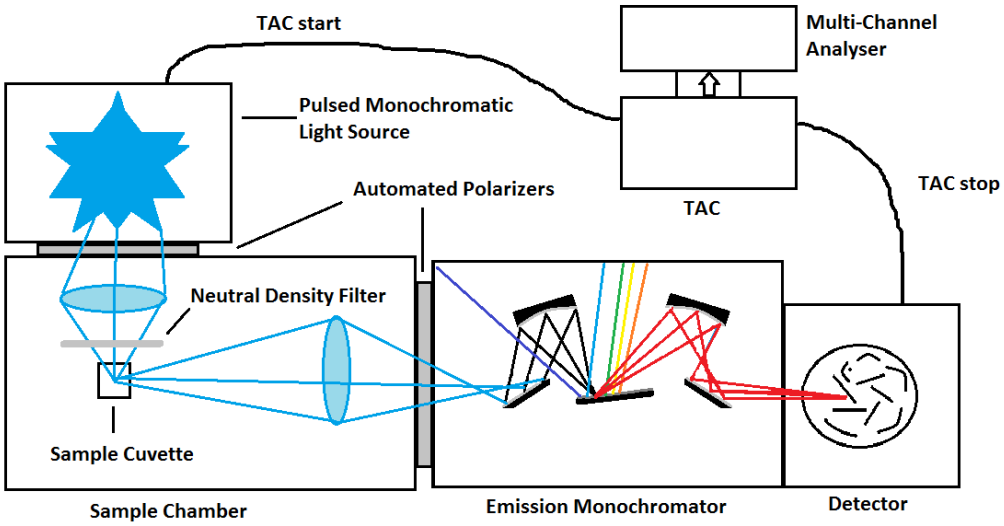

Figure 2.13: Typical Experimental setup for TCSPC based techniques.

A pulsed light source (typically, laser diodes or LEDs are used as the light source) is focused onto a sample in a light-tight sample chamber; at the same time the light source is pulsed, a trigger signal is sent to start the timing electronics. After a period, the sample will fluoresce, emitting a photon which is detected by a PMT detector, sending a trigger signal to stop the timing electronics. A monochromator is used to select the emission wavelength of interest and the emission polarizer is set to the magic angle; for square geometry, the magic angle is 54.7 °[79]. The magic angle describes the value at which interactions which depend on the second order Legendre polynomial vanishes – such as depolarizing phenomena which can take place during fluorescence decay acquisition. Depolarization effects such as FRET can enhance the fluorescence decay and result in incorrect fluorescence decay values. The time-to-amplitude converter (TAC) measures a period by building the voltage in a capacitor. The voltage when the stop signal is received is converted to a time and stored in a histogram of measured fluorescence lifetimes. The electronics creating the histogram is known as the multi-channel analyser (MCA). Any time after the stop signal has been received and before the next start signal has been sent is known as the dead time. To acquire a complete fluorescence lifetime decay curve, this process must be

continually carried out until one channel in the histogram has received a set amount of counts (typically pre-set to stop the experiment at a peak count of 10,000). If the sample does not fluoresce and a stop trigger signal is not sent the TAC will reset upon the next start trigger signal and no time will be recorded. This is typical for a TCSPC measurement as the experiment is setup to detect 1-2 photons per 100 excitation events. This is critical to avoid bias towards detecting shorter fluorescence lifetimes. During each excitation event, only one photon can be registered by the detector; always being the first photon emitted by the sample. The excitation/emission ratio is tracked by dividing the stop signal rate by the start trigger rate to give what is known as the α value. To keep the α value below 2 % neutral density filters are placed in the beam path before the sample is excited to dampen the excitation intensity focussed onto the sample. This results in fewer photons emitted. If the TAC range selected to measure over results in a dead time longer than the measured time, then it can be beneficial to measure in reverse mode. Reverse mode switches the source of the start and stop signals so that a measurement is made for every emission event rather than excitation. This stops the timing electronics measuring dead time for every excitation event, lowering the total amount of time required to collect a full data set.

For it to be possible to yield correct fluorescence lifetimes from the data the instrument response must be known. This is measured before the fluorescence lifetime decay curve by utilizing Rayleigh scattering. The emission monochromator is set to the excitation wavelength, both polarizers are set to vertical and a silica colloid solution (typically a Ludox SM-AS solution) is placed in the sample chamber. The time taken for the pulsed excitation source to be detected directly is measured. In ideal conditions the instrumental response would result in a δ-function (i.e a single peak reserved to only one data channel), however due to the imperfections inherent with the light pulses used in exciting the samples and pulse broadening from the optical components the resulting instrumental response is broader, an example is seen in Figure 2.14.

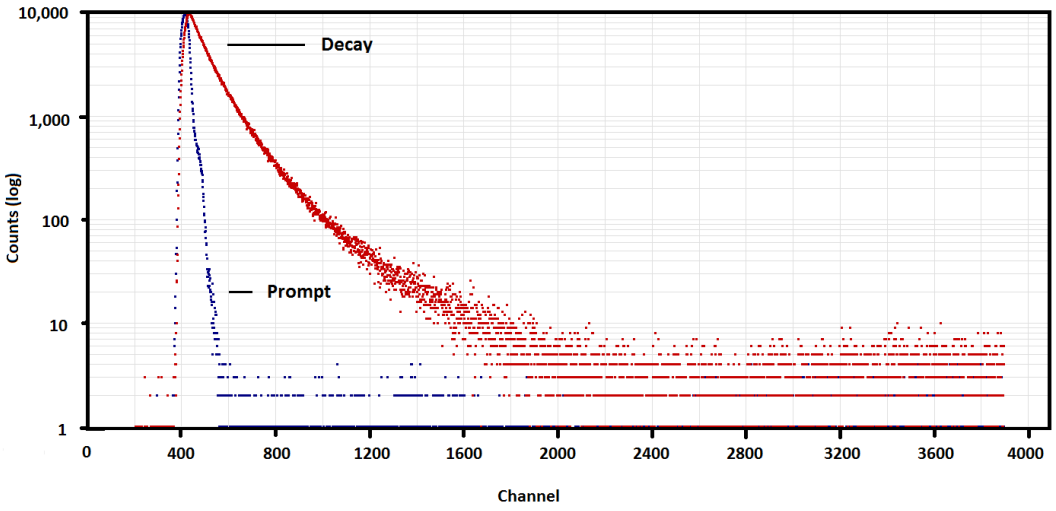

Figure 2.14: Fluorescence decay curve of HSA measured over a TAC range of 100 ns. The instrument response or 'prompt', can be seen in blue and the decay curve in red. Excitation 295 nm, Emission 320 nm.

The prompt and the fluorescence lifetime decay are convoluted in the measured decay curve, as shown in Equation 2.13. To yield correct values for the fluorescence lifetimes measured the prompt and fluorescence decay must be reconvoluted.

$$P(t) \otimes i(t) = F(t) \qquad [2.13]$$

Where: P(t) = Instrumental response function

i(t) = Impulse response function

F(t) = Theoretical model of fluorescence decay

To find the correct values for the fluorescence lifetimes the correct mathematical model to describe F(t) must be used. Depending on the complexity of the samples fluorescence characteristics, a one or more exponential model is used to describe the fluorescence lifetime values and their associated pre-exponential values, shown in Equation 2.14.

$$I(t) = \sum_{i=1}^{n} b_i \exp\left(-\frac{t}{\tau_i}\right) \quad [2.14]$$

Where: I(t) = decay function with respect to time

b_i = fluorescence lifetime amplitude

τ_i = fluorescence lifetime [s]

t = time after excitation [s]

To test the quality of the fit between the theoretical function and the measured decay the non-linear least squares fitting method is employed. The goodness of fit is determined by the chi squared value (χ^2), shown in Equation 2.15.

$$\chi^2 = \sum_N \left[\frac{Y(i) - F_d(i)}{\sigma(i)}\right]^2 \quad [2.15]$$

Where: Y(i) = measured data

$F_d(i)$ = fitted function

$\sigma(i)$ = standard deviation of Y(i)

N = number of data channels selected for analysis

A value of 1.0 for χ^2 is considered a perfect fit, however it is widely accepted that a value of $0.9 > \chi^2 > 1.3$ is considered a good fit. Also, important to determining a good fit is the use of the weighted residuals (W_i). If the weighted residuals are distributed randomly around the fitted function, then it is considered that the correct theoretical method has been chosen and a good fit has been achieved. If, however the weighted residuals are non-random, then the model has not fit the data correctly and must be reviewed. Examples of random and non-random weighted residuals are shown in Figure 2.15.

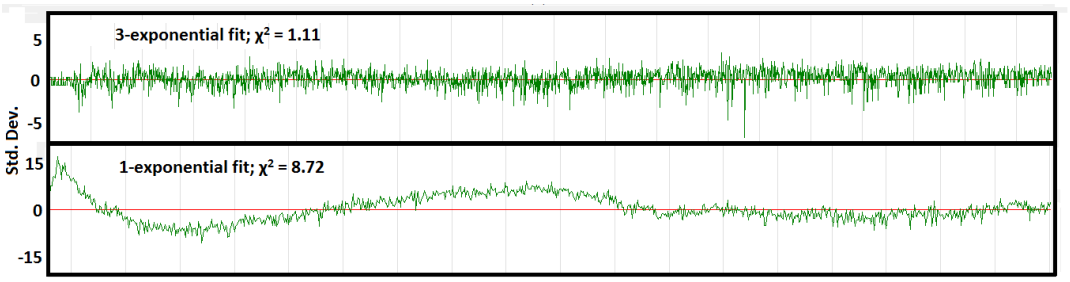

Figure 2.15: Random and non-random weighted residuals for 3 and 1 exponential fitting to a fluorescence lifetime decay curve. It can be clearly seen that in this example a 3 exponential fit describes the decay curve correctly since the χ^2 value is between 0.9 and 1.3 and the residuals are randomly distributed around 0. For the 1 exponential fit neither of these criterions is met and thus does not correctly describe the decay curve.

For longer fluorescence lifetimes which need to be measured using a TAC longer than 13 µs it becomes beneficial to measure using the Multi-Channel Scaling (MCS) technique[79]. At such long TAC ranges the time resolution becomes ≥85 ns per channel depending on the length of TAC chosen. At this time resolution, current timing electronics are fast enough to register a stop trigger signal for each data channel per start trigger signal. Essentially the MCS sweeps through the whole TAC range treating each channel in the same way the TCSPC technique treats the whole-time range. The main difference between MCS and TCSPC techniques is the way in which a sample is excited. Rather than pulse a light source as in TCSPC, a spectra-LED is turned on for a period continuously exciting the sample to a steady state and then switching off. After the light source has been switched off, the fluorescence decay from the sample from that point is measured, resulting in a decay curve, as seen in Figure 2.16.

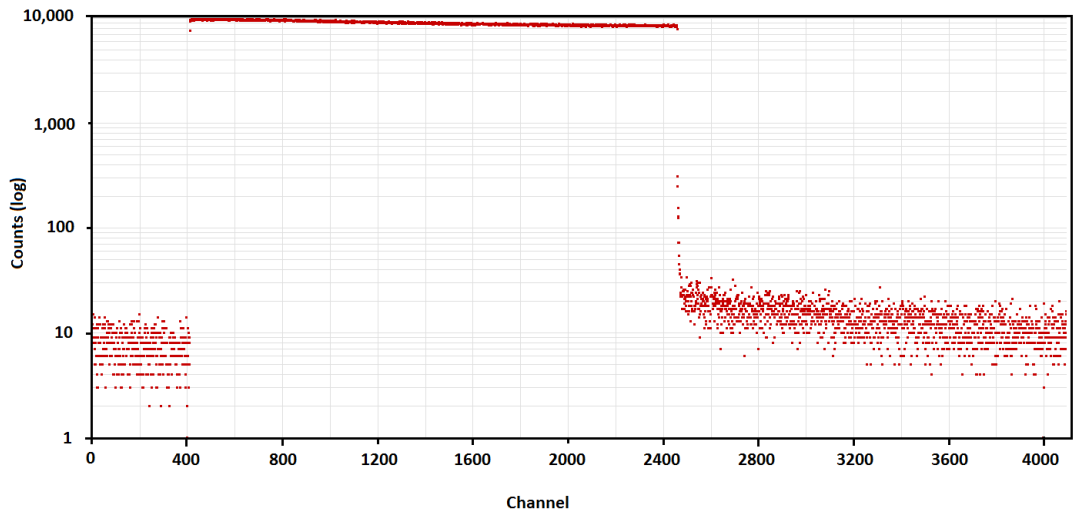

Figure 2.16: MCS decay curve for HSA-AuNC (excited at 295 nm, emission at 670 nm). The fluorescence decay is fitted from the falling edge (~channel 2400) of the steady state period (~channel 400-2400).

As with TCSPC pile-up effects are possible in each data channel if the α value is greater than 2 %; again, this must be controlled using neutral density filters. At such long TAC ranges, it is not necessary to measure at the magic angle since polarization effects resulting from photo-selection happen at a much shorter time scale. The resulting decay curve is analysed by fitting the falling edge after the steady state emission. Fitting is less complex since it is not necessary to consider the instrument response due to the large time scales MCS is used at, however the exponential model is still used to describe the experimental data and the non-linear least squares fitting method is used to test the quality of the fit between theoretical function and experimental data.

A more advanced technique which utilises TCSPC is Time Resolved Emission Spectroscopy (TRES). TRES differs from regular TCSPC in that multiple measurements are taken over an emission wavelength range to gain information on the emission spectra of individual fluorescent species with their own fluorescence lifetime. At each wavelength increment data is measured for a set period. All the decay curves measured are then combined and a global fit is applied to yield

fluorescence lifetimes. Each individual decay curve is then fitted using the previously found lifetime values to gain relative amplitudes for each lifetime at each emission wavelength. The data can then be displayed as relative amplitude vs emission wavelength, effectively giving an emission intensity spectrum associated with each lifetime.

A much simpler and more widely used fluorescence based technique for measuring at the nanometre scale is fluorescence anisotropy. Fluorescence anisotropy is a powerful tool which can measure the size of single molecules by tracking the rotational time of a molecule undergoing Brownian motion. This is carried out by exciting either an intrinsic fluorophore or attaching an extrinsic fluorophore to a molecules surface, using vertically polarized light. Only fluorophores whose dipole moment are aligned with the polarized light will be excited – in this way the orientation of the excited state population of molecules is known at the start. The emission from the excited population is then measured at vertical and horizontal polarization; from this the rotational time can be calculated. If the temperature and viscosity of the solvent is known, then the hydrodynamic radius of the molecule can be calculated from the rotational diffusion time. Several groups have made use of fluorescence anisotropy to observe single molecule dynamics which are unable to be tracked via fluorescence microscopy methods. Stewart *et. al.* demonstrated the viability of this technique by measuring the radius of stable Ludox colloids of known radius using a newly synthesised ADOTA derived fluorophore with an unusually long lifetime of ~20 ns[149]. Using fluorescence anisotropy, it was possible for the investigators to correctly measure particle sizes less than 10 nm to within an error of less than 10 %. One of the major disadvantages of fluorescence anisotropy is the length of the fluorescence lifetime of the fluorophore used must be close in length to the rotational time of the molecule under observation. As molecules get larger and more complex their rotational time also increases. If a fluorophores lifetime isn't sufficiently long, then the time it spends in the excited state is too short for the molecule to rotate enough to the point it has depolarized. To overcome the problem of measuring large particles with fluorescence anisotropy Raut *et. al.* studied the polarization properties of Bovine Serum Albumin-encapsulated (BSA) gold nanoclusters (AuNCs) under different conditions[150]. These fluorophores have

exceptionally long lived fluorescence lifetimes in the microsecond regime. The investigators successfully displayed polarization properties present in these new types of fluorophores offering the possibility of using them to measure the diameter of large particles in solution. Protein-encapsulated AuNCs have also been demonstrated to measure protein unfolding due to pH. Li *et. al.* successfully used the polarization properties of AuNCs within BSA to measure the radius of the protein under highly acidic conditions[151]. It is known that under these conditions BSA unfolds, giving the protein a larger hydrodynamic radius. This was observed via the longer rotational time of AuNCs under acidic conditions in comparison to neutral pH.

2.3 Fundamentals of Molecular Dynamics (MD)

To compliment the experimental work carried out in the laboratory, computational models of the protein-AuNCs complexes were created using Molecular Dynamics (MD) simulations[152]. In simplest terms MD allows for the simulation of molecules and single atoms interacting with each other over a given period, basing the interactions on approximations of the laws of physics. The position, velocity and acceleration of each individual atom in the simulation is known and used to calculate its next location and velocity after a given timestep. The interactions between each of the particles are represented by potential energy and are simulated by molecular mechanics' force fields. In MD, the potential energy is associated with a set of forces, referred to as the force field, which acts upon a particle; thus, potential energy only depends on the particle position in space. These calculations are carried out numerous times for each timestep for every atom in the system until a satisfactory trajectory of each particle is known. These trajectories can then be studied to gain information on atomic interactions on the single molecule scale. Before looking at the calculations carried out to find the trajectories it is important to describe how molecular models are first setup based on individual particles. MD makes use of molecular mechanics (MM) to set up model molecular systems based on classical mechanics. Each particle is given a few characteristic parameters based on which atom is being modelled. The parameters given are a radius based on the van der

Waals radius of the atom, a constant net charge and a polarizability value. All bonded atoms are treated like classical springs which rest at the equilibrium distance for that given atom-atom bond (either measured experimentally or calculated theoretically). Bond angles are also taken into consideration during calculations. To optimize a molecular construct in MD MM is used to minimize the molecules potential energy to find the lowest energy conformation of the given molecule. The force field previously described is used as a criterion for finding the local minimum for each atom while an algorithm is running to find the global lowest energy conformation. The force field itself is modelled using the sum of two equations, the difference between the two depending on whether interactions between each atom are bonded or non-bonded interactions. The equations used to model bonded interactions are shown in Equation 2.17.

$$U(R^{\rightarrow})_{bonded} = \frac{1}{2}\sum_{bonds} K_b(b - b_0)^2 + \frac{1}{2}\sum_{angles} K_\theta(\theta - \theta_0)^2 + \sum_{dihedrals} K_\phi[1 + \cos(n\phi - \delta)] + \sum_{impropers} K_\omega(\omega - \omega_0)^2 \quad [2.17]$$

Where: $U(R^{\rightarrow})_{bonded}$ = force field energy due to bound interactions

$R^{\rightarrow}$ = set of separate atom vectors

K_b = spring constant for bonds [N]

b = bond length [m]

K_θ = spring constant for bond angles [N]

θ = bond angle [°]

K_ϕ = spring constant for bond dihedrals [N]

(nϕ-δ) = bond dihedral rotation [°]

K_ω = spring constant for improper bonds [N]

ω = improper bond angle [°]

The equations used to model non-bonded interactions are shown in Equation 2.18.

$$U(R^{\rightarrow})_{unbound} = \sum_{i>j}\left(\frac{A_{ij}}{r_{ij}^{12}} - \frac{B_{ij}}{r_{ij}^{6}}\right) + \sum_{i>j}\frac{q_i q_j}{4\pi\varepsilon_0 r_{ij}} + \sum_{i>j}^{(4)}\left[v_{1,4}\left(\frac{A_{ij}}{r_{ij}^{12}} - \frac{B_{ij}}{r_{ij}^{6}}\right) + e_{1,4}\frac{q_i q_j}{r_{ij}}\right]$$

[2.18]

Where: $U(R^{\rightarrow})_{unbound}$ = force field energy due to unbound interactions

A_{ij} & B_{ij} = nuclear force constants for atomic interactions

r_{ij} = separation between 2 atoms [m]

q = charge of atom [C]

ε_0 = electric permittivity [$F.m^{-1}$]

Some approximations must be made when modelling atomic interactions in MD. Firstly the bonded interactions are modelled upon the simple harmonic oscillator case from classical mechanical physics. Secondly all the atoms in the system are treated as hard spheres and all collisions are perfectly elastic, so that there is a conservation of all kinetic energy and momentum such that an atoms shape cannot be deformed in MD. The charge state of the atoms is not changed during the trajectory and following on from this fact no bonds are created or broken in MD simulations. To minimise the global potential energy of the system the atoms are placed in non-equilibrium geometry and mathematical procedures based on energy minimization methods are used to relocate the atoms into its lowest energy configuration. Potential energy surfaces are created with atomic positions as variables. It is then possible to use gradient based algorithms to find the best coordinate for the atoms using the simple gradient descent method.

The MD trajectories are calculated using classical mechanics, represented by Newton's laws of motion, shown in Equations 2.19 and 2.20.

$$F^{\rightarrow}(r_i^{\rightarrow}) = -\nabla U(r_i^{\rightarrow}) \quad [2.19]$$

$$F^{\rightarrow}(r_i^{\rightarrow}) = m_i a_i = m_i \frac{d^2 r_i^{\rightarrow}(t)}{dt} \quad [2.20]$$

Where: $F^{\rightarrow}(r_i^{\rightarrow})$ = force experienced by an atom [N]

$U(r_i^{\rightarrow})$ = energy [J]

m_i = mass of atom [kg]

a_i = acceleration of atom [$m.s^{-2}$]

To integrate Newton's equations of motion the Velocity Verlet algorithm[153] is used. Based on the Verlet algorithm, the position of the atom is updated every time step using Equation 2.21.

$$r_i^{\rightarrow}(t + \Delta t) = r_i^{\rightarrow}(t) + v_i^{\rightarrow}(t)\Delta t + \frac{1}{2} a_i^{\rightarrow}(t)\Delta t^2 \quad [2.21]$$

Where: $r_i^{\rightarrow}$ = atom position

$v_i^{\rightarrow}$ = velocity of atom [$m.s^{-1}$]

$a_i^{\rightarrow}$ = acceleration of atom [$m.s^{-2}$]

t = time [s]

The Velocity Verlet algorithm calculates velocities every full and half time step through Equation 2.22.

$$v_i^{\rightarrow}\left(t + \frac{\Delta t}{2}\right) = v_i^{\rightarrow}(t) + \frac{1}{2} a_i^{\rightarrow}(t)\Delta t \quad [2.22]$$

As previously mentioned the position, velocity and acceleration are needed to create trajectories in MD. Acceleration of each particle in the next timestep can be found using Equation 2.23.

$$\vec{a_i}(t + \Delta t) = -(\frac{1}{m_i})\nabla U[\vec{r_i}(t + \Delta t)] \quad [2.23]$$

The Velocity Verlet algorithm then calculates velocities also in the next timestep using Equation 2.24.

$$\vec{v_i}(t + \Delta t) = \vec{v_i}\left(t + \frac{\Delta t}{2}\right) + \frac{1}{2}\vec{a_i}(t + \Delta t)\Delta t \quad [2.24]$$

To correctly simulate a system, the molecules temperature must be taken into consideration. In MD temperature is not an independent variable but represented as a statistical quantity expressed as a function of the position and momenta of all particles. If the total number of particles is large enough it is possible to find the temperature using the kinetic theory of gases, shown in Equation 2.25.

$$T(t) = \sum_{i=1}^{N} \frac{m_i v_i^2(t)}{K_B N_f} \quad [2.25]$$

Where: T(t) = temperature with respect to time [K]

m_i = mass of atom [kg]

v_i = velocity of atom [$m.s^{-1}$]

K_B = Boltzmann's constant [$J \cdot K^{-1}$]

N_f = number of degrees of freedom

To 'heat' a molecule to the correct temperature in MD simulations Langevin dynamics are employed[154]. Another consideration to consider is the size of the overall simulation box. It is important that the box is much larger than the molecule so that water molecules and other atoms freely move and interact with the protein surface. One way of overcoming this is the introduction of periodic boundary conditions. The simulation box (typically cube or cuboidal in shape) is surrounded by image replicas of itself so that the primary cell has replica image cells on every

surface. Only the trajectories of the primary cell are calculated and recorded, when the trajectory of a particle passes into an image cell. If a particle moves into an image cell it also appears in the primary cell in the exact position it crossed into the image cell since all cells are identical. This effectively allows for particles to continue travelling in trajectories which would normally interact with the box surface and appear on the other side, as shown in Figure 2.17.

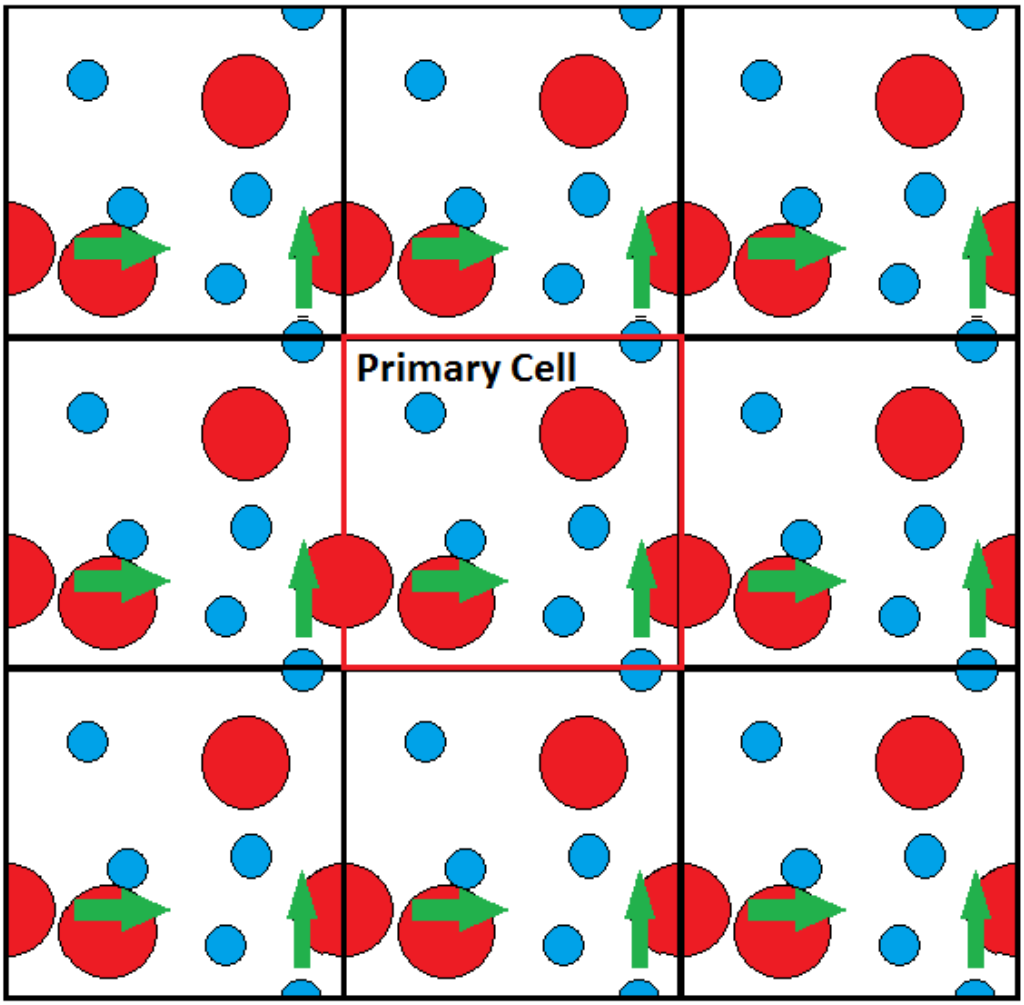

Figure 2.17: Two-dimensional representation of periodic boundary conditions; as an atom passes through a boundary of the primary cell it appears on the opposite side. Only the atoms that cross the primary cell boundary are calculated from the surrounding simulation boxes.

The advantage of this method is that it requires relatively little extra computing power due to the fact only particles crossing cell boundaries need to be accounted for on top of the primary cell trajectories.

2.4 Fundamentals of Proteins - Amino Acids and Protein Structure

Proteins are the building blocks of all complex, multi-cellular organisms. They play a wide range of critical roles within the body such as, but not limited to, DNA replication, the transportation of molecules and catalysing metabolic reaction, allowing cellular functions to carry out as normal. They are defined as large, complex molecules constructed from a linear chain of amino acids. Differences in protein structure and function arise from the differences in their amino acid sequence. The order of amino acids in the linear chain of amino acids, commonly referred to as the polypeptide chain, also determines how a protein folds into its native three-dimensional state, which in turn dictates how the protein functions within a living organism. Polypeptides sequences are longer than 30 residues (amino acids within a chain) and can be as long as 36,000 residues in the case of the protein titin[155]. Amino acid sequences shorter than 30 residues are described as peptides. It is typical to talk about a proteins size in total mass rather than the length of the polypeptide. The unit used to quantify protein mass, rather than grams, is the Dalton. The Dalton is defined as $1/12^{th}$ the mass of a C^{12} atom and is approximately analogous to an atomic mass unit (a.m.u).

Before discussing protein assembly and structure in more detail it is important to look at amino acids in more detail. An amino acid is a simple compound, defined by the presence of a carboxylic acid (-COOH) and an amine ($–NH_2$) functional group with a specific side chain unique to each amino acid. In total 500 amino acids have been documented, with 240 being observed in nature[156], however, of the 240 occurring naturally only 22 are used in the assembly of proteins. This group of 22 amino acids is referred to as the proteinogenic amino acids, 21 of them exist in the standard genetic code of proteins and are directly encoded for protein synthesis, while pyrrolysine depend on special translation mechanisms during construction of

proteins to be included. The 21 coded amino acids can be classified in a variety of ways. One way of classification is through the characteristics of the amino acid side chain. The first group of amino acids have electrically charged side chains at pH 7.4 (The physiological pH of a typically healthy human body.) Arginine (Arg), Histidine (His) and Lysine (Lys) all have positively charged side chains at this pH, while Aspartic acid (Asp) and Glutamic acid (Glu) have negatively charged side chains.

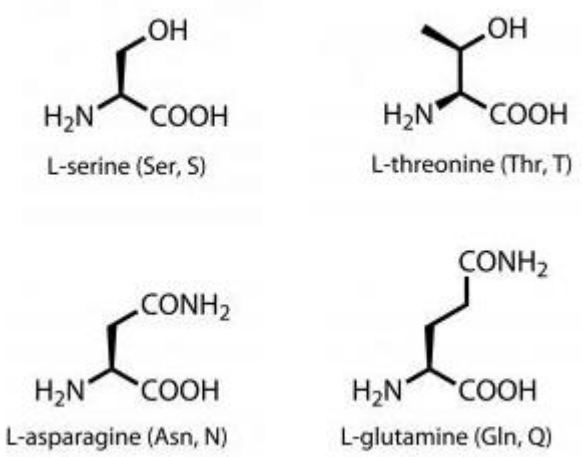

Figure 2.18: Structure of the amino acids with electrically charged side chains at pH 7.4.

The second group of amino acids are characterised through their polar, uncharged side chains. Serine (Ser), Threonine (Thr), Asparagine (Asn) and Glutamine (Gln) are all grouped under this classification.

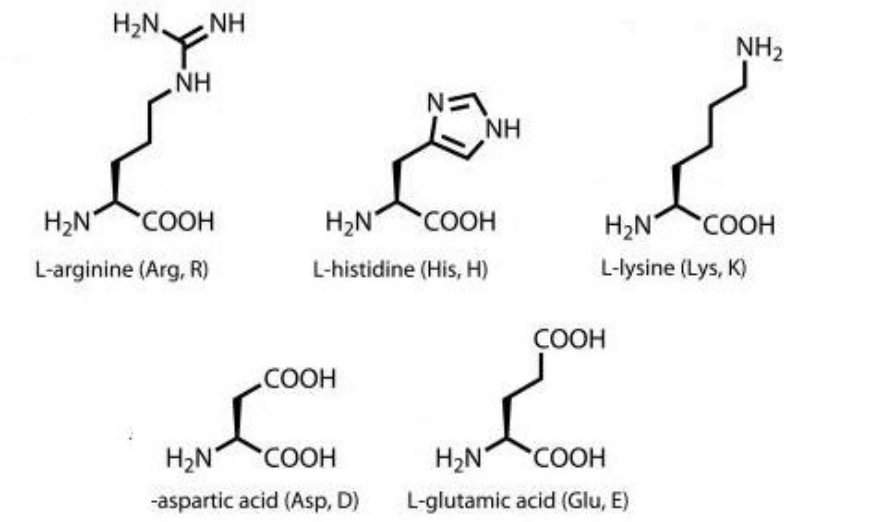

Figure 2.19: Structure of the amino acids with polar, uncharged side chains at pH 7.4.

Thirdly is the largest classification, the amino acids with hydrophobic side chains. Alanine (Ala), Isoleucine (Ile), Leucine (Leu), Methionine (Met), Phenylalanine (Phe), Tryptophan (Trp), Tyrosine (Tyr) and Valine (Val) all fall under this category.

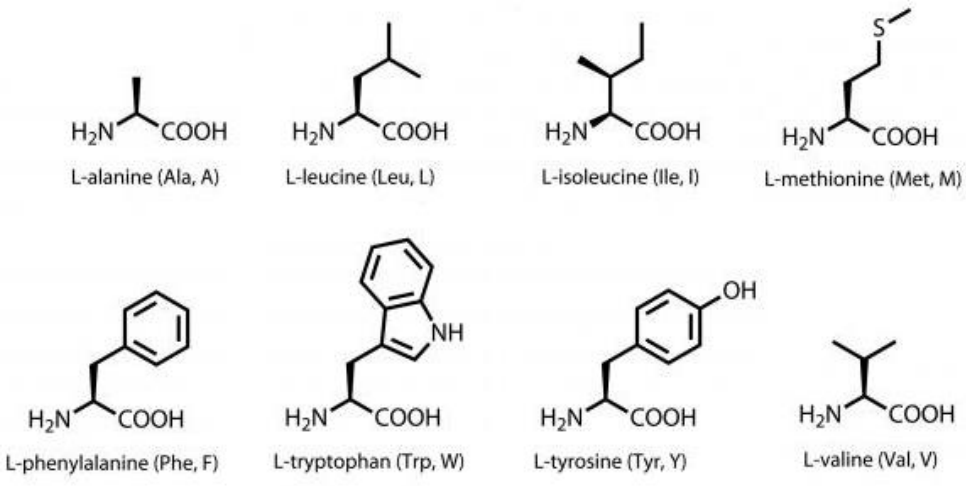

Figure 2.20: Structure of the amino acids with hydrophobic side chains at pH 7.4.

Finally, there are the special cases which do not fall under the other categories. This includes Cysteine (Cys), Selenocysteine (Sec), Glycine (Gly) and Proline (Pro).

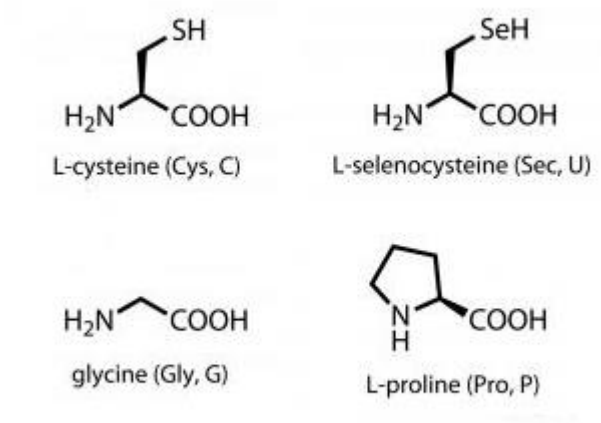

Figure 2.21: Structure of the special case amino acids at pH 7.4.

The forms given in the previous four figures are the standard chemical structures, however in aqueous solutions they exist as zwitterions. A zwitterion is a neutral molecule with positive and negative charges at different points on the molecule itself.

The pKa of the functional groups and side chains of each amino acid are also of interest to the synthesis of protein encapsulated AuNCs and are given in Table 2.1.

Amino Acid	a-carboxylic acid	a-amino	Side chain
Alanine	2.35	9.87	
Arginine	2.01	9.04	12.48
Asparagine	2.02	8.80	
Aspartic Acid	2.10	9.82	3.86
Cysteine	2.05	10.25	8.00
Glutamic Acid	2.10	9.47	4.07
Glutamine	2.17	9.13	
Glycine	2.35	9.78	
Histidine	1.77	9.18	6.10
Isoleucine	2.32	9.76	
Leucine	2.33	9.74	
Lysine	2.18	8.95	10.53
Methionine	2.28	9.21	
Phenylalanine	2.58	9.24	
Proline	2.00	10.60	
Serine	2.21	9.15	
Threonine	2.09	9.10	
Tryptophan	2.38	9.39	
Tyrosine	2.20	9.11	10.07
Valine	2.29	9.72	

Table 2.1: pKa values for amino acids; note that the uncharged side chain amino acids have no pKa value for their side chains.

The pKa is the logarithmic acid dissociation constant. It describes the quantitative strength of an acid in solution. If the pKa value is high, then it is less likely an acid will donate a proton. Associated with the pKa values of amino acids is the isoelectric point. The isoelectric point of a molecule is the pH at which the net charge of the molecule is zero. Since each amino acid has different pKa values the isoelectric point for each amino acid is slightly different. The isoelectric points are shown in Table 2.2.

Amino Acid	**Isoelectric pt.**	**Amino Acid**	**Isoelectric pt.**
Alanine	6.01	Leucine	5.98
Arginine	10.76	Lysine	9.74
Asparagine	5.41	Methionine	5.74
Aspartic Acid	2.77	Phenylalanine	5.48
Cysteine	5.07	Proline	6.48
Glutamic Acid	3.22	Serine	5.68
Glutamine	5.65	Threonine	5.87
Glycine	5.97	Tryptophan	5.89
Histidine	7.59	Tyrosine	5.66
Isoleucine	6.02	Valine	5.97

Table 2.2: Isoelectric point values for amino acids.

Another characteristic of interest to this thesis is the hydrophobicity of each amino acid as they can determine the hydrophobicity of certain areas within a proteins structure. The hydrophobicity of an amino acid at pH 7 is determined using a scale based on the hydrophobicity of glycine, which is neither hydrophobic nor hydrophilic in an aqueous environment. The hydrophobicity of each amino acid is displayed in Table 2.3.

Amino Acid	Hydropathy index	Amino Acid	Hydropathy index
Alanine	1.8	Leucine	3.8
Arginine	-4.5	Lysine	-3.9
Asparagine	-3.5	Methionine	1.9
Aspartic Acid	-3.5	Phenylalanine	2.8
Cysteine	2.5	Proline	-1.6
Glutamic Acid	-3.5	Serine	-0.8
Glutamine	-3.5	Threonine	-0.7
Glycine	-0.4	Tryptophan	-0.9
Histidine	-3.2	Tyrosine	-1.3
Isoleucine	4.5	Valine	4.2

Table 2.3: Overall hydropathy of each amino acid, negative values indicate hydrophilic behaviour, positive values indicate hydrophobic behaviour.

As previously mentioned, a protein is formed by a single long chain of amino acids. The amino acids bond through peptide bonding[157]. Peptide bonds form by linking the α-carboxyl group of one amino acid to the α-amino group of another, resulting in the production of a dipeptide bond and a water molecule, as shown in Figure 2.22.

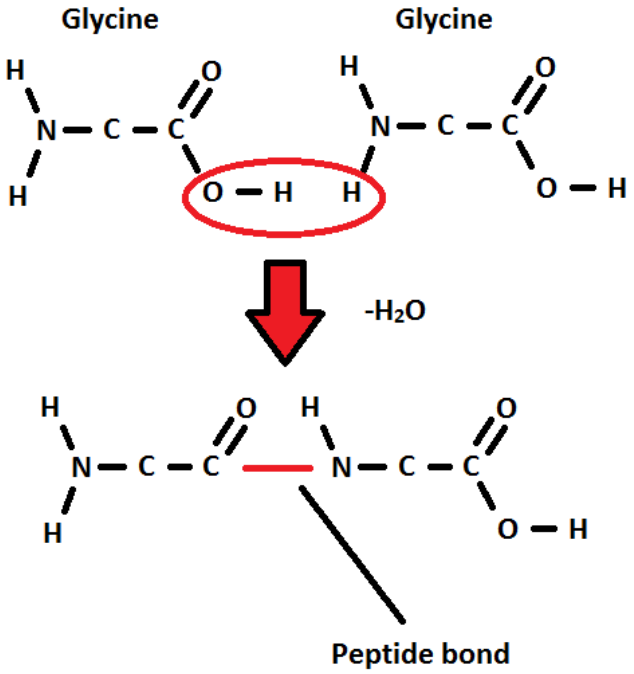

Figure 2.22: Chemical diagram of the condensation reaction which takes place during peptide bonding; in this case the α-carboxyl group of one Glycine bonds to the α-amino group of another by losing one water molecule.

It is possible for the polypeptide to bond to itself via cross-linking. Cross-linking is generally due to disulphide bonding, resulting from the oxidation of the sulphur side chains of two cysteine residues. The disulphide bonds typically give the structure of a protein more rigidity and are more commonly seen in extracellular proteins since they exist in harsher environments in comparison to intracellular proteins which are relatively protected within the cell membrane.

When discussing structure of a protein there are 3 aspects which are commonly taken into consideration. The primary structure has already been discussed and is the amino acid sequence of the complete polypeptide chain is in. It is the backbone of the protein structure and cannot change unless the amino acid sequence is effectively cut in two along the chain or cross-linking bonds are broken. The secondary structure describes local structures within the protein which are repeatable and common for not just one protein. Features such as alpha-helices and beta sheets are described as

secondary structure and are assembled via hydrogen bonding by amide and carboxyl groups in the protein backbone. Alpha-helices are right hand spiralled structures which are formed when every amine group donates a hydrogen bond to the carbonyl group of an amino acid four places previous in the polypeptide sequence. Cross linking is often present in proteins where alpha-helices are present, rigidifying these structures making them less likely to destabilise.

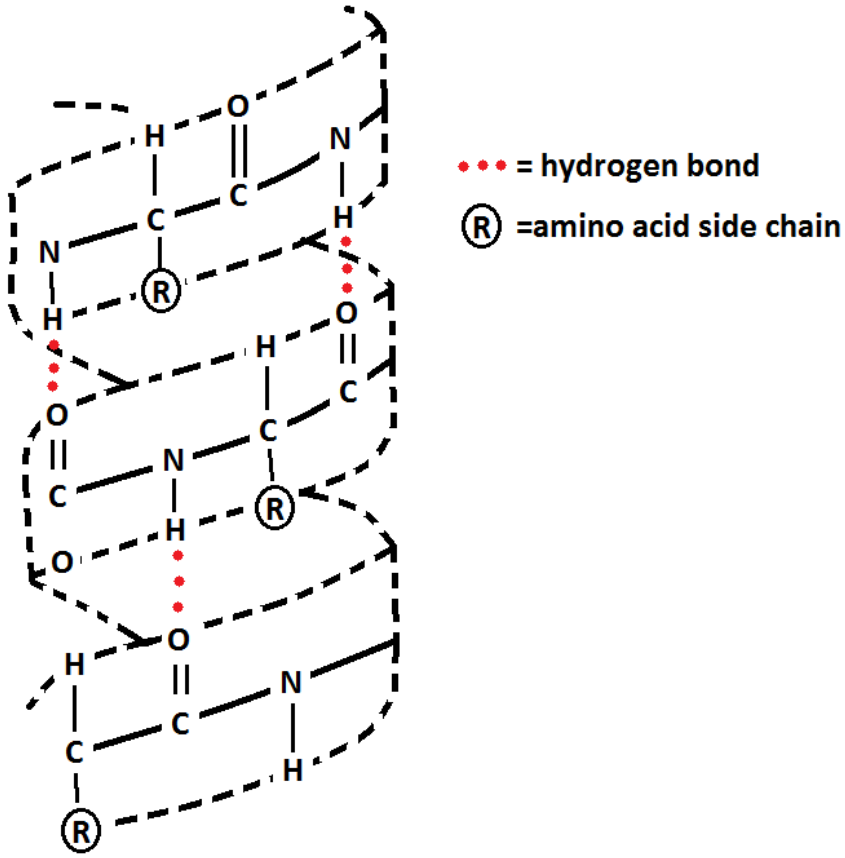

Figure 2.23: 2D representation of the structure of a typical alpha-helix. While hydrogen bonding is relatively weak, the amount of hydrogen bonding taking place along the coil offers enough strength for the secondary structure to keep its shape.

The other most common secondary structure is the beta-sheet. Beta sheets are assembled when hydrogen bonding takes place between the backbones of two or more strands of the polypeptide chain running parallel to one another, forming a twisted sheet. In this formation, all the side chains of the individual amino acids all point upwards in the same direction from the beta-sheet. Depending on the alignment of the polypeptide chain backbone, the beta-sheet can exist in two forms, based on the alignment of hydrogen bonding, either an antiparallel or parallel beta-sheet, shown in Figure 2.24.

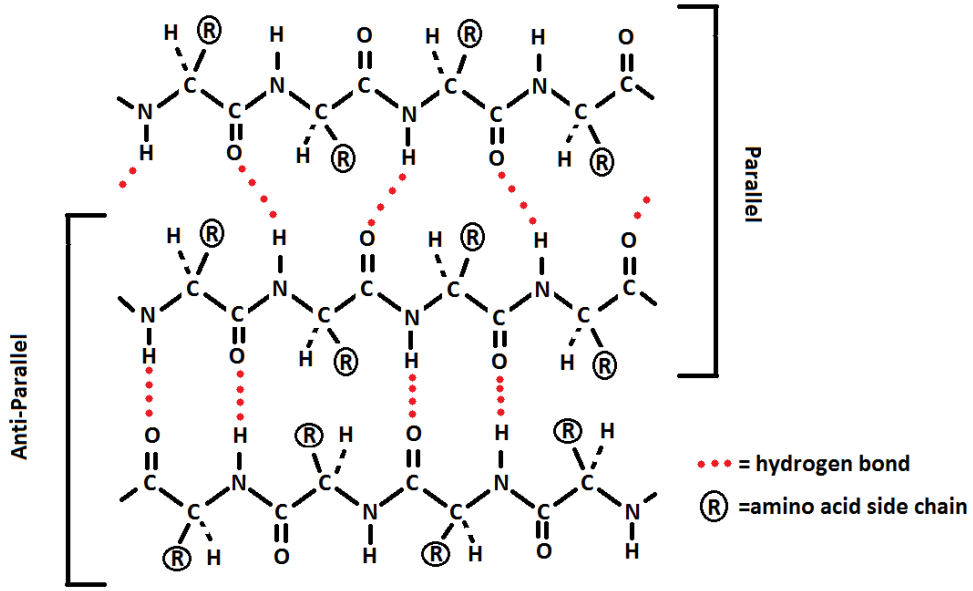

Figure 2.24: Chemical bond representation of both backbone alignment types in the formation of beta sheet secondary structures.

The final important aspect of a proteins structure is the tertiary structure. This describes the proteins geometric shape formed by the backbone and the secondary structures forming distinct domains within the protein itself. The tertiary structure is paramount to a proteins function as the overall shape or conformation of a protein affects how it interacts with its surrounding environment. Many diseases result from changes to a proteins tertiary structure, resulting in it aggregating, forming large

particles or affecting the way it interacts within the body, even changing it to become toxic[158]. The tertiary structure can be defined by the spatial coordinates of all the atoms in a proteins structure. X-ray crystallography and nuclear magnetic resonance imaging are most commonly used to determine the tertiary structure of a protein.

As mentioned previously proteins can be intrinsically fluorescent if their polypeptide chain contains phenylalanine, tyrosine or tryptophan. The side chains of these amino acids contain aromatic rings and can all absorb light to varying degrees at different wavelengths.

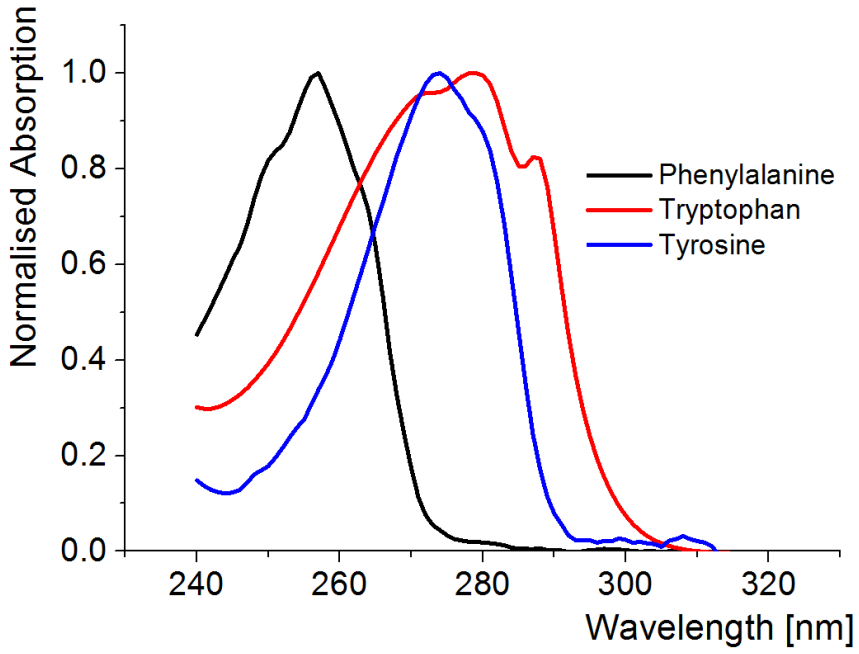

Figure 1.25: Normalised UV-Vis absorption of the fluorescent amino acids Phenylalanine, Tryptophan and Tyrosine.

Tryptophan has a quantum yield of 0.20 and has the highest quantum yield of the three amino acids and is most widely used to sense changes in protein conformation. Tryptophan's absorption profile consists of two bands, one centred on 280 nm and the other at 290 nm. As seen from Figure 2.25, the overlap in absorption between

tryptophan and the other two amino acids allows for the excitation of tryptophan exclusively at approximately 290 nm. The reason for two absorption bands arises from different states the indole ring (5-sided carbon ring – see Figure 2.20) on the side chain can take. Transitions from the π to π^* in the electron-vibration energy in the indole ring are attributed to the two different absorption peaks. Tryptophan can also experience energy transfer from nearby excited tyrosine and to a lesser extent phenylalanine through FRET. Tryptophan is reasonably complex in terms of fluorescence lifetimes. The tryptophan amino acid's fluorescence decay curve is 3-exponential in aqueous solution. These three fluorescent species arise from different rotamer forms (conformational isomers of the molecule which exist in nature) the amino acid can take[159].

2.5 Physicochemical Characterisation Techniques

2.5.1. Determination of Particle Size via Dynamic Light Scattering

The size of molecules can be measured via Rayleigh scattering of light if the particle size is small in comparison to the scattered light's wavelength, typically below sizes of 20 nm[160]. Rayleigh scattering is the elastic scattering of light by particles smaller than the incident light's wavelength. As an elastic process the total energy of the incident light is equal to that of the scattered and the particle which scatters the light remains unchanged[161]. If a monochromatic and coherent laser source of light is focussed on a liquid medium containing small particles undergoing Brownian motion, then the intensity of scattered light will fluctuate due to changes in distance between scattering particles in solution over time. The surrounding particles will cause scattered light to undergo constructive or destructive interference which results in the intensity fluctuations previously mentioned. Within these fluctuations information describing movement timescales of the scattering particles can be retrieved. This information can then be converted into particle sizes using the autocorrelation function.

The apparatus setup consists of a monochromatic laser source which is vertically polarized and shot into a sample contained in a light sealed box.

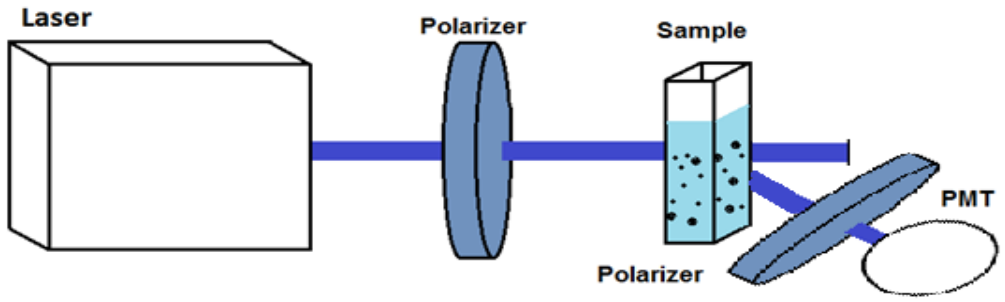

Figure 2.26: Experimental setup for a typical DLS measurement.

The scattered light is then passed through a second polarizer and into a photomultiplier which monitors the intensity of scattered light. This process is repeated continuously so that many scattering events take place as the particles move in solution under Brownian motion[162]. The differences in constructive and destructive light from all diffracting particles in solution is then analysed by an auto correlator, comparing the intensity of scattered light over time. The dynamic information of the scattering particles is calculated from the auto correlation curve using Equation 2.26.

$$g^2(q;\tau) = \frac{<I(t)(t+\tau)>}{<I(t)>^2} \qquad [2.26]$$

Where: $g^2(q; r)$ = the auto correlation function at a wavelength q, and time τ

I = intensity of incident light [$W.m^{-2}$]

The autocorrelation function decays exponentially with time; this is due to the lack of correlation between two scattered light events after a longer period. The long period allows the scattering particles to move. This movement results in the light being scattered differently. The exponential decay of the autocorrelation function is fitted using numerical methods based on a sample which has polydisperse scattering particles present. The autocorrelation function consists of a sum of exponential

decays, as shown in Equation 2.27; where each decay corresponds to a different particle size in the total sample population.

$$g(q;\tau) = \int G(\Gamma) \exp(-\Gamma\tau)\, d\Gamma \quad [2.27]$$

Where: Γ = decay rate [s^{-1}]

The decay rate can then be expressed as a function of the translational diffusion coefficient, D_t, and wave vector as shown in Equation 2.28.

$$\Gamma = q^2 D_t \quad [2.28]$$

The wave vector of the experimental setup can be found via Equation 2.29.

$$q = \frac{4\pi n_0}{\lambda} \sin\left(\frac{\theta}{2}\right) \quad [2.29]$$

Where: n_o = refractive index of the sample

λ = laser wavelength [m]

θ = the angle of the detector with respect to the sample cell [°]

The hydrodynamic radius can then be calculated via the Einstein-Smoluchowski relation for the diffusion of spherical particles through a liquid with a low Reynolds number.

$$D_t = \frac{k_B T}{6\pi\eta r} \quad [2.30]$$

Where: k_B = Boltzmann constant

T = absolute temperature [K]

η = dynamic viscosity [$kg.m^{-1}.s^{-1}$]

r = the radius of a spherical particle [m]

2.5.2 Determination of Zeta Potential via Electrophoretic Mobility

It is possible to measure the potential difference between a surface of a particle in solution and the bulk of the liquid, referred to as a particle's zeta potential, via electrophoresis. Electrophoresis describes the motion of charged particles in a conducting liquid as a result of applying a uniform electric field – typically via a cathode and anode. A negative charge is applied to the liquid causing positively and negatively charged particles to move towards the electrodes which they are attracted to, overcoming friction and the electrophoretic retardation forces. The surface charges of particles in liquids are screened by a diffuse ion layer which has a charge of the same magnitude but opposite sign of the particle surface charge.

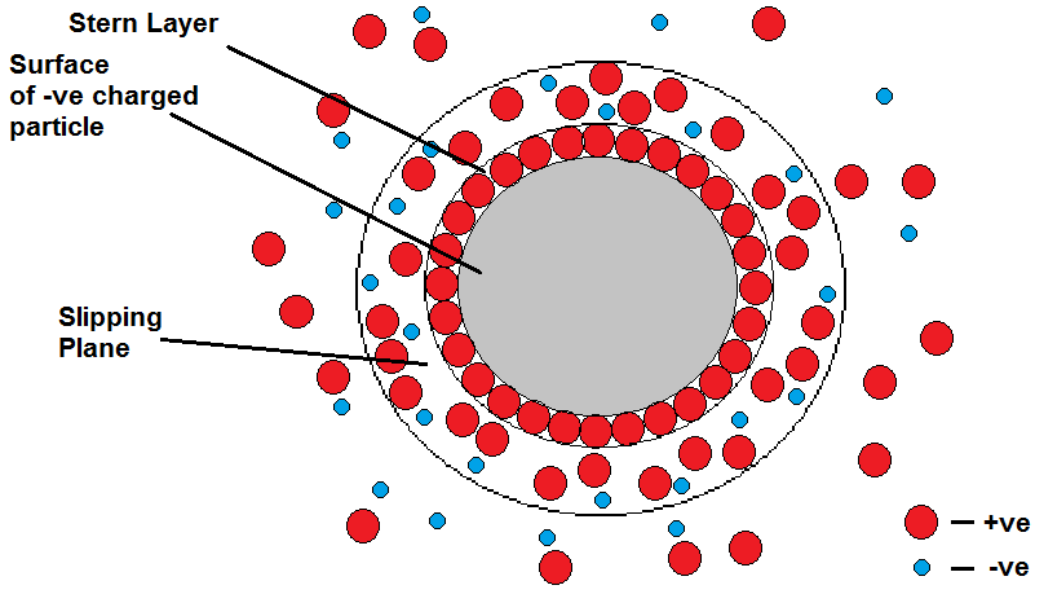

Figure 2.27: A negatively charged surface of a particle suspended in a medium. The Zeta potential comes from the overall charge at the slipping plane surface.

The overall force applied to a particle moving through an applied electric field in a liquid is zero when moving at constant speed. The drift velocity, v, of a particle in a strong electric field in a liquid with a low Reynolds number can be described as proportional to the applied field, E, defining the electrophoretic mobility, μ_e (the

ability of a charged particle to move through a medium) in Equation 2.31, known as Henry's Equation[163].

$$\mu_e = \frac{v}{E} = \frac{2\varepsilon_r \varepsilon_0 \zeta}{3\eta} \quad [2.31]$$

Where: ε_r = dielectric constant of the dispersion medium

ε_o = permittivity of free space [10^{-12}. m^{-3}.kg^{-1}. s^4. A^2]

ζ = zeta potential [V]

η = dynamic viscosity of the dispersion medium [$kg.m^{-1}$. s^{-1}]

The drift velocity can be measured via Laser Doppler Velocimetry (LDV). Two coherent, monochromatic lasers are crossed in the sample cell, where the two beams interfere with one another. As the particles move through the laser intersection they reflect the lasers and the changes in intensity are detected by a photodetector. The frequency in fluctuation of detected scattered light intensity is equivalent to the Doppler shift between both incident and scattered light and can be converted into a velocity for scattering particles, since the Doppler shift is proportional to particle velocity.

The measured particle velocity is then used to calculate the electrophoretic mobility and converted into zeta potential values which are used to quantify the magnitude of net electrical charge of a particle in solution.

2.5.3 Determination of Liquid Viscosity

The viscosity of a fluid is simply the drag caused by the relative motion of a fluid on a surface it flows past. To successfully measure viscosity, the flow must be laminar; therefore, a liquid must have a small Reynolds number[164]. A rolling ball viscometer was utilised throughout this thesis; the advantage of this method is that it utilises micro capillaries, and therefore only a small sample volume (5 ml) is needed to calculate viscosity. A metal ball is passed through the capillaries under gravitational

forces and the time of flight for the ball to pass through two optical beams is recorded.

To calculate the dynamic viscosity of a liquid both the density of the rolling ball and the sample density must be known (calculation of the sample density will be explained in **2.5.4 Measuring the Density of Liquids***)*, the relationship between dynamic viscosity and sample density is shown in Equation 2.32.

$$\eta = K(\rho_b - \rho_s)t_r \qquad [2.32]$$

Where: η = dynamic viscosity [mPa.s]

K = proportionality constant

ρ_b = ball density [g.cm^{-3}]

ρ_s = sample density [gcm^{-3}]

t_r = time of flight for the ball [s]

2.5.4 Determination of the Density of Liquids

The digital oscillating U-tube method was used throughout this thesis to determine the density of liquids. The oscillating U-tube method is based on the Mass-Spring model; the liquid sample is used to fill a glass U-tube which can oscillate. The U-tube is excited mechanically to oscillate at its lowest un-dampened frequency. The natural frequency of vibration is influenced by the samples mass. Since the volume of the liquid within the U- tube does not change, the mass does not change and the frequency of vibration can allow the density of the sample to be determined. The oscillation of the tube is converted into an electronic frequency via electromagnets.

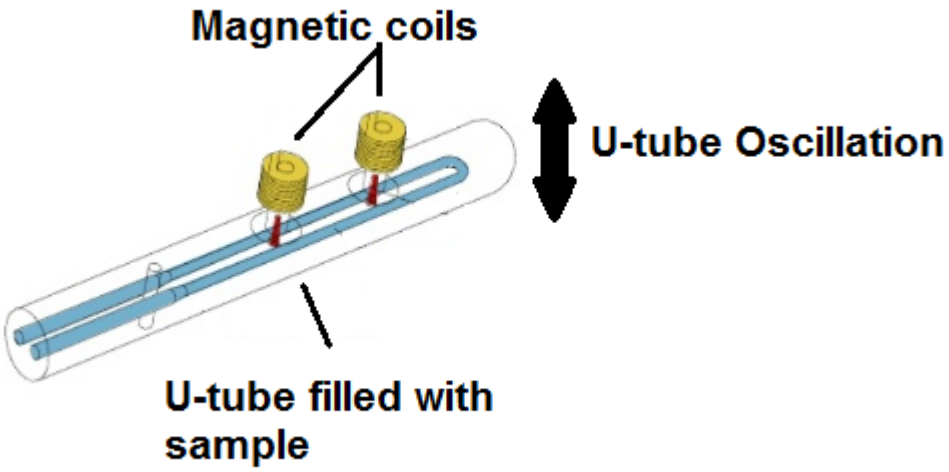

Figure 2.28: Experimental setup of the U-tube densitometer

The period of oscillation is then used to calculate density using Equation 2.33.

$$\rho = A\tau^2 - B \qquad [2.33]$$

Where: ρ = density of liquid [g.cm^{-3}]

A = instrument constant

B = instrument constant

τ = period of oscillation [s]

The instrument constants can be found by measuring the density of substances of which the densities are already known. For all experiments the densities of water and air were used.

2.5.5 Theory Quartz Crystal Microbalances

The resonant frequency of a piezoelectric quartz crystal resonator is utilised to measure changes in mass on the nano gram scale, deposited on a surface. A Quartz Crystal Microbalance (QCM) consists of a thinly cut quartz disc with gold electrodes plated on either surface to allow a current to pass through the quartz crystal. An electrical potential applied through the electrodes causes mechanical stress within the quartz crystal. This mechanical stress can be thought of as an acoustic wave propagating through the crystal, reaching minimum impedance when the crystal thickness is a multiple of half the acoustic wavelength[165]. By setting up a constant oscillation in which the acoustic wave travels perpendicular to the crystal surface, it is possible to calculate the total mass adsorbed to the sensor surface. A QCM is said to be operating in shear mode when these conditions are met regarding the direction of acoustic wave in the crystal[166]. The deposition of material as a thin film on the sensor surface results in a decrease in the frequency the crystal is resonating at. This change in frequency is proportional to the mass adsorbed on the surface, thus allowing for the mass to be calculated.

A resonant frequency is setup in the crystal by matching the acoustic oscillation with the electrical oscillation near to the fundamental frequency of the crystal being used in the sensor. The fundamental frequency is determined by the crystal characteristics. Its thickness, chemical structure, shape and adjacent medium are constants and do not change, whereas the mass of the crystal changes with the deposition of material on the crystal surface[167], first shown by Sauerbrey *et. al.*

$$\Delta f \propto K\,\Delta m \qquad [2.34]$$

Where: Δf = change in fundamental frequency [Hz]

K = constant associated with the crystal characteristics

Δm = change in deposited mass on sensor surface [g]

When the QCM sensor is submerged in solution the frequency of oscillation will change. The factors that determine the new fundamental frequency are based on the characteristics of the solvent adjacent to the sensor surface. When the layer over the sensor surface is thick, the relationship between Δf and Δm also becomes non-linear. To correct for these factors Kurosawa *et. al.* observed that Δf is a linear function of the viscosity and density of the liquid[168,169] shown in Equation 2.35.

$$\Delta f = f_0^{3/2} \left(\frac{\rho \eta}{\pi \eta_q \rho_q} \right)^{1/2} \quad [2.35]$$

Where: f_0 = fundamental frequency of the quartz crystal [Hz]

ρ = liquid density [$g.cm^{-3}$]

η = liquid viscosity [$kg.m^{-1}.s^{-1}$]

ρ_q = water density [$g.cm^{-3}$]

η_q = water viscosity [$kg.m^{-1}.s^{-1}$]

3 Locating the Nucleation Site of AuNCs within Serum Albumin Proteins

3.1 Abstract

Protein encapsulated AuNCs are a new class of highly stable, non photobleaching fluorophores[51]. Due to these unique fluorescent properties, this new type of fluorescent probe has potential to be utilised for biological imaging and sensing. Proteins which contain tyrosine and cysteine amino acids within their polypeptide chain in the correct ratios can act as the nanocluster template, offering a wide variety of proteins in which AuNCs can be grown. Serum albumin of both bovine and human variety have been extensively studied, however questions about how and where gold nucleates within BSA and HSA during synthesis have yet to be answered.

In this study, evidence of the location of nucleated AuNCs within BSA and HSA are presented. Fully atomistic molecular dynamics studies of BSA interacting with randomly introduced Au atoms were combined with experimental spectroscopic studies of HSA-AuNCs in changing pH. These were carried out in conjunction with FRET based studies on the separation between the single tryptophan residue present in HSA and the AuNC itself. The combination of both experimental and computational data revealed that the major binding site for AuNCs within BSA and HSA is at the bottom of the heart shape protein in domain IIB, close to the Sudlow I drug binding site. Knowledge of the major AuNC binding site and the surrounding residues will aid in the understanding of the AuNC fluorescence mechanism and their optimisation as a fluorescent probe.

3.2 Introduction

It is of the upmost importance to understand the structure and function of a biomolecule when using it as a scaffold to synthesize fluorescent metal nanoclusters. Both BSA and HSA have been used as a model protein for AuNC synthesis due to their abundance and the well-studied nature of both proteins. Serum albumin predominantly acts as the major transportation molecule in the blood stream; carrying fatty acids, hormones and many other molecules, including drugs, throughout the body[170]. Comparatively both BSA and HSA share the same tertiary and secondary structures however there are some differences within the primary structure of both proteins. The polypeptide sequence of HSA and BSA share a 76 % homology[171], also highlighting the close similarities of the two proteins. Despite the difference in the polypeptide sequences both proteins weigh on average between 66.0 kDa - 66.7 kDa, depending on the literature quoted[170,172]. The primary structure of serum albumin can be described as heart shaped with dimensions of 84 x 84 x 31.5 Å[173]. Despite the proteins large size, it is still relatively rigid due to several disulphide bonds cross-linking three domains within the protein. The main structure of serum albumin is alpha-helical in nature with each domain consisting of 2 long loops of alpha helices and one shorter loop. Each domain is split up into 2 subdomains, the first consisting of the two long loops and the second domain consisting of the one shorter loop. The heart shape of the protein is the natural conformation of the protein in natural conditions (pH 7.4, temperature 37 °C) however the protein undergoes conformational changes depending on the pH of its environment. There are five well defined conformations of serum albumin depending on the pH of its environment. As previously mentioned the proteins take on a heart shape at pH 7.4, this is known as the 'normal' form and exists in pH 4.3 - 8.0[174]. At pH values between 4.3 and 2.7 the proteins take on a partially unfolded state known as the 'fast' form. Lowering the pH below 2.7 results in the proteins taking on a fully unfolded conformation known as the 'extended' form in which the protein is exposed to the surrounding environment. At pH between 8.0 - 10.0 the protein takes on the 'basic' form in which the heart shape is retained but hydrophobic areas of the protein bury themselves further into the protein structure. At pH above 10.0 the protein takes on the 'aged' form which keeps the heart shape conformation of the normal and basic

form. It is referred to as the aged form due to the ageing process the protein undergoes at this pH. The process is catalysed by free sulfhydryl and results in conversion of sulfhydryl at its origin position. This aging process allows the protein to retain its normal shape and does not undergo the transition from normal to fast conformations[175]. In terms of this chapter of work it is important to note that in terms of fluorescence behaviour both are also similar in their absorption and emission profiles; however, BSA contains two fluorescent tryptophan residues whereas HSA contains only one, making energy transfer analysis between tryptophan and AuNC more simplistic in nature. The tryptophan is found at position 214 in the polypeptide chain placing the residue in domain II, near the centre of the protein, whereas in BSA the positions are separated across domains I and II, in positions 134 and 213. The single tryptophan has been shown as a useful FRET donor in HSA; successfully measuring the separation distance between it and a prodan dye attached to the single free cysteine in position 34 in the polypeptide chain under protein unfolding[176], showing the feasibility of utilising the single tryptophan and single acceptor fluorophores to measure Angstrom scale distances within dynamic systems.

To intelligently optimize the properties of protein encapsulated AuNCs it is paramount to have a clearer understanding of how these protein-gold complexes form during synthesis. Studies concerning the fluorescence characteristics of AuNCs have been undertaken in the past. The fluorescence characteristics of HSA-AuNCs and BSA-AuNCs have been shown in the literature to be the same under matching solvent conditions[177,178]. The absorption band of AuNCs has been seen to be broad, resulting in unusually wide excitation band from 280 nm to 470 nm[178]. It has also been shown that tryptophan can undergo FRET with the AuNC illustrating that there are at least two pathways of excitement for AuNCs[147]. The position of the peak emission has been reported between 670 - 710 nm, however some care must be taken as not all published spectra are correctly calibrated for detectors which are biased towards shorter wavelength photon detection. The overall quantum yield of the AuNCs emitting in the red regime has also been reported at different values ranging from 1 - 8 %[51,179]. Quantum yield of AuNCs encapsulated in serum albumin have also been shown to be dependent on solvent type and temperature of solution[150]. The quantum yield of the AuNCs has been shown to be one of the major barriers in the

widespread use as a fluorophore in bio-imaging[180]. Of most interest to all protein encapsulated AuNCs is the extremely long lived fluorescence lifetimes. Fluorescence lifetimes have been reported, one around 1μs and another longer fluorescence lifetime of 2-2.5 μs[150,181]. Studies have been carried out to explain the source of a 2-exponential fluorescence decay. Wen *et. al.* revealed two bands of fluorescence emitted by the AuNCs, the spectrum was observed to consist of a major band with a peak of 710 nm and a weaker band with a peak of 640 nm[182]. From temperature based experiments carried out by the group the origin of the major band was attributed to the core of the nanocluster while the weaker band was assigned to the surface-protein bonded shell. The core of the AuNCs is icosahedral shaped, consisting of 13 Au(0) atoms while the shell structure takes on a [S-Au(I)-S-Au(I)-S] motif, with the sulphur sourced from sulphur groups within the protein. This core/shell model has also been suggested in other literature[51]. Further work carried out by Wang *et. al.* also observed two bands within red fluorescent ligand encapsulated AuNCs at the same positions as protein encapsulated AuNCs. It was found that not only does the fluorescence originate from the core/shell structure but the fluorescence characteristics of the AuNCs can be altered depending on the type of ligand used to form the shell structure. The overall charge of the AuNC was found to be the factor determining the changes to the fluorescence characteristics and it is possible that the AuNC charge could also play a role in altering the fluorescence characteristics of protein encapsulated AuNCs[47].

One critical area which has not fully been explored is the nature of the synthesis and how gold atoms interact with the protein surface and nucleate inside proteins. While much speculation has been made as to the exact process of AuNC nucleation within proteins using the one-pot method developed by Xie *et. al.*, only a few studies have attempted to uncover information about the synthesis method itself. Xu *et. al.* studied how the number of different residues affected the AuNC formed by comparing the synthesis of AuNCs using different proteins[183]. This work also adds further weight to the idea of a core/shell model for protein encapsulated AuNCs due to the lack of growth of AuNCs within protein that do not contain sulphur groups – a critical part of the shell structure as previously discussed. XPS data taken of protein encapsulated

AuNCs have also shown gold sulphur bonding present, further adding weight to the shell/core model[183].

Pyo *et. al.* have made interesting discoveries on the fluorescence mechanism associated with the two fluorescence bands associated with AuNCs fluorescence[184]. They have reported on the origin of fluorescence emission from thiolate encapsulated AuNCs, in which they probe the fluorescence mechanism by rigidifying the AuNC via tetraoctylammonium (TOA) or via freezing. They describe the emission from AuNCs as phosphorescence due to the large Stokes' shift and microsecond lifetimes. Due to the lack of aggregation of their AuNCs under freezing and a large increase in quantum yield the luminescence model which best described their observations was a ligand-to-metal-metal charge transfer relaxation, which occurred at a triplet metal-centred state in gold shell of the AuNCs rather than the core. The group describes the full luminescence dynamics upon excitation of the AuNCs as first a femtosecond relaxation of the gold core state to the shell state. From this state, intersystem crossing takes place to a triplet state which then relaxes to a lower luminescent triplet state that has a high affinity in charge transfer to the surrounding ligands. Upon freezing the ability of the second triplet state to transfer charge is lost due to reduced solvent interactions and the luminescence predominantly occurs from the higher energy, brighter triplet state.

The position of the AuNCs within proteins has never been explored, information which is critical to improving the fluorescent capabilities of these fluorophore complexes through intelligent engineering of the protein's local environment or alteration of the protein itself. Here in this chapter we present a dual approach to uncovering the location of AuNC nucleation within serum albumin using both fluorescence studies and molecular dynamics simulations.

3.3 Experimental

3.3.1 Sample Preparation

BSA-AuNCs were prepared using an unmodified version of the widely used one-pot method, devised by Xie *et. al.*[51] Initially solutions of gold salt and protein were prepared at room temperature directly before synthesis. 51 mg of Chloroauric acid (chemical formula $HAuCl_4$) was dissolved in 15 ml of water providing a solution with a concentration of 10 mM. 750 mg of BSA was dissolved in 15 ml of water, providing a solution of 750 μM. The two solutions were heated and mixed together using a magnetic stirrer bar and hot plate with stirring functionality at 37 °C for 2 minutes. 1.5 ml of NaOH, with a concentration of 1.0 M, was added to the solution to increase the pH above 10. The solution was then continued to be stirred and heated for a further 6 hours. To control the temperature more accurately, a 3 L water bath kept at a temperature of 37 °C was used during the 6 hrs of stirring and heating. The solution was then removed from the water bath and stored in an oven at 37 °C for 48 hrs. BSA-AuNCs were dialysed into buffer solutions using dialysis cassettes with a molecular weight cut off (MWCO) of 40,000 Da to remove any impurities from the BSA-AuNC solution and control the pH. Buffer solutions of pH 1.0, 7.0 and 12.0 were prepared by dissolving buffer salt tablets in water. For each pH, BSA-AuNCs were dialysed in 2 L of buffer solution for 24 hrs. This process was repeated for a total of 3 times, replacing the buffer solution each time, for each pH. Each samples' pH was verified at the end of dialysis using a Horiba electronic pH probe. Before any measurements were carried out, solutions were diluted to 10 % and pH was readjusted using HCl or NaOH when needed.

HSA-AuNCs were similarly prepared using the above protocol. Measurements of natural BSA and HSA were carried out using proteins which underwent dialysis treatment as above.

All chemicals used within this chapter were supplied by Sigma Aldrich, Dialysis cassettes and accessories were supplied by Fisher Scientific.

3.3.2 Fluorescence Measurement and Data Analysis

All fluorescence emission and excitation spectra, including 3D emission/excitation matrices (EEMs), were acquired using a Horiba Fluorolog 3. Emission and excitation spectra were measured with a resolution of 1 nm, whereas 3D EEM measurements were carried out with a resolution of 10 nm to keep measurement times as short as possible to avoid any fluctuations with the sample environment over time. All time resolved fluorescence lifetime measurements were performed on an IBH Fluorocube fluorescence lifetime system equipped with an emission monochromator, utilising the TCSPC technique for nanosecond regime fluorescence lifetimes and the MCS technique for microsecond regime fluorescence lifetimes. Both Laser diode and LED based light sources were used for all fluorescence lifetime measurements. The pulsed laser diode operated at a 1 MHz repetition rate (with an excitation wavelength of 482 nm) and the LEDs operated at a repetition rate of 2 kHz (with excitation wavelengths 295 nm, 377 nm and 471 nm). 100 ns and 13 μs TACs were used to measure protein fluorescence lifetimes and AuNC fluorescence lifetimes respectively using the TCSPC method. A 340 μs TAC was used for all measurements carried out using MCS. All fluorescence lifetime data analysis was carried out using the nonlinear least squares method with the IBH iterative reconvolution software: DAS6. To find the fluorescence lifetimes associated with decay associated spectra, a global fit method was applied to the sum of all the datasets measured. The fluorescence lifetimes gained from the fitting were then used as fixed variables across each individual data set; for each emission wavelength measured at, to calculate the relative intensities of each fluorescence lifetime in each decay curve. The standard deviations associated with the calculated lifetimes were obtained from fitting to the parabola that defines the minimum in the chi-squared goodness of fit parameter.

The Förster distance for tryptophan and AuNC was calculated using Equation 2.8. The separation between Tryptophan and AuNC within HSA was then calculated using Equation 2.7, where the efficiency of the energy transfer, E was given by Equation 2.10.

3.3.3 Theoretical Modelling

Gold atoms were randomly added to a molecular dynamics model of a BSA protein (3V03), downloaded from the Protein Data Bank[185]. The CHARMM27[186] force field was used in conjunction with NAMD 2.8[187] to produce the simulation. The simulation was setup to best emulate the synthesis conditions of BSA-AuNCs used in the laboratory. The protein was solvated in a water box with dimensions 1.16 nm x 0.89 nm x 1.01 nm, and neutralised using NaCl at an ionic strength of 0.05 M. The total atom count for the total system was approximately 93,000 atoms. Initially the system was equilibrated for 300 ps at a constant temperature of 300 K. This yielded a pH of 7 for the overall system. After equilibrium 25 gold atoms were introduced to the system randomly and allowed to disperse for 100 ns. The simulation was then continued further, introducing another 25 atoms to the system and running for a further 100 ns. This protocol was repeated for 600 ns at which point the simulation contained a total of 150 gold atoms. This protocol was applied to two systems; one in which BSA disulphide bonds were present and one in which they were not. For electrostatic interactions, the PME method, discussed previously was used. Parameters proposed by Heinz *et. al.*[188]. for the gold atom potentials were used (Lennard-Jones parameters of ε = -5.29 Å and R_{min} = 1.4755 Å).

Visual Molecular Dynamics (VMD) was used to track the interaction and final positions of gold atoms within the simulation. VMD was also utilised to calculate the separation distances between potential gold cluster nucleation sites within serum albumin and the single tryptophan of HSA using a HSA model (4K2C) downloaded from the protein data bank[189]. All Molecular Dynamics images herein were also produced using VMD. All molecular modelling and visualisation of the simulations was carried out on the ARCHIE-WeSt supercomputer.

3.4 Results and Discussion

3.4.1 Molecular Dynamics Simulations of BSA-AuNCs

Initially the way in which individual gold atoms were interacting with the protein surface was studied at the start of the simulation for both systems (with and without disulphide bonds present). It was found that for 150 gold atoms in both cases the majority interacted with the protein surface, predominantly within 1 ns of the simulation, as shown in Figure 3.1.

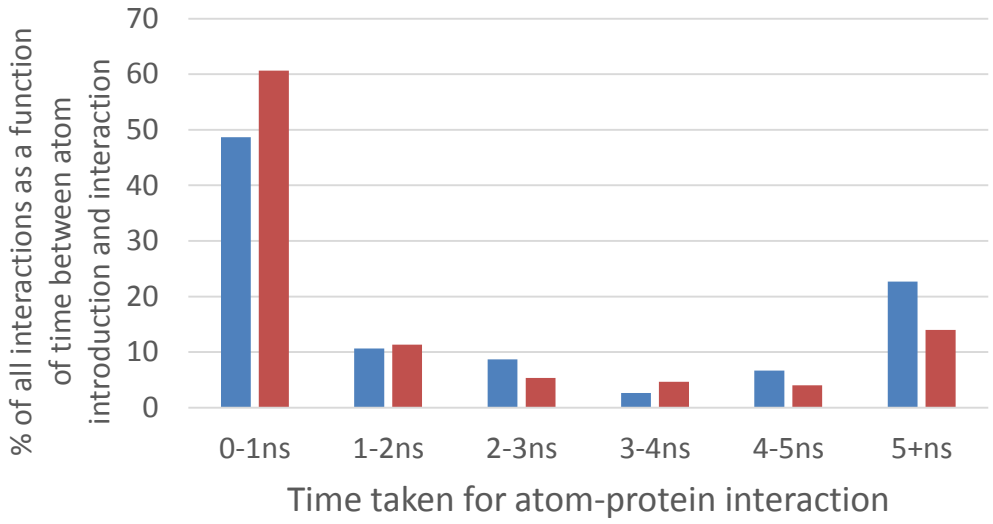

Figure 3.1: The initial uptake for gold atoms onto the protein surface are shown as a percentage of all atoms introduced to the simulation vs time taken for each individual atom to interact with the protein surface. Blue indicates times for the system with disulphide bonds intact, orange indicates times for the system in which disulphide bonds are broken.

The uptake of gold atoms in the system with no disulphur bonds was found to be quicker due to the proteins increased flexibility (disulphide bridges offer the protein increased rigidity across its backbone structure, with none present, the protein loses its rigidity, becoming more flexible). The sudden increase in gold atoms interacting

with the proteins after >5 ns compared to 4-5 ns was due to the formation of small AuNCs 2 gold atoms in size in the water box before interaction with the protein surface, indicating that larger AuNCs do not so readily interact with the protein surfaces. The location of the initial gold-protein surface interaction for all atoms in the case of both systems was also observed, tracking what type of protein residue the gold atoms favoured, as seen in Figure 3.2.

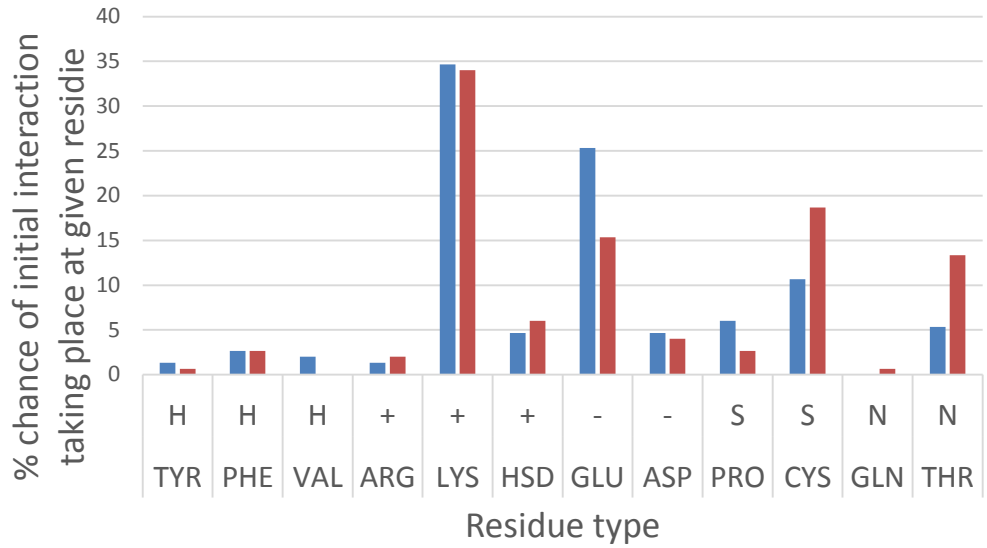

Figure 3.2: The percentage chance of a gold atom interacting with a given residue on the protein surface is shown. Blue indicates times for the system with disulphide bonds intact; orange indicates times for the system in which disulphide bonds are broken.

The initial gold – protein surface interactions were found to take place near the surface of hydrophobic pockets formed by predominantly lysine and glutamic acid. Initial interactions with cysteine were also surprisingly common; due to the proximity between cysteines and the hydrophobic pockets within the BSA protein. The system with disulphide bonds broken presented nearly twice the amount of gold-cysteine interactions initially. This can be attributed to the ease with which sulphur

can be accessed in this system in comparison with the system with disulphide bonds still intact.

After 600 ns of the trajectories, both simulations clearly showed that the gold atoms nucleated close to cysteine residues located within hydrophobic pockets within the protein, as shown in Figure 3.3 and 3.4.

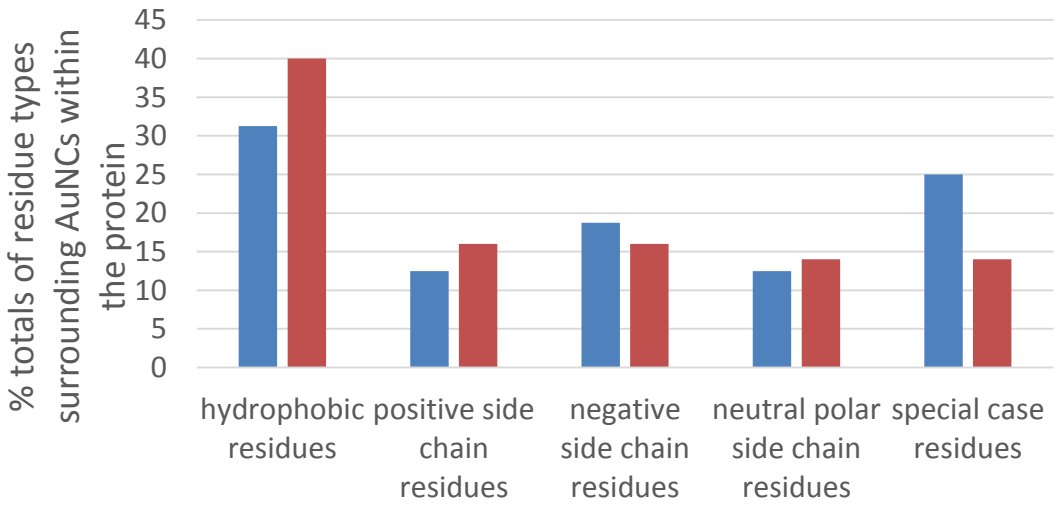

Figure 3.3: The percentage chance of residue types surrounding the gold atoms nucleated inside the protein after 600 ns of the simulation is shown. Blue indicates times for the system with disulphide bonds intact; orange indicates times for the system in which disulphide bonds are broken.

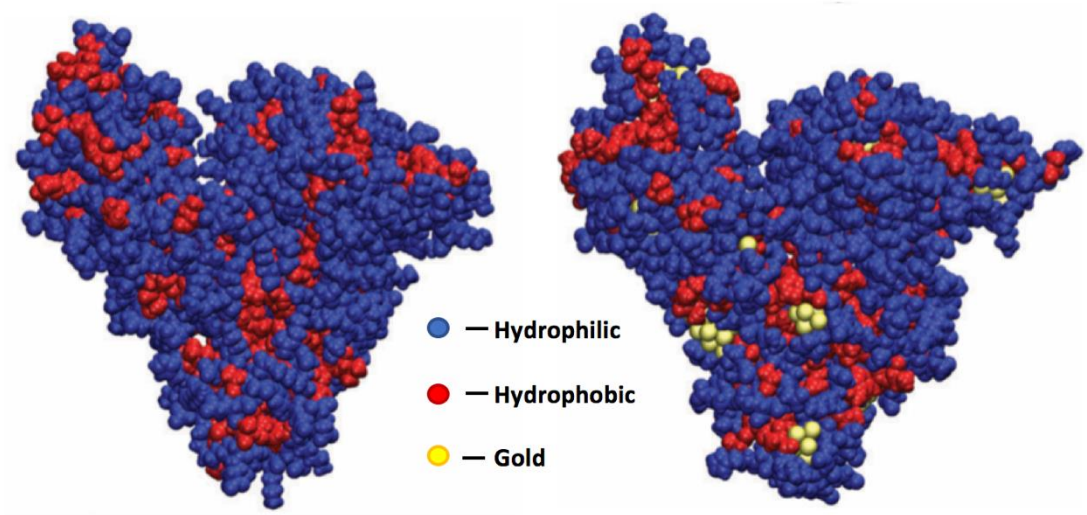

Figure 3.4: The hydrophobicity of the protein surface is shown. Left shows the protein surface before gold is introduced to the simulation, right shows the protein surface after gold has nucleated within the protein. Hydrophobic regions are represented by blue while hydrophilic regions are represented by red. AuNCs not fully buried under the protein surface are represented by yellow, and can only be seen binding to hydrophobic regions of the protein.

The high affinity for gold to bind to sulphur within protein encapsulated AuNCs systems, as shown from previous XPS experimentation[51,53] agrees well with this result. As explained previously, MD simulations do not model bonding; however, this result suggests that it would be highly likely the AuNCs bind to the protein in the manner suggested. In both simulations, it was found that the AuNCs formed were 3 - 13 atoms in size. The formation of multiple smaller AuNCs within the protein was unexpected since previous studies have shown the formation of AuNCs of around 25 atoms[190]. One explanation which could explain this result is the fact gold atoms were randomly introduced to the system, rather than focused onto one part of the protein. This resulted in the gold atoms interacting with residues at all points on the protein surface and then migrating to the nearest cysteine residues. The positions of the AuNCs for simulation with disulphide bonds intact can be seen in Figure 3.5.

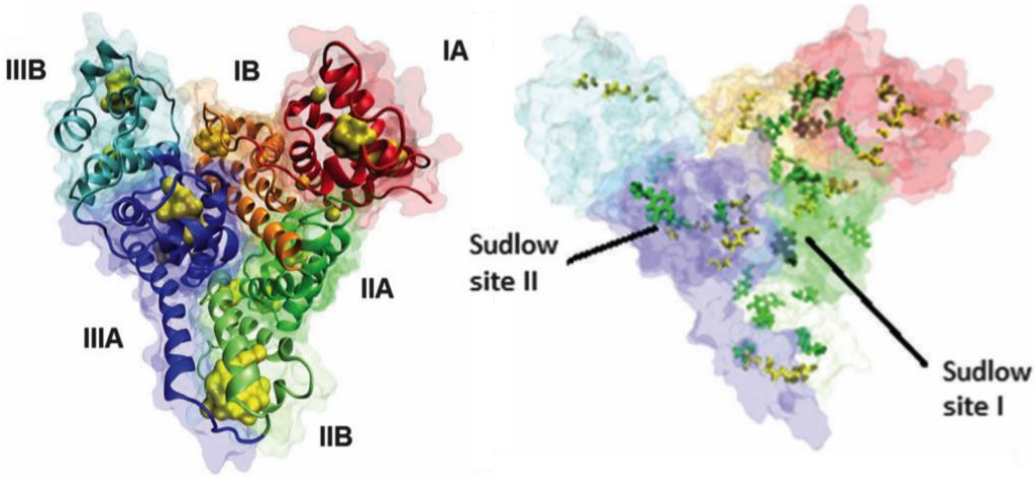

Figure 3.5: Molecular dynamics simulations showing AuNCs nucleated within the BSA protein after 600 ns. On the left two large nanoclusters can be observed in domain IA and IIB (as yellow globules), with smaller clusters dispersed throughout the protein. Gold atoms can be seen to be near when comparing the globule locations with the cysteine locations within BSA on the right (seen as yellow chains). Tyrosine residues (seen as green chains) can be seen within proximity to the cysteine residues. In both cases the protein surface is represented using a ghost model and coloured to indicate subdomains of the protein. IA – red, IB – orange, IIA - green, IIB – light green, IIIA – blue, III – light blue.

Previous studies have indicated that tyrosine may play a part in the one pot synthesis process by acting as a reducing agent for the gold salt used[51]; however only four tyrosine residues are accessible at the protein surface. Therefore, the areas at which gold atoms can interact with the protein surface before migrating to a cysteine residue may be limited to areas where the tyrosine residues can be accessed, and therefore the several different AuNC nucleation locations may not truly be representative of the real system. Of all the sites identified for possible AuNC nucleation, the major nucleation site in subdomain IIB which is within proximity of the Sudlow I binding site[191], is the most likely. The Sudlow I binding site is located within a hydrophobic pocket within domain IIA[192], as seen in Figure 3.5. The proximity between the Sudlow I binding site and major nucleation site of AuNCs is

interesting since this site has a high binding affinity for many molecules and contains a tyrosine molecule. This makes the Sudlow I binding site the most likely location for initial interaction between the gold salt and protein to take place within the real laboratory synthesis.

3.4.2 Fluorescence Spectroscopy Studies of BSA-AuNCs at different pH

To clarify where AuNCs were located within the BSA protein, BSA-AuNC fluorescence properties were studied under different pH conditions. To characterize the fluorescence emission from BSA-AuNCs in a detailed way, 3D excitation-emission graphs (3D EEM) were created. The full 3D EEMs for a concentrated sample of BSA-AuNCs (25,000 ppm) and a diluted sample of BSA-AuNCs (2,500 ppm) are shown in Figure 3.6.

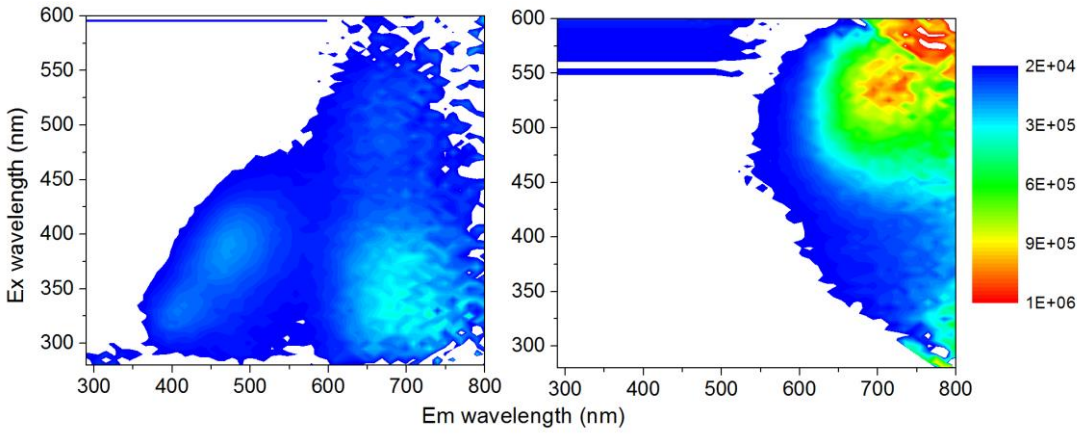

Figure 3.6: 3D EEMs of BSA-AuNCs at different concentrations. The left graph shows the full spectrum of BSA-AuNCs at a concentration of 2,500 ppm, while the graph to the right shows a more concentrated sample of BSA-AuNCs at 25,000 ppm. The uncoloured parts of the graphs indicate that the fluorescence was no higher than the background noise associated with the experimental apparatus.

In the diluted case, we can see that there are two distinct and separate fluorescence hotspots; one with an emission maximum between 400 - 500 nm which is attributed to the protein fluorescence (which arises from two tryptophan residues present in BSA) and one with an emission between 650 - 750 nm which is attributed to fluorescence from the AuNCs. Maximum AuNCs emission is seen at shorter excitation wavelengths when the sample is diluted and inner filtration effects are not present. Differences in the emission profiles for the diluted and undiluted BSA-AuNCs arise from inner filtration effects caused by the concentration of the sample. In the undiluted case, the emission is weak when excited with shorter wavelengths of light due to its inability to penetrate fully into the sample and excite the full population of fluorophores. The sample is effectively opaque at shorter wavelengths due to the high concentration of protein and AuNCs. At lower concentrations, inner filtration effects are not apparent and the full excitation spectrum is observed, revealing that UV light is a more effective excitation source for AuNCs than visible light. To understand why shorter wavelength light excites AuNCs the UV-Vis absorption spectrum was measured, as shown in Figure 3.7.

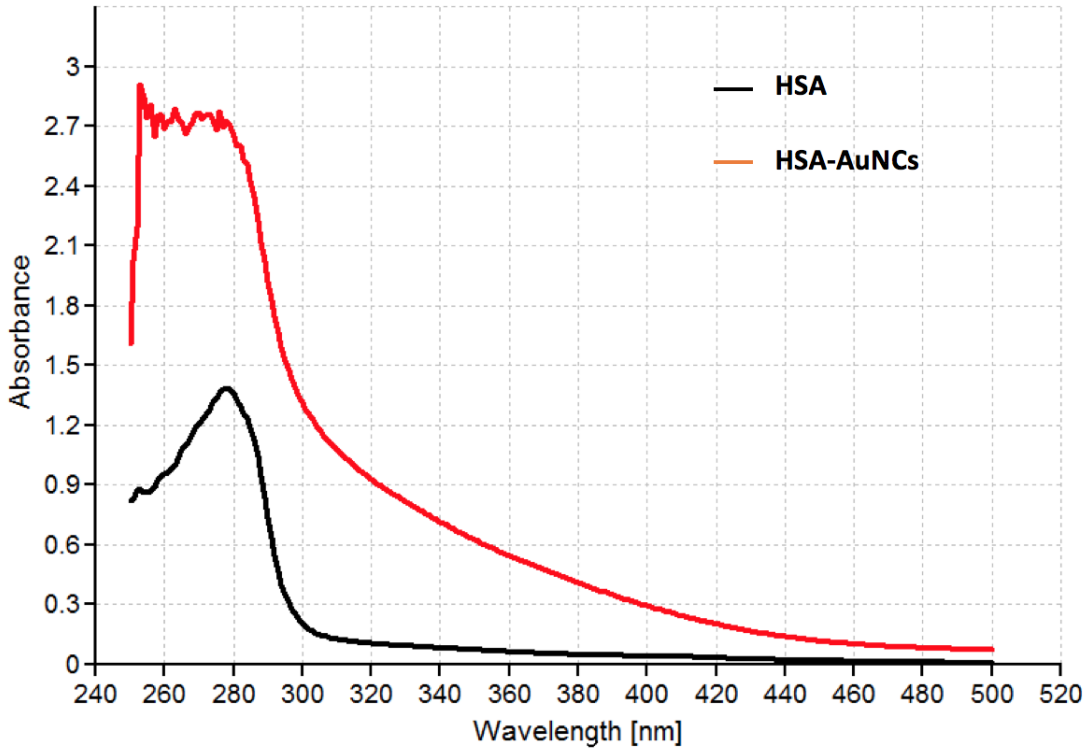

Figure 3.7: UV-Vis absorption spectra of HSA shown in black and HSA-AuNCs shown in red. The HSA-AuNCs spectrum between 260 – 290 nm is scattering light to such a high degree it is saturating the detection limit of the apparatus.

The absorption spectrum for BSA-AuNCs can be seen to be very broad, becoming weaker towards longer wavelengths, due to scattering. This accounts for the wide excitation spectrum, with the AuNCs becoming excited across a wide band from 280 - 500 nm.

Further characterization of the undiluted BSA-AuNCs (pH 10.5) was carried out using TCSPC to measure the fluorescence lifetime of the AuNCs. Exciting at 471 nm it was found that the fluorescence decay curve was bi-exponential in nature and thus had two fluorescence lifetimes associated with it, $\tau_1 = 940 \pm 80$ ns and $\tau_2 = 2310 \pm 30$ ns. The bi-exponential nature of the fluorescence decay is confirmed by the non-random residuals of the fitting used and the low χ^2 value of 1.13, as shown in Figure 3.8.

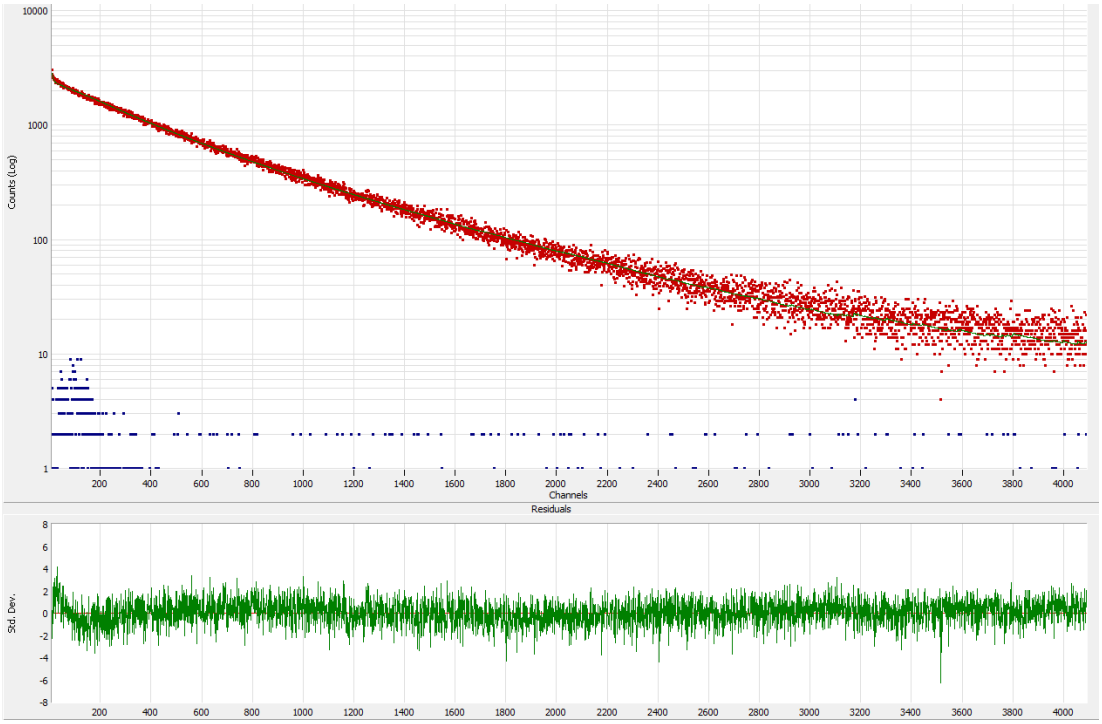

Figure 3.8: The top graph shows the fluorescence lifetime decay of BSA-AuNCs (excitation 482 nm, emission 670 nm). Red dots indicate the experimental data while green represents the fitted bi-exponential theoretical model describing the fluorescence kinetics. The lower graph represents the quality of fit between the theoretical function and experimental data. The residuals here can be seen to be randomly distributed and therefore indicate good agreement between theory and experimental data. (χ^2 = 1.13)

To locate the domain in which the AuNC is bound the BSA proteins tertiary structure was unfolded and modified by varying the pH. How BSA unfolds in a changing pH environment is well documented and thus it is well known which domains of the protein become solvent exposed at different pH. The fluorescence characteristics of the AuNC were tracked as the pH was altered and the proteins began to unfold. Initially 3D EEMs were measured of BSA-AuNCs in pH intervals of 2, as shown in Figure 3.9.

The fluorescence emission characteristics of BSA-AuNCs are highly affected by pH of the solvent. The BSA protein is in its natural state at pH 7.0 and this coincides with the brightest emission from the AuNCs and the weakest emission from the tryptophan fluorescence (except from the case where pH is 0.95). The low tryptophan emission coupled with the strong AuNC emission is a strong indicator for FRET taking place between the two fluorophores; this point will be explored in more detail later in this chapter. As the pH is lowered the protein begins to unfold, the separation between the AuNC and tryptophan increases, resulting in less energy being transferred to the AuNC from tryptophan. This results in tryptophan becoming brighter at pH 3.07 and pH 4.95 in comparison with pH 6.98. The reverse is true of the AuNCs which become quenched as the protein opens. It is also likely that solvent exposure of the AuNCs results in collisional quenching. At pH 0.95 the protein is fully unravelled which causes both the AuNC and tryptophan to be fully solvent exposed resulting in complete quenching of tryptophan fluorescence and near complete quenching of AuNC fluorescence. The weak fluorescence still displayed by the AuNCs may indicate that a small population of proteins remain partially folded. At pH of 8.95 and 11.11 the fluorescence of tryptophan increases while the AuNCs emission intensity drops. Serum albumin proteins do not undergo unfolding at higher pH, however, they are known to rearrange their surface structure. Hydrophobic residues bury themselves further within the protein itself which likely effects the separation distance between tryptophan and AuNCs resulting in the lower emission intensity and shortened fluorescence lifetime observations made at higher pH.

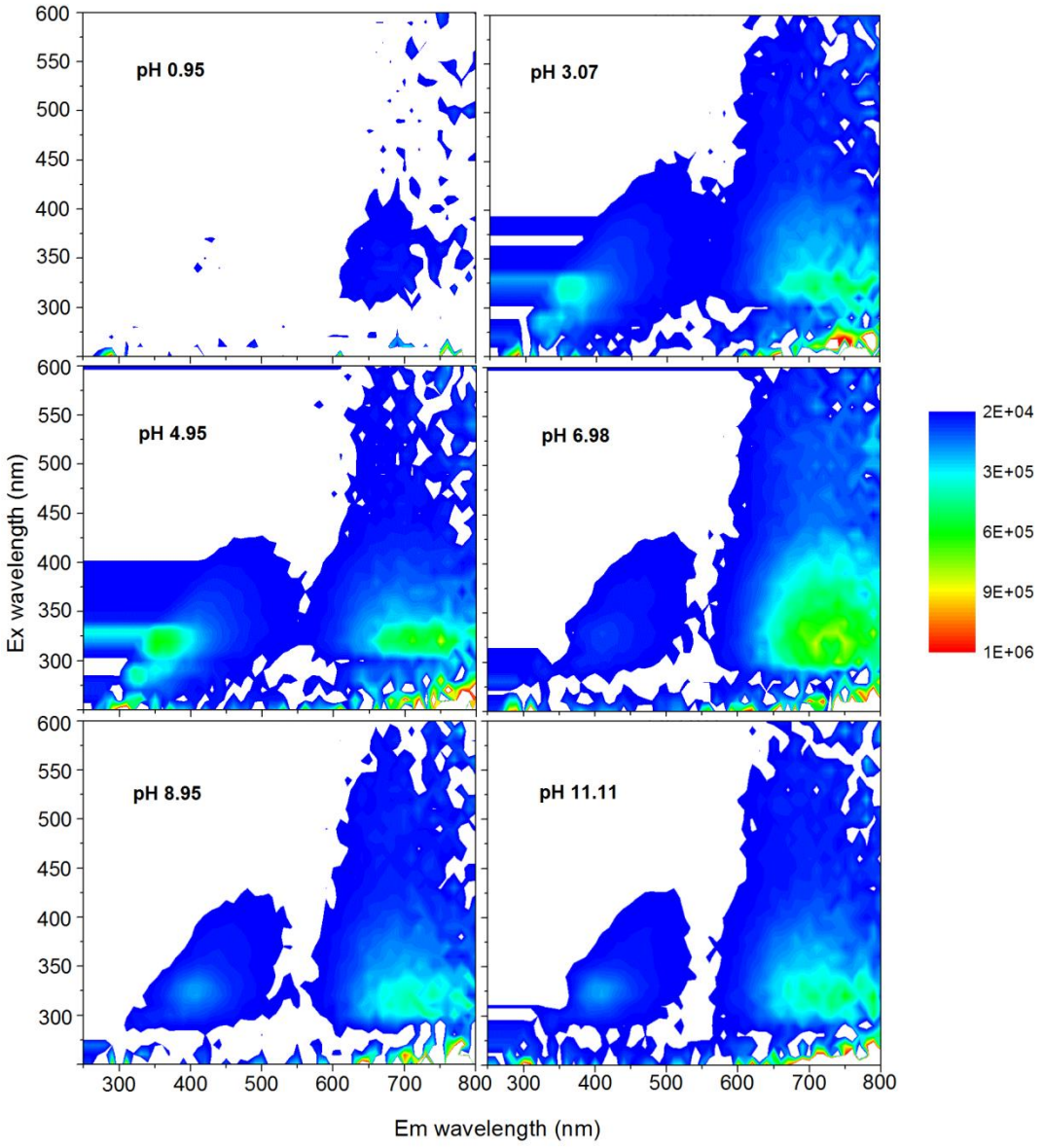

Figure 3.9: 3D EEMs of BSA-AuNCs at different pH. As pH lowers from 6.98, the fluorescence signal of BSA-AuNCs is quenched due to the unfolding of the protein and subsequent solvent exposure of the AuNCs. As pH increases the protein conformational change can be seen to quench the fluorescence of AuNCs to a lesser degree.

To better compare and quantify the fluorescence emission peak of AuNCs under different protein conformations 2D emission spectra were taken, exciting at 295 nm, as shown in Figure 3.10.

The fluorescence of AuNCs is strongest when the BSA protein is in the normal form. Upon increasing the pH to 12.0 the fluorescence emission at the peak decreases by ~60 %. As previously mentioned, when the BSA protein is in the aged form at high pH the tertiary structure remains broadly the same. However, solvent exposed alpha helices become buried under the protein surface. Decreasing AuNCs emission during this conformational change indicates that the AuNCs location is modified in some way and is most likely near the protein surface where the alpha helices are changing position. Lowering the pH to 1.0 resulted in a dramatic decrease in fluorescence emission from the AuNCs. This dramatic decrease coincides with the unfolding of domains I and II of the BSA protein at low pH and therefore it is most likely that the AuNCs are located within either of these domains. The fluorescence decrease is attributed to the domains becoming solvent exposed and the AuNC fluorescence undergoing collisional quenching, as previously mentioned. If the AuNC were located within domain III of the protein, we would not expect such a dramatic drop in fluorescence since it does not become globular and lose its shape at lower pH.

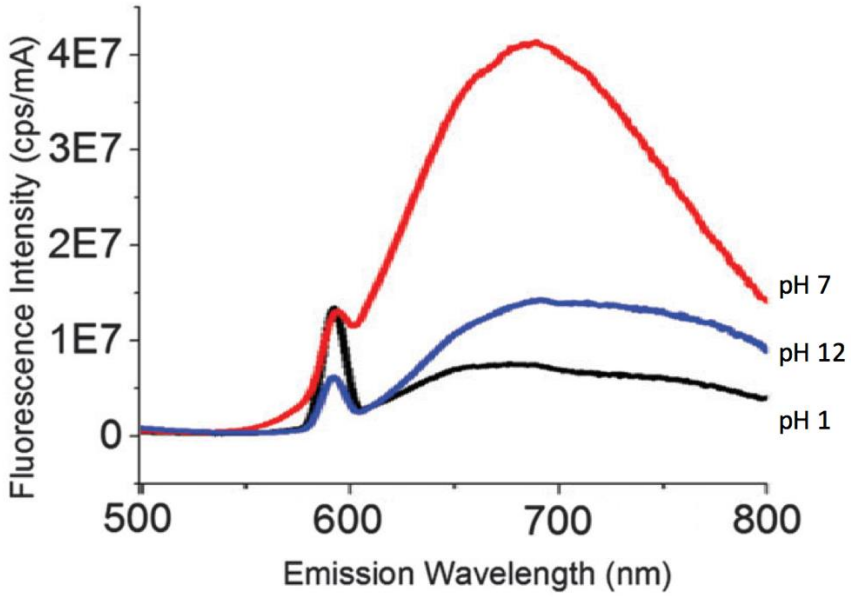

Figure 3.10: Fluorescence emission spectra of BSA-AuNCs at different pH (excited at 295 nm). pH 1 is indicated by black, pH 7 is indicated by red, pH 12 is indicated by blue. The small peak for each spectrum at 590 nm is a second harmonic generated by the excitation source.

Further experimentation on the fluorescence characteristics of BSA-AuNCs under different pH conditions were carried out. Decay associated spectra of the BSA-AuNCs were measured at pH 1.0, 7.0 and 12.0 as shown in Figure 3.11.

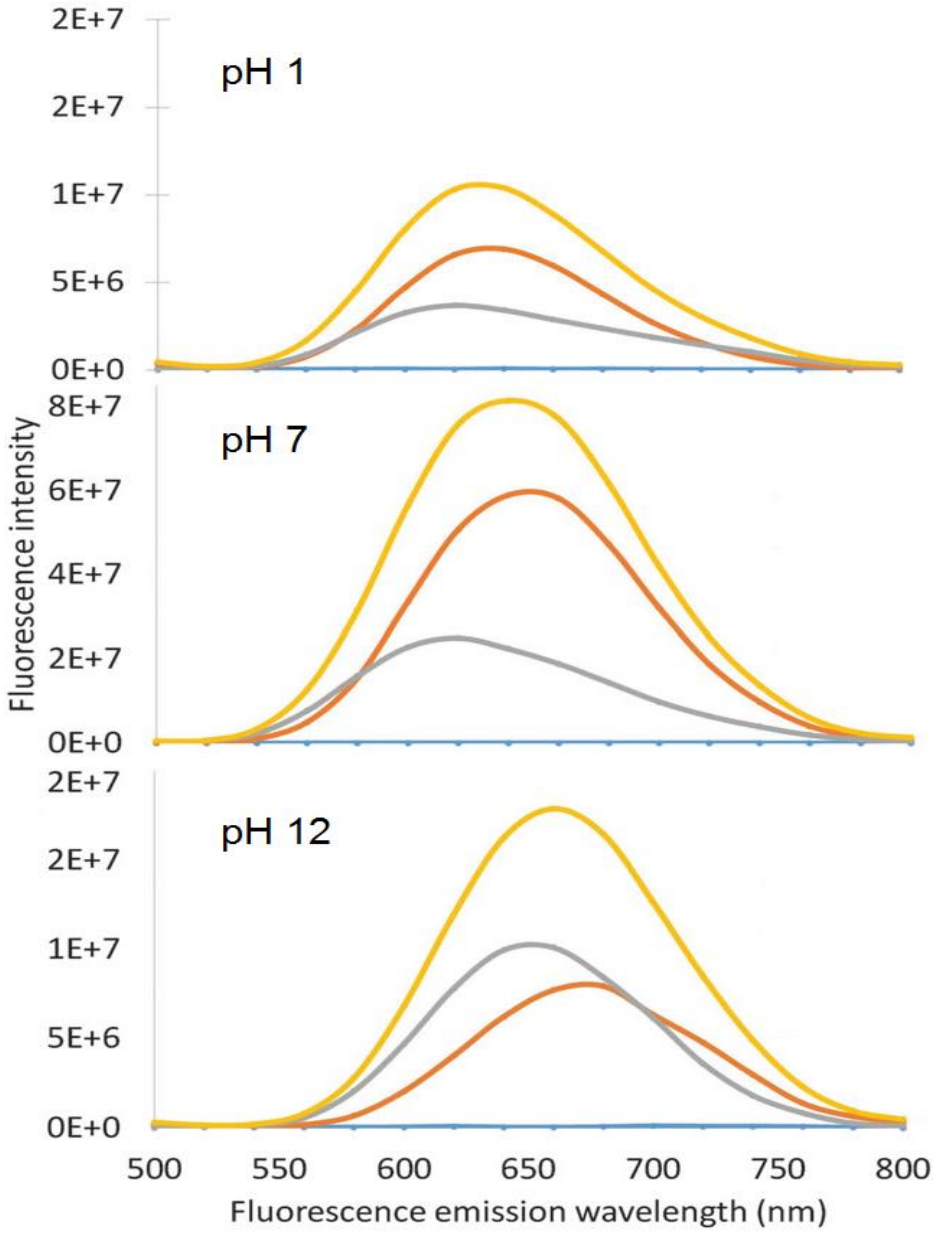

Figure 3.11: Decay associated spectra of BSA-AuNCs at varying pH (excitation 471 nm). Three exponential fitting gave varying lifetime values (all values are given in Table 3.12). τ_1 is shown in blue, τ_2 is shown in orange, τ_3 is shown in grey, the sum of all curves is shown in yellow.

A 3-exponential fitting revealed 2 long fluorescence lifetime components, in good agreement with the previous lifetime measurement of BSA-AuNCs (Figure 3.8) and a third short lifetime component which was due to scattering effects caused by the aggregation of the BSA (overall contribution to fluorescence intensity less than 1 % of total). The corresponding lifetime values are shown in Table 3.12.

pH of BSA-AuNCs	τ_1 (ns)	τ_2 (ns)	τ_3 (ns)	χ^2
1	220 ± 80	1940 ± 80	4460 ± 90	1.08
7	360 ± 20	2000 ± 20	4730 ± 40	1.37
12	190 ± 30	1170 ± 30	2400 ± 30	1.17

Table 3.12: Fluorescence Lifetimes and goodness of fit criteria associated with the decay associated spectra of Figure 3.11. Excitation 471 nm, Emission 670 nm

The long lifetimes observed at pH 7, τ_2 = 2000 ± 20 ns and τ_3 = 4730 ± 30 ns compare well with previously reported values[150]. At pH 12 there is a significant decrease in both τ_2 and τ_3 to 1170 ± 30 ns and 2400 ± 30 ns, respectively. The overall contribution of each lifetime to the total fluorescence also changes, with τ_3 becoming more prominent (see Figure 3.10). As previously stated at highly basic pH alpha helices exposed at the protein surface become buried within the protein. If the AuNC nucleation site is within proximity (*e.g.* the possible nucleation site discussed in either domain IIB or IA), then at high pH the hydrophobicity of the AuNC microenvironment could be altered, possibly making the AuNC more solvent exposed resulting in a decrease in fluorescence lifetimes. At pH 1 the fluorescence lifetimes of AuNCs were like the lifetimes found at pH 7, τ_2 = 1940 ± 80 ns and τ_3 = 4460 ± 90 ns. This similarity suggests that the fluorescence originated from a similar mechanism at both pH. As previously shown, it is possible that a few BSA-AuNCs remain unfolded at low pH and are still able to fluoresce without the fluorescence characteristics being altered by solvent exposure associated with the protein

unfolding. While the fluorescence lifetimes do not change between pH 1 and pH 7, the total intensity measured from the sum of both fluorescence lifetimes decreases by a factor of ~8 (see Figure 3.10's difference in intensity), comparing well with the decrease in fluorescence intensity seen in Figure 3.9.

The decrease of both longer fluorescence lifetimes along with the drop in total intensity observed during the lifetime measurement can be explained again by the unfolding of a large majority of the BSA-AuNCs molecules under strong acidic conditions, where fluorescence is quenched due to the breaking of sulphur-gold bonds and the exposure of AuNCs to the surrounding solvent. In conjunction with the well-known conformational changes of BSA under these conditions, these results again suggest a nucleation site of either domain IA or IIB.

3.4.3 Förster Resonance Energy Transfer (FRET) between tryptophan and AuNCs present in serum albumin encapsulated AuNCs

Here we studied the FRET interaction between tryptophan and AuNCs to further probe for the location of AuNCs within serum albumin proteins. To show that FRET takes place in BSA-AuNCs the emission from tryptophan in the presence and in the absence of AuNCs within BSA was measured. The concentration of protein in all cases was kept constant at 2,500 ppm and pH 7. The results are shown in Figure 3.13.

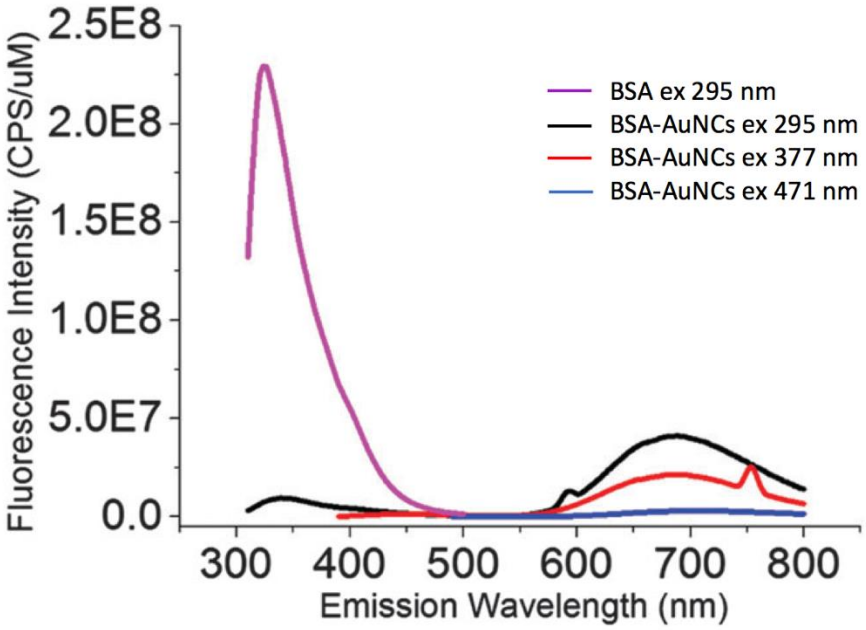

Figure 3.13: The fluorescence emission spectrum of BSA (excitation 295 nm) is shown in pink. Fluorescence emission spectra of BSA-AuNCs excited at different wavelengths are also shown. Blue indicates BSA-AuNCs excited at 471 nm, red indicates BSA-AuNCs excited at 377 nm and black indicates BSA-AuNCs excited at 295 nm. The fluorescence from tryptophan is completely quenched in the presence of AuNCs while AuNCs emission increases the shorter the excitation wavelength, indicating possible FRET.

It is evidently clear that the presence of AuNCs within the BSA protein causes tryptophan emission to be quenched. The fluorescence emission from BSA-AuNCs at 295 nm also suggests that the tryptophan present in BSA offers additional channels of excitation for the AuNCs rather than just exciting the fluorophore directly which is seen using a 471 nm excitation source. Other criteria must also be met if FRET is to be a plausible explanation for tryptophan emission becoming quenched while at the same time AuNC emission is enhanced. The spectral overlap between tryptophan emission and AuNC absorption must be enough that efficient energy transfer can take place. The spectral overlap for both fluorophores is shown in Figure 3.14 and can be seen that the donor emission and acceptor absorption spectra overlap and FRET is possible.

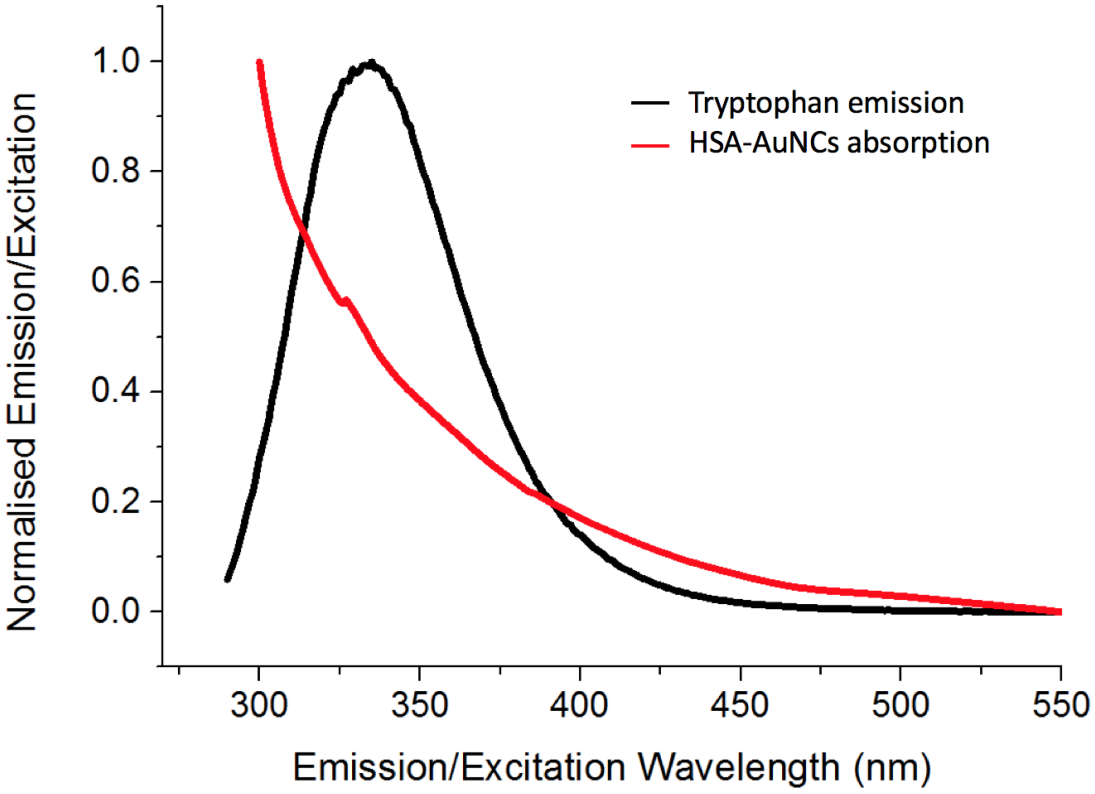

Figure 3.14: Spectral overlap between tryptophan emission indicated in black and HSA-AuNCs absorption, indicated in red.

To simplify any separation calculations made using FRET as a 'spectroscopic' ruler, HSA was used rather than BSA to encapsulate the AuNCs. This is due to the single tryptophan present in HSA, while there are two tryptophans present in BSA; both of which could have an influence on the energy transfer to the AuNCs. HSA also has a similar structure to BSA making it a possible substitute for the following work. Initially the Förster distance, $R_{0,}$ was calculated using Equation 2.8 and the spectral overlap from Figure 3.9. This yielded a R_0 value of 30.14 Å. To find the energy transfer efficiency, the fluorescence lifetimes of tryptophan in HSA were measured in the presence and absence of AuNCs.

Fitting the fluorescence lifetime decay with a 3-exponential model yielded 3 fluorescence lifetimes with an average lifetime of 4.33 ± 0.02 ns in the absence of AuNCs and an average lifetime of 2.33 ± 0.02 ns in the presence of AuNCs. The

need for a 3-exponential model arises from the 3 different rotamer forms of tryptophan found in nature, each with its own fluorescence lifetime[193]. The tryptophan-AuNC separation was then calculated using the R_0 and average lifetime values of tryptophan measured in conjunction with Equations 2.7 and 2.10, yielding a value of 29.74 Å.

To compare this separation to possible nucleation sites suggested in Section 3.4.1 and 3.4.2 a HSA model was downloaded from the protein databank (model iD: 4K2C)[189] and compared to the BSA model previously used for MD simulations using VMD software. The distance from the cysteine residues 316, 360, 361 and 369 (the cysteine residues located in the major binding site found in domain IIB) to the single tryptophan molecule were found to be 28.79 ± 3.23 Å, 27.29 ± 3.23 Å, 29.52 ± 3.23 Å and 30.90 ± 3.23 Å respectively, matching the distance calculated from the FRET calculations previously carried out. This group of cysteine could be a favourable nucleation site for gold since it is close to a tyrosine molecule on the protein surface and to the tyrosine molecule which makes up part of the Sudlow I binding site. The second possible major nucleation site located in domain IA was found to be too far from the tryptophan residue. Cysteine 75 and 91, which make up the IA nucleation site were found to be 35.60 ± 3.23 Å and 36.01 ± 3.23 Å, too large a separation in comparison to the FRET calculation value of 29.74 Å. For a detailed view of the separation between tryptophan and the two possible major AuNCs nucleation sites see Figure 3.15. From this study the most likely location for AuNC nucleation in serum albumin proteins is within domain IIB, surrounded by the four cysteine residues found at the base of the heart shape.

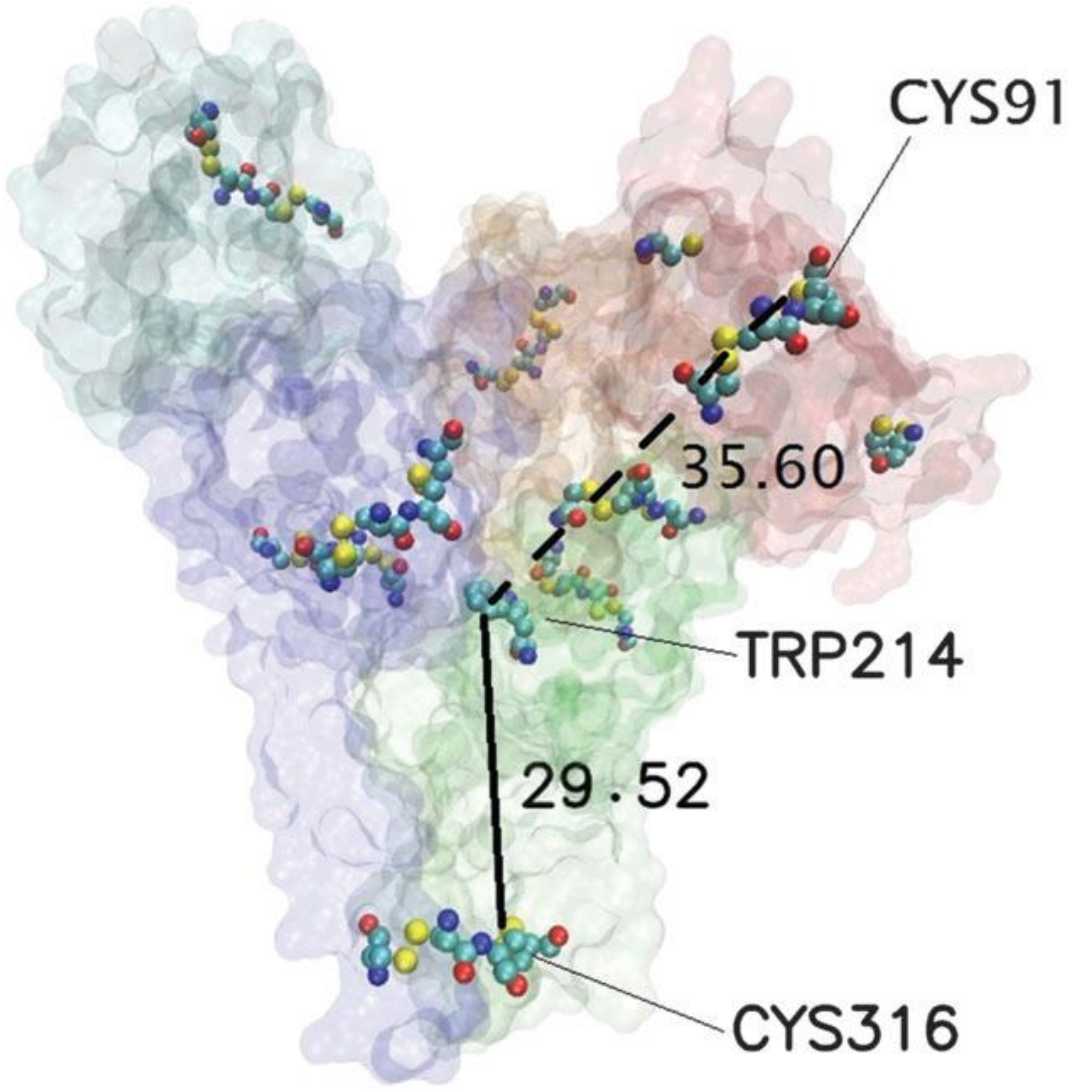

Figure 3.15: HSA protein model (4K2C). The separation between the tryptophan residue at position 214 and cysteine 316 in domain IIB was found to be 29.52 Å, indicated by the black solid line. The separation between cysteine 91 in domain IA and tryptophan was found to be 35.60 Å. The domain colouring scheme is consistent with other Figures previously shown.

This result also suggests that while there are 35 cysteine residues present with in the serum albumin proteins studied, only a small number of sulphur-gold bonds are created during synthesis and stabilization of the AuNC. In previous XPS studies carried out, a small number of Au(I) atoms were present on the surface of the AuNC core, ~17 % of the total gold atoms studied were in this Au(I) state while the rest

were in the Au(0) state[51]. If the AuNCs are indeed 25 atoms in size, this would indicate 4 Au atoms in the Au(I) state, agreeing with the result showing 4 cysteine in the nucleation location. This suggests a much smaller number of sulphur-gold bonds in comparison to thiolated AuNCs, *e.g.*, $Au_{22}SG_{18}$. Another study, carried out by Bao *et. al.* compared the fluorescence characteristics of AuNCs encapsulated within BSA (35 cysteine) and lysozyme (8 cysteine)[181]. They found that despite the large difference in total available sulphur to bond to, the fluorescence lifetimes of the AuNCs were similar. This again suggests that only a few cysteines are involved in the stabilization of AuNCs within proteins. Due to the complexity of protein encapsulated AuNCs, the current explanation of the fluorescence mechanism is based on atomically precise thiolated-AuNCs.

3.5 Conclusions

Molecular dynamics simulations were utilised in conjunction with Fluorescence based measurements techniques to unveil the position of AuNCs within serum albumin proteins. Simulations clearly show that the AuNCs have a strong affinity for nucleation within hydrophobic pockets of the protein which also contain cysteine residues which were previously shown to be vital to the formation of AuNCs within proteins. AuNCs were found to grow in several sites with cysteine; however only two larger clusters formed at two sites which accommodate the larger cluster size. Two large clusters greater than 12 atoms in size were found at potential binding sites in domain IA and IIB of the BSA protein. By altering the pH of BSA-AuNCs in solution experimentally, it was possible to study the changing fluorescence properties and correlate it with well-known conformational changes of BSA at pH. From these experiments, we could determine that the AuNC was not located within domain III of BSA. Finally Using FRET analysis, we could calculate the separation between a single tryptophan residue in HSA and the AuNC. The separation distance was found to be 29.74 Å. This separation was compared to the separation between the tryptophan and cysteine residues located in the two possible major binding sites using a HSA computer model in VMD. The separation between cysteine residue 316 located in the binding site in IIA and the single tryptophan was found to be 29.52 Å,

a near match to the FRET experimental separation. This work therefore shows the location of AuNCs within serum albumin proteins to be the large hydrophobic pocket located at the bottom of the proteins heart shape in domain IIB.

This result is significant as it reveals for the first time the precise location of an AuNC synthesized within serum albumin proteins. This opens the possibility of understanding the fluorescence mechanism of protein encapsulated AuNCs by studying the AuNC local environment. A better understanding of the local environment would naturally allow for more intelligent, focussed attempts at manipulating the fluorescence characteristics of protein encapsulated AuNCs. This will be important to any future endeavours to improve the fluorescence of serum albumin encapsulated AuNCs and utilise them as a fluorescent dye or probe in biomedical imaging and sensing. In the next chapter the possibility of using the nearby drug binding site as a means of manipulating the fluorescence characteristics of AuNCs encapsulated in HSA will be explored in the next Chapter.

4 Probing the Sudlow I Binding Site within HSA-AuNCs Using Warfarin

4.1 Abstract

In the previous chapter, it was shown that the location of AuNCs in HSA was a hydrophobic pocket at the bottom of the heart shape structure in domain IIB. While this location does not typically bind with other molecules it was close enough to the major drug binding site Sudlow I to merit further investigation. It is possible the function of the protein may be altered due to the proximity of the AuNC to the drug binding site. If HSA-AuNCs are to be utilized as functional fluorescent biomarkers in biological imaging, either *in vivo* or *in vitro*; it is important to fully understand the exact effect the presence of AuNCs have on protein function. Natural HSA acts as the main drug carrying protein within the blood stream, carrying a multitude of molecules in the two major drug binding sites (Sudlow I and II). To probe any changes to the binding affinity of the drug binding sites before and after the synthesis and nucleation of AuNCs, the fluorescent drug molecule, warfarin, was employed due to easily observed and well documented changes to its fluorescence characteristics upon binding to HSA.

Experimental spectroscopic studies were carried out which showed that warfarin is unable to bind naturally to HSA-AuNCs and that the presence of AuNCs stops the Sudlow I site from being functional. It was observed that AuNCs could not form using HSA with warfarin bound as a scaffold, suggesting that the Sudlow I site plays a critical role in the reduction of gold salt during synthesis. These discoveries are critical in predicting changes to natural protein behaviour in HSA-AuNCs and fully understanding the synthesis method, allowing for further optimization and improvements.

4.2 Introduction

Understanding how the presence of AuNCs within proteins affects their natural functionality is vital to the utilisation of protein encapsulated AuNCs as an *in vivo* probe or as a method of observing cellular activity *in vitro* imaging and sensing. HSA acts as a major transport molecule within the human body carrying an assortment of fatty acids, heavy ions and drug molecules. If HSA-AuNCs are to be used *in vivo* to aid the medical treatment of a patient, then any effect the introduction of HSA-AuNCs can have on the body must be known.

The major drug carrying sites of HSA are well documented[192,194,195]. The two major drug binding sites are referred to as Sudlow site I and Sudlow site II. Sudlow Site I, which is the site of interest to this chapter, consists of a pocket formed in the subdomain IIA with an opening to the solvent environment at the top of the heart shaped structure, and is commonly known to selectively bind with the drug warfarin[196]. Within the binding site itself are two sub-chambers which can accommodate different parts of the warfarin molecule. The interaction between binding site and warfarin is dominated by hydrophobic interactions; however, there are also many electrostatic contacts within the pocket that take part in binding also. The benzyl ring of warfarin binds in one of the previously mentioned sub-chambers which contacts the residues PHE211, TRP214, LEU219 and LEU238. The side chain of the tryptophan residue makes direct contact with the benzyl ring and has been shown to be critical to the binding affinity of warfarin to HSA[197]. It must be stressed however a wide number of drugs stereospecifically bind at Sudlow site I, all with different affinities due to the presence of other sub pockets within the Sudlow I binding site which accommodates different drug molecules[191].

Warfarin is a commonly used anticoagulant drug (also known by the brand name Coumadin or Jantoven) which is used to prevent blood clots in veins or arteries. It can reduce the risk of strokes or heart attacks in patients; however, it can be equally dangerous if administered in the wrong dosage or in conjunction with other drugs. Warfarin was chosen as a probe for the Sudlow I binding site due to its fluorescent nature and the changes to its fluorescence characteristics undergo upon binding to the HSA protein. Other molecules such as 4-hydroxycoumrin have been suggested as

alternatives to probe binding affinity to HSA; however, they use Nuclear Magnetic Resonance spectroscopy (NMR) and High-Performance Affinity Chromatography (HPAC) rather than fluorescence based spectroscopy[198]. Warfarin has an absorption maximum of 320 nm and an emission maximum of 390 nm. Free in solution, warfarin has weak fluorescence intensity due to quick, non-radiative losses of energy to the surrounding environment. Due to these loses to the surrounding environment fluorescence lifetimes of warfarin are very short, typically less than 0.1 ns[199]. Upon binding with HSA, the fluorescence intensity of the warfarin emission increases by a factor of around 10 times. This increase depends on the initial solvent micro environment of the warfarin molecule[200]. The fluorescence lifetime, because of the warfarin molecule being stabilised within the Sudlow I binding site, becomes longer, between 0.5 - 1.5 ns, depending on the solvent environment[201]. If these changes to fluorescence characteristics are observed upon mixing HSA with warfarin, then it is clear from the fluorescence information alone if the warfarin has bound to the Sudlow I binding site.

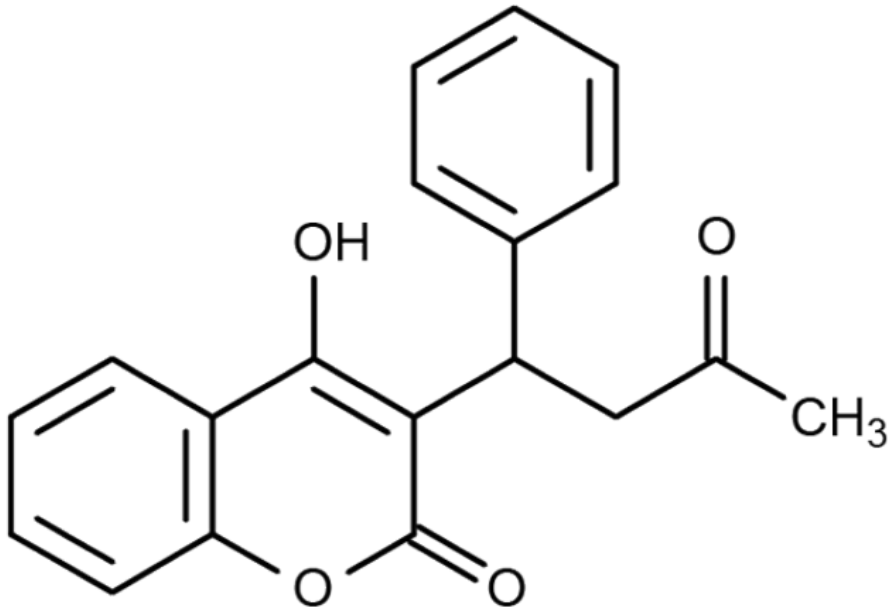

Figure 4.1: Chemical structure of warfarin molecule.

Changes to the protein function of serum albumin based protein encapsulated AuNCs is poorly documented. However, the function of lysozyme has been partly studied upon the synthesis of AuNCs within the protein scaffold. Liu *et. al.* developed a one pot synthesis method for lysozyme encapsulated AuNCs, like Xie's method, which allowed for the lysozyme molecule to retain its specific recognition ability the Escherichia coli bacteria (*E. coli*). It was found that upon Lysozyme binding to the bacteria surface the AuNCs fluorescence was enhanced, offering a possible real-time detection method for bacteria[202]. Therefore, from this study it is at least known that protein functionality is not always retarded by the presence of AuNCs.

From the previous chapter, we found the location of the AuNC within HSA to be near the Sudlow I binding site. We also observed that a tyrosine residue, which is needed in the reduction of $HAuCl_4$ also exists within the Sudlow I site raising questions as to whether the entrance to this binding pocket plays a role in the formation of AuNCs within serum albumin type proteins. Herein a valuable insight into how protein function can change upon the synthesis of AuNCs and new information towards better understanding the synthesis steps of protein encapsulated AuNCs in serum albumin type proteins are presented.

4.3 Experimental

4.3.1 Sample Preparation

HSA-AuNCs were prepared in the same manner as the previous Chapter (see **3.3.1 Sample Preparation)**. Warfarin was purchased from Sigma Aldrich and diluted using PBS buffer at an ionic strength of 0.1 M. PBS buffer solution was prepared via PBS buffer tablets also sourced from Sigma Aldrich.

4.3.2 Fluorescence Measurement and Data Analysis

Fluorescence emission spectra were acquired using a Horiba Fluorolog 3. The resolution of all emission spectra measured was 1 nm. All time resolved fluorescence lifetime measurements were performed on an IBH Fluorocube fluorescence lifetime system equipped with an emission monochromator, utilising the TCSPC technique. An LED based light source with an emission maximum of 303 nm, operating at a repetition rate of 1 MHz was used for all fluorescence lifetime measurements. A TAC range of 100 ns was used throughout. DAS6 software, as previously discussed was used to find the lifetimes associated with the fluorescence lifetime decays measured.

4.4 Results and Discussion

The fluorescence characteristics of warfarin in the presence and absence of HSA were first studied to understand the basic behaviour of the warfarin molecule. The adsorption of warfarin bound and unbound to HSA can be seen in Figure 4.2.

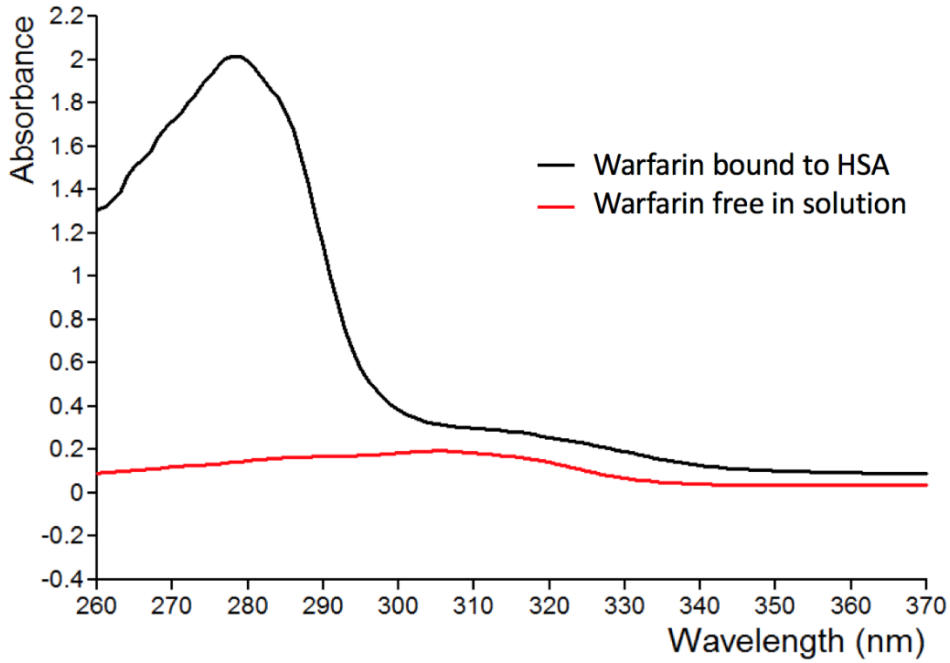

Figure 4.2: Absorption Spectra of warfarin free in solution, shown in red and warfarin bound to HSA, shown in black. The large peak at 280 nm is absorption due to HSA while the smaller peak at 310 – 320 nm is attributed to warfarin absorption. The absorption of warfarin is seen to increase and red-shift upon binding to HSA.

The absorption spectra profiles of warfarin in both cases match previously reported spectra in the literature[203].

The fluorescence emission spectrum of warfarin (warfarin concentration of 40 μM) was then observed in the presence and absence of HSA (HSA concentration of 40 μM), shown in Figure 4.3.

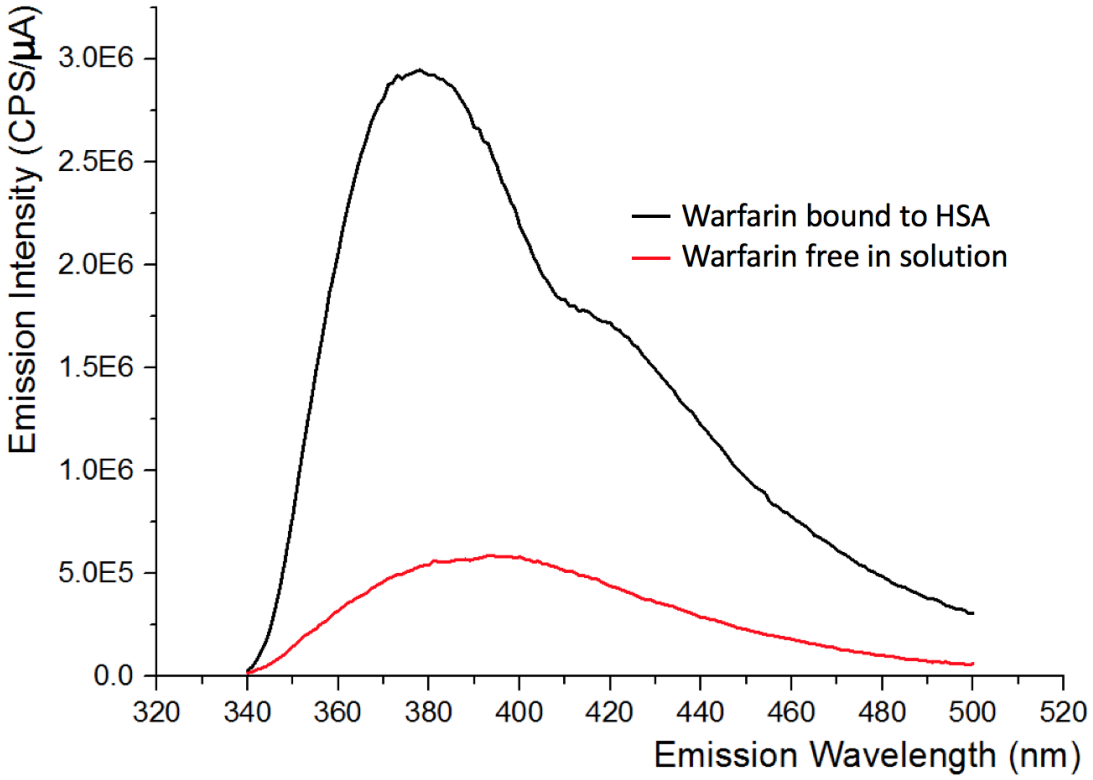

Figure 4.3: Emission spectra of warfarin bound to HSA, shown in black and warfarin free in solution, shown in red. The emission intensity of warfarin is seen to increase dramatically and blue-shift upon binding to HSA.

The increase in emission intensity and blue-shift of the emission peak of warfarin upon binding to HSA is a characteristic observation when studying the interaction between the protein and drug molecules[204]. The rise in fluorescence intensity stems from the added stability the warfarin molecule gains upon binding to HSA. This stability reduces the amount of energy lost non-radiatively by the warfarin molecule to the surrounding solvent environment.

The warfarin fluorescence lifetimes were also studied using the TCSPC technique in the absence and presence of HSA at the same concentrations as used in the previous experiment.

Sample	Warfarin	HSA-Warfarin
τ_1	0.12 ± 0.01	0.34 ± 0.02
τ_2	-	1.75 ± 0.06
τ_3	-	6.63 ± 0.15
χ^2	1.37	1.30

Table 4.4: Fluorescence lifetimes of warfarin free in solution and bound to HSA. Warfarin fluorescence lifetimes are seen to increase when bound to HSA due to the stability the protein gives to the molecule; resulting in less energy being dissipated in a non-radiative manner to the surrounding solvent.

Again, due to the fact the HSA protein lowers the amount of energy lost from the warfarin due to non-radiative mechanisms, such as collisional quenching from water and oxygen molecules in the solvent, the average lifetime the molecule stays in the excited state is seen to increase more than ten-fold on average. This again agrees with previously observed characteristics in the literature for warfarin[201,205].

Due to the multiple sources of fluorescence within sample solutions containing all of HSA, HSA-AuNCs and warfarin, it is important to this chapter that the fluorescence emission spectrum for each source is shown. The normalised emission spectra for warfarin (free in solution and bound to HSA), HSA emission due to the single tryptophan present and the emission of HSA-AuNCs is shown in Figure 4.5.

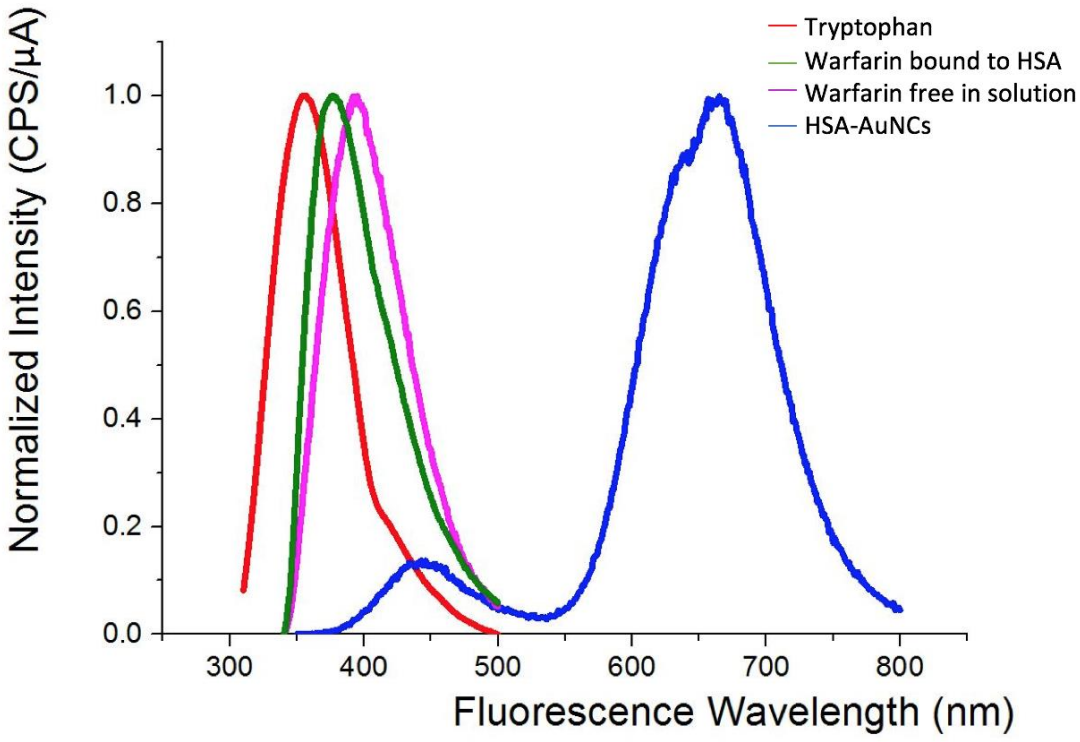

Figure 4.5: Normalised Fluorescence emission spectra of warfarin free in solution is shown in pink (emission peak at 393 nm), warfarin bound to HSA shown in green (emission peak at 370 nm), tryptophan emission is shown in red (emission peak at 340 nm) and HSA-AuNCs is shown in blue (emission peak seen at 440 nm is due to oxidised tryptophan emission while the peak seen at 670 nm originates from the AuNC). All samples were excited at 290 nm.

It is important to observe the broad, more complex emission from HSA-AuNCs due to the overlapping nature of the small emission shoulder at 440 nm. This overlap in fluorescence between HSA-AuNCs and warfarin must be considered when trying to observe any changes to warfarin fluorescence intensity upon mixing the two molecules. The overlap between the HSA and warfarin emission spectra is of vital importance to understanding the following observations presented in this chapter.

The binding affinity of warfarin to HSA and HSA-AuNCs was compared by introducing warfarin to both solutions in the same manner and comparing the changes to the fluorescence emission. The concentration of HSA and HSA-AuNCs were both kept constant at 40 µM while the concentration of warfarin was increased in 2.5 µM steps from 0-15 µM. These results were then compared to the spectra of warfarin in only buffer solution. The peak changes to warfarin's peak emission intensity are shown in Figure 4.6.

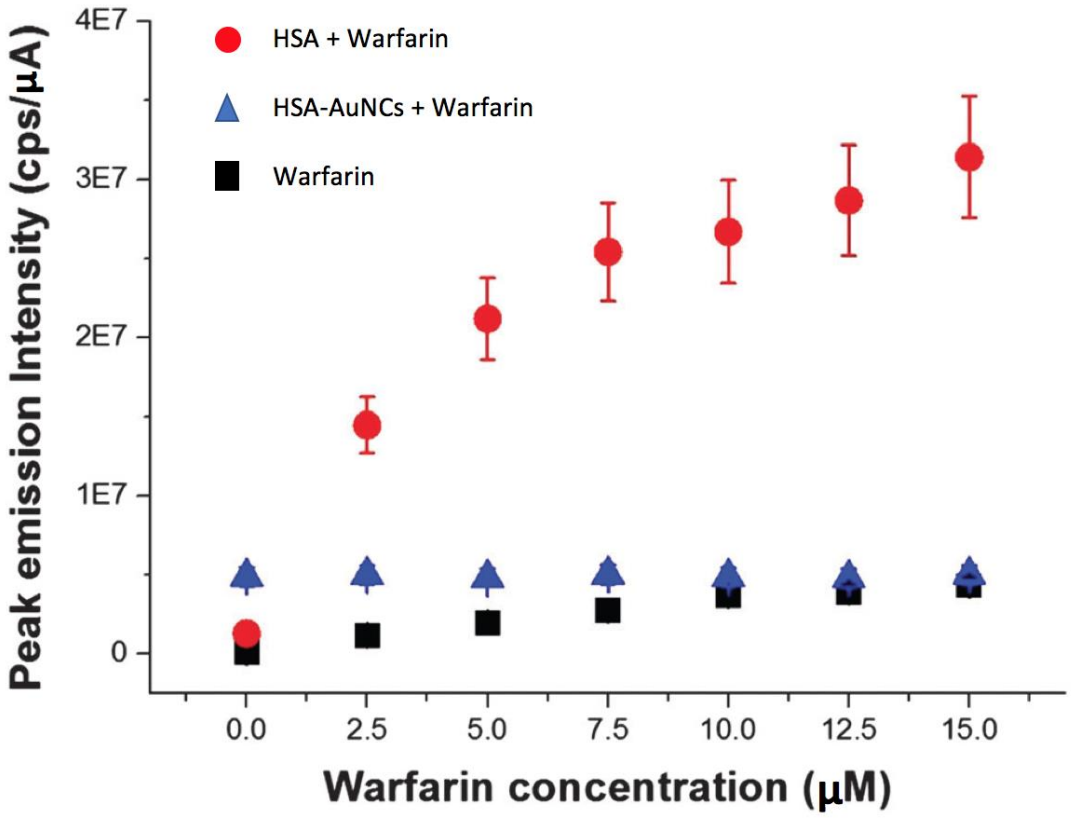

Figure 4.6: Peak fluorescence intensity of warfarin increasing in concentration under different conditions (excitation 320 nm). Warfarin in buffer solution is shown in black, warfarin in solution with HSA-AuNCs (40 µM) is shown in blue and warfarin in solution with HSA (40 µM) is shown in red.

For consistency, all samples were excited at 320 nm rather than the absorption maximum for each. As expected, increasing the warfarin concentration in buffer solution resulted in a linear increase in peak fluorescence emission. This shows that between concentrations of 0-15 μM warfarin does not undergo collisional quenching or inner filtration through interactions between the individual molecules, since the peak emission distribution would not be linear in nature as the concentration increases. The peak emission of warfarin does not change in the presence of HSA-AuNCs. The fluorescence measured can be attributed to the small emission shoulder of HSA-AuNCs (seen previously in Figure 4.5). There is no increase in peak fluorescence as warfarin is added; suggesting that warfarin fluorescence is quenched by either the presence of AuNCs within the HSA molecule or left over products from the AuNCs synthesis (this is unlikely due to the cleaning procedures carried out on the sample post synthesis). Finally, the addition of warfarin to HSA resulted in the characteristic large peak fluorescence increase from warfarin when bound to HSA. As more warfarin is added to the HSA we can see the increase in peak fluorescence emission is greater than that for warfarin alone in buffer. This observation points to warfarin binding to free HSA. The initial fluorescence peak measured for warfarin in solution with HSA is non–zero due to intrinsic fluorescence from the HSA molecule before any warfarin has been added to solution.

The fluorescence peak position for the above experiments were also monitored and displayed in Figure 4.7.

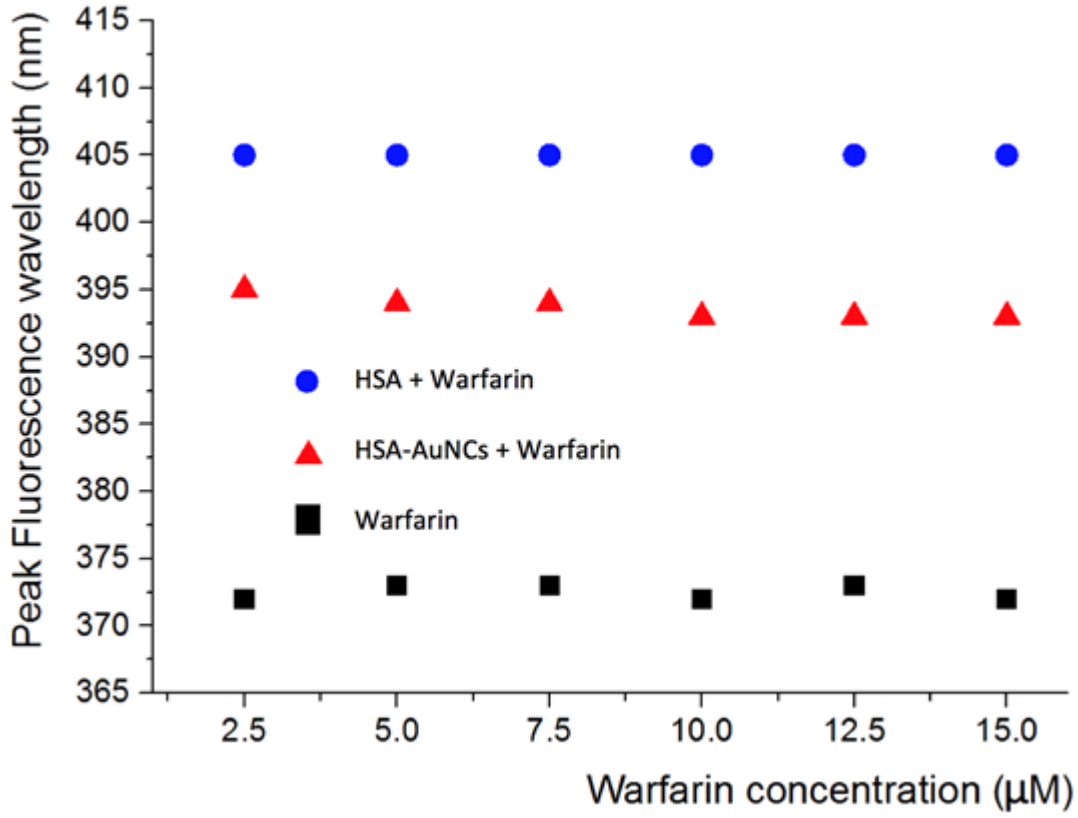

Figure 4.7: Peak emission wavelength of warfarin (excited at 320 nm), in buffer solution shown in black, in solution with HSA shown in red and in solution with HSA-AuNCs shown in blue. The emission of warfarin is seen to redshift upon binding to HSA while the red shift in emission from warfarin in solution with HSA-AuNCs is attributed to direct emission from HSA-AuNCs, not warfarin.

From changes in peak emission wavelength we can see that warfarin in solution with HSA are binding to one another since the emission maximum of warfarin at 373 nm is red-shifted to 394 nm in the presence of HSA. In the case of HSA-AuNCs the peak emission wavelength is too high to be contributed to warfarin emission and is instead due to the direct fluorescence of HSA-AuNCs. This along with the data in Figure 4.6 suggests that warfarin does not bind to HSA in the presence of AuNCs.

As previously shown, the fluorescence lifetime of warfarin can also be a powerful tool in determining the interaction of the molecule with HSA. To further probe the interactions between warfarin and HSA-AuNCs the fluorescence lifetime of warfarin

in the presence of HSA-AuNCs was studied and compared to previously shown fluorescence lifetime data using the TCSPC technique. The TCSPC measurements were carried out under the same conditions used previously for the intensity based studies. The fluorescence intensity decay curves were fitted using a multi-exponential model, analysing the goodness of fit using the least-squares method. The fitting results for warfarin fluorescence lifetimes in the presence of HSA-AuNCs along with the previous results from Table 4.4 for reference are displayed in Table 4.7.

Sample	Warfarin	HSA +Warfarin	HSA-AuNCs + War
τ_1	0.12 ± 0.01	0.34 ± 0.02	0.16 ± 0.02
τ_2	-	1.75 ± 0.06	1.86 ± 0.31
τ_3	-	6.63 ± 0.15	4.98 ± 0.28
b_1	0.026 ± 0.001	0.054 ± 0.001	0.169 ± 0.001
b_2	-	0.036 ± 0.001	0.094 ± 0.001
b_3	-	0.002 ± 0.001	0.030 ± 0.001
α_1	1.00	0.58	0.93
α_2	-	0.39	0.05
α_3	-	0.03	0.02
χ^2	1.37	1.30	1.30

Table 4.7: Results of exponential fitting to warfarin fluorescence decay curves in the presence of HSA and HSA-AuNCs and alone in buffer solution. Warfarin alone in solution was found to be single-exponential in nature while in the presence of HSA and HSA-AuNCs was found to be 3 exponential. All samples were excited at 303 nm using a Nano LED and TAC range of 100 ns, emission was measured at the respective peak emission wavelength for the sample.

Warfarin alone in solution has a very short fluorescence lifetime of 0.12 ± 0.01 ns, explained by a rapid de-excitation through the loss of vibrational and rotational energy to the surrounding solvent. Upon binding to HSA in solution we observe a more complex decay with three longer lifetimes present; τ_1 = 0.34 ± 0.02 ns, τ_2 = 1.75 ± 0.06 ns and τ_3 = 6.63 ± 0.15 ns. The longer lifetimes of τ_1 and τ_2 can be explained by the stability that the warfarin gains as a result of binding to HSA. The longer lifetime of τ_3 is more consistent with the fluorescence lifetime associated with HSA. The relative intensity b_3 is much weaker than the other lifetimes suggesting that tryptophan present in HSA is weakly fluorescing in the background. Interestingly the fluorescence lifetimes of warfarin in solution with HSA-AuNCs are different. The decay is again more complex, with a three-exponential fitting best describing the kinetics. Lifetime values of τ_1 = 0.16 ± 0.02 ns, τ_2 = 1.86 ± 0.31 ns and τ_3 = 4.98 ± 0.28 ns were calculated from the fitting analysis. Lifetime τ_1 compares well with the lifetime value for warfarin free in solution and its corresponding alpha value α_1 = 0.93, showing that 93 % of the fluorescence lifetimes measured originated τ_1. This result suggests that most warfarin molecules do not bind to HSA when AuNCs are present in the HSA protein. The existence of τ_2 is possibly due to warfarin binding to free HSA which has no AuNCs formed inside. The alpha value α_2 is very small at 0.05 suggesting only a very small fraction of HSA remains free without AuNCs inside. The existence of the longer fluorescence lifetime τ_3 can again be assigned to HSA fluorescence as with free HSA with warfarin in solution.

To show that most warfarin molecules remain unbound in solution with HSA-AuNCs additional free native HSA was added to the solution and changes to the fluorescence emission intensity and peak wavelength were tracked. Any large increases in warfarin fluorescence and a peak emission red shift can be attributed to free warfarin binding to the newly added free native HSA. The maximum fluorescence intensity of warfarin was seen to dramatically increase upon adding HSA to the HSA-AuNCs + warfarin solution, as shown in Figure 4.8.

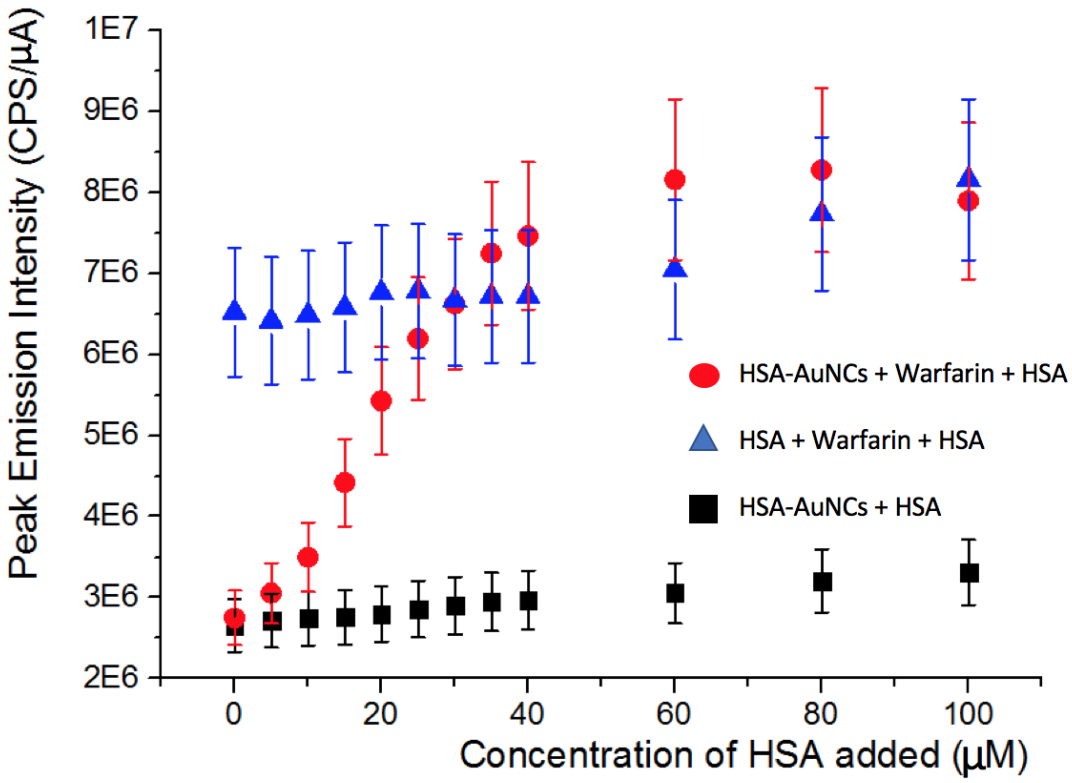

Figure 4.8: Fluorescence intensity of warfarin upon adding additional free HSA to a solution of HSA-AuNCs (40 µM) + warfarin (40 µM) shown in red, additional free HSA to a solution of HSA (40 µM) + warfarin (40 µM) shown in blue and additional free HSA to a solution of HSA-AuNCs (40 µM) shown in black. Upon adding free HSA to HSA-AuNCs & warfarin it was observed that the maximum emission intensity increased dramatically indicating free warfarin was binding to the added HSA.

To rule out the influence of intrinsic fluorescence from HSA, control tests were carried out by adding further amounts of HSA to HSA-AuNCs (without warfarin) and to HSA with warfarin already attached. In both cases the increase in fluorescence intensity can be seen to be small and the overall increase with respect to the added concentration of HSA is equal. This shows that intrinsic fluorescence from HSA cannot account for such a dramatic increase in fluorescence when HSA is added to HSA-AuNCs + warfarin in solution. It can also be seen that once 40 µM of HSA has

been added to HSA-AuNCs + warfarin the increase in peak fluorescence intensity levels off.

The peak fluorescence wavelength for the above experiment was also observed and is displayed in Figure 4.9.

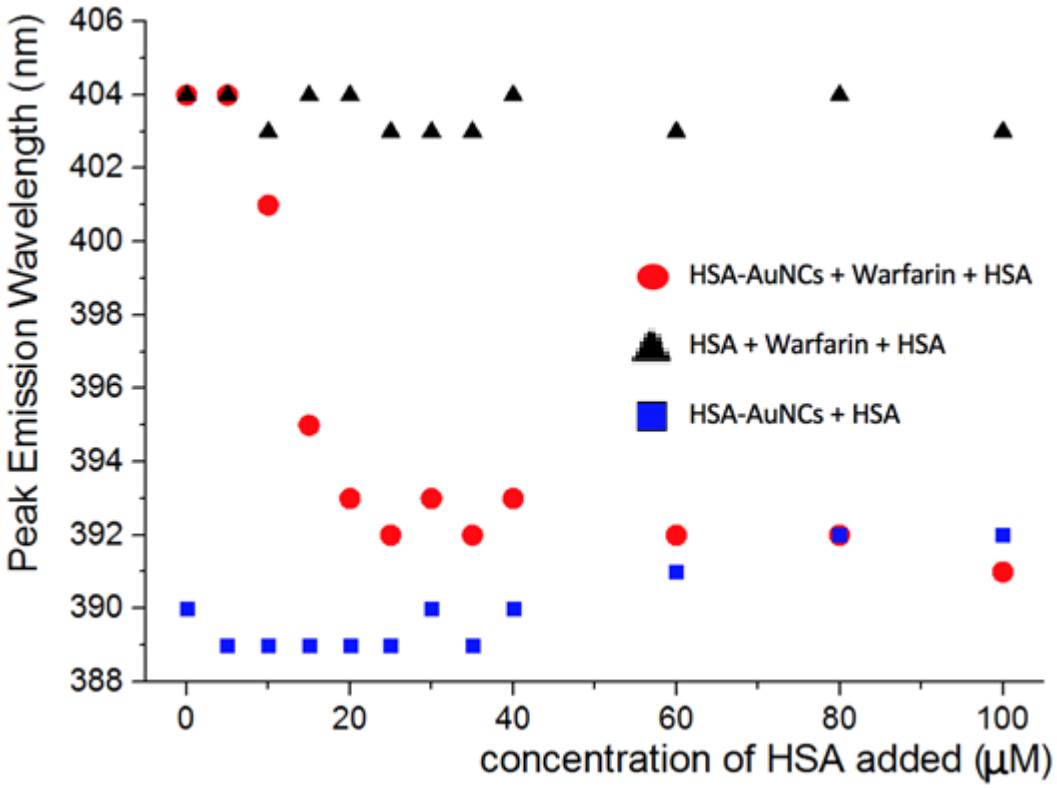

Figure 4.9: Peak emission wavelength of warfarin upon adding additional free HSA to a solution of HSA-AuNCs (40 µM) + warfarin (40 µM) shown in red, additional free HSA to a solution of HSA (40 µM) + warfarin (40 µM) shown in blue and additional free HSA to a solution of HSA-AuNCs (40 µM) shown in black. Upon adding free HSA to HSA-AuNCs & warfarin it was observed that the peak emission maximum of warfarin shifted to 392 nm indicating that it had bound with the free HSA added.

The peak emission wavelength of warfarin in solution with HSA-AuNCs shifts from the same peak wavelength as HSA-AuNCs + HSA to the same peak wavelength as warfarin bound to HSA. This is another clear indication that there is free warfarin in solution with HSA-AuNCs and the addition of HSA results in the free warfarin binding to the free protein.

In summary the results from Figure 4.8 and Figure 4.9 suggest that: firstly, in the case of HSA + warfarin, most warfarin is bound to HSA and the small increases in peak fluorescence intensity is due to intrinsic HSA emission; secondly, the large fluorescence intensity increase when adding additional HSA to HSA-AuNCs + warfarin is not due to intrinsic HSA emission, but the binding of free warfarin to newly added HSA; thirdly, the final emission intensity of HSA + warfarin and HSA-AuNCs + warfarin + HSA are the same above 40 μM concentration levels of added HSA suggesting all previously unbound warfarin in the HSA-AuNCs solution was bound to the free HSA. These findings confirm that warfarin in a solution of HSA-AuNCs is free and unbound and the previously measured low fluorescence intensity of warfarin in solution with HSA-AuNCs was due to a lack of warfarin binding rather than quenching processes or alterations to the fluorescence nature of warfarin. The existence of AuNCs in HSA affects the binding of warfarin to protein. This may be due to the nucleation site of AuNCs being near the warfarin binding site.

To test this idea that the proximity between the AuNC nucleation site and warfarin binding site affected the binding of warfarin to HSA-AuNCs we attempted to synthesise AuNCs within HSA with warfarin pre-bound. The formation of AuNCs within HSA was monitored by observing the fluorescence emission from AuNCs during the synthesis period. The changes to emission spectra during the AuNCs growth period can be seen in Figure 4.10.

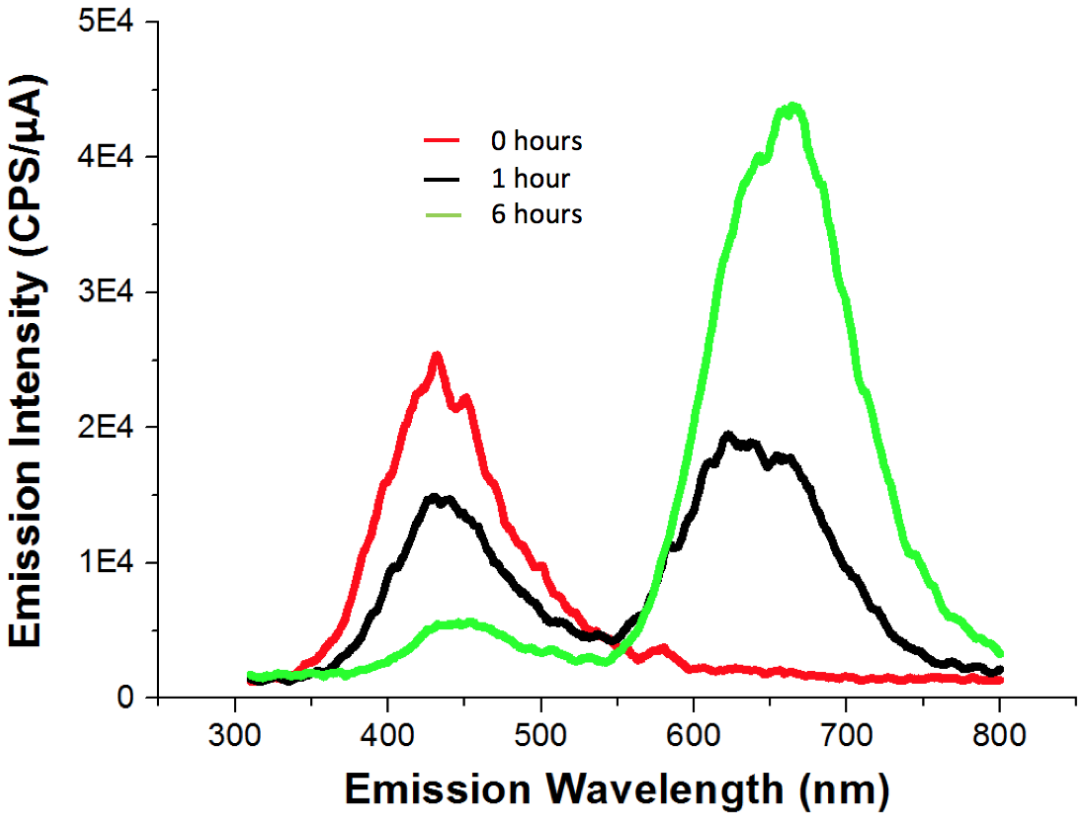

Figure 4.10: Fluorescence emission spectra of HSA-AuNCs during synthesis. At 0 hrs, shown in red, a peak at 440 nm is dominant suggesting only small intermediate clusters have formed. After 1 hr, shown in black, some AuNCs are seen to form due to the formation of a peak at 640 nm, the intermediate peak is seen to decrease showing that the intermediate product has grown into larger AuNCs. After 6 hrs, shown in green, the peak has red shifted to 670 nm and increased in size, indicating that the synthesis of fully formed AuNCs has completed.

Initially there was a strong emission at 440 nm, implying that a large amount of intermediate product (*e.g.* small AuNCs) initially exists with no emission in the red regime of the spectrum. After 6 hours, a large characteristic peak at 670 nm associated with fully formed AuNCs was present with a large decrease in fluorescence from the intermediate products suggesting that they had formed larger AuNCs.

With the knowledge that the two characteristic peaks change over time during the synthesis of AuNCs in free HSA, both peak positions were observed during the synthesis of AuNCs using HSA with warfarin pre-bound. The results are displayed and compared to AuNCs forming in free HSA in Figure 4.11.

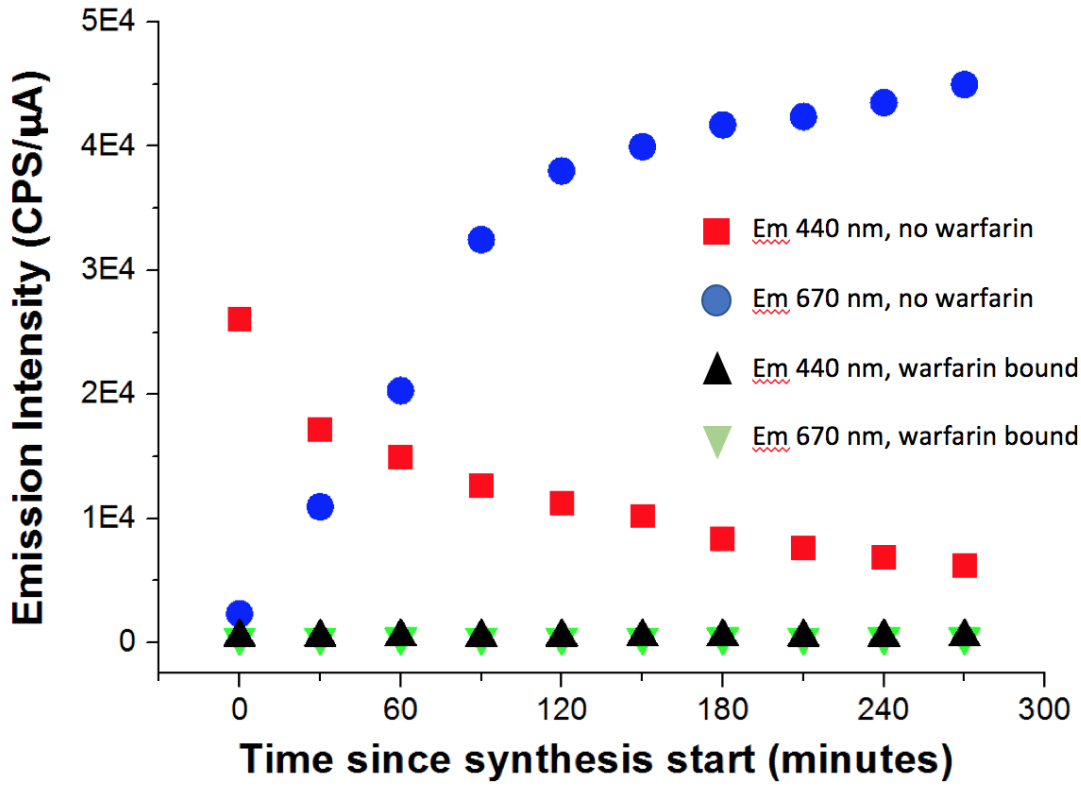

Figure 4.11: Time evolution of the fluorescence intensity peak emissions at 440 nm and 670 nm during AuNC synthesis with HSA and HSA with warfarin bound. The 440 nm and 670 nm peaks for native HSA-AuNCs synthesis are shown in red and blue respectively. The 440 nm and 670 nm peaks for synthesis using HSA with warfarin pre-bound is shown in green and black respectively. The lack of peaks either for the intermediate product or final AuNCs during synthesis with HSA that has warfarin prebound suggests that the gold salt cannot interact with HSA when warfarin is bound.

In the case of native HSA, the emission at 440 nm decreases overtime, while the emission with a peak between 640 - 670 nm increases. This indicates the decrease in intermediate gold products as they further grow into larger AuNCs. The lack of fluorescence at either 440 nm or 640 nm for the synthesis using HSA with prebound warfarin indicates that neither intermediate products nor larger AuNCs form at any time during the synthesis attempt. The bound warfarin affects the ability of HSA to interact and bind with the gold salt present in solution during synthesis.

From the previous chapter, molecular dynamics was used to observe gold atoms interacting with the Sudlow I major drug binding site for a short amount of time before terminating at one of the AuNC nucleation sites. Tyrosine has been shown to play a critical factor in the reduction of gold salt; of which an accessible residue resides within the Sudlow I binding site. It is possible that this tyrosine residue (position 149 for BSA, position 148 for HSA in the polypeptide chain) plays a critical role in the reduction of the gold salt molecules during synthesis. Warfarin binding to the amino residues arginine and lysine may block the accessibility of this tyrosine molecule to gold salt while it is bound to HSA. This explains the lack of small intermediates forming in the case of HSA with prebound warfarin. This also explains why warfarin cannot bind to HSA-AuNCs; it is possible that excess gold salt or by-products of the reduction reaction block the Sudlow I binding site. Chlorine ions have been previously reported to have a high affinity for histidine[206]. The chlorine bond to the positively charged nitrogen centres of these residues through hydrogen bonding. If the leftover chlorine ions from the gold salt reduction bind to the previously mentioned residues present in the Sudlow I binding site, then access could be physically hindered for warfarin binding. Due to the very low concentration of excess chlorine ions it is not possible that the protein would be drastically altered. It is suggested that the warfarin binding affinity decreases with chlorine ion concentration, due to both competing for the same binding site[207]. The presence of chlorine ions would also change the steric attraction between warfarin and the Sudlow I binding site lowering the overall binding affinity. Another factor to consider is the formation of possible dimers and aggregates after AuNC synthesis. The formation of aggregates could also physically block warfarin access to the entrance of the Sudlow I binding site. Alternatively changes in the surface charge of

the protein upon AuNC synthesis may be responsible for the lack of warfarin-HSA binding. Further studies, shown in Chapter 5, are required to better understand the physico-chemical characteristics of HSA before and after AuNC synthesis.

4.5 Conclusions

Warfarin has been successfully utilised as a probe to study the influence of AuNCs nucleation within HSA on the protein's functionality. It was observed that warfarin was unable to bind to HSA-AuNCs, implying that the Sudlow I major drug binding site of HSA is directly affected by the presence of AuNCs within the protein. This suggests that the Sudlow I binding site may have an important role in the gold atom transport and nucleation. The most likely reason for this is that the tyrosine residue present in the Sudlow I binding site plays a critical role in the reduction of gold salt and subsequent formation of AuNCs during the synthesis. These findings must be taken into consideration in the future if HSA-AuNCs are to be used as fluorescent probes in the study of biological processes where the Sudlow binding I site is important; such as monitoring patients who are drug dependent. It is currently not clear whether other drug molecules binding to the Sudlow I binding site of HSA are affected by the presence of AuNCs and further studies would be required. The limiting factor of studying further drugs using the techniques and methods in this chapter arises when finding suitable fluorescent drug molecules which have clearly defined changes to their fluorescence characteristics upon binding to HSA. It is also important to highlight other possible reasons for the lack of warfarin binding to HSA-AuNCs such as changes to surface chemistry of the protein upon AuNC synthesis or the formation of aggregates. Further studies of the physico-chemical properties are vital to better understand the changes HSA undergoes upon AuNC formation and will be explored in the next Chapter.

5 Uncovering the Physicochemical Properties of HSA-AuNCs

5.1 Abstract

In the previous chapter, it was shown that the fluorescent drug molecule warfarin cannot bind to Sudlow I major drug binding site of HSA after the synthesis of AuNCs. Similarly, AuNCs could not be successfully grown when warfarin was pre-bound to HSA, raising questions as to what extent the presence of AuNCs in HSA changes the proteins native physico-chemical characteristics. To better understand the reasons why warfarin did not bind to HSA-AuNCs, physicochemical methods were used to provide a greater understanding the extent to which AuNCs synthesis changes HSA's physical properties. It is hoped that a greater understanding of HSA-AuNCs physical properties can aide in the improvement of its fluorescence characteristics.

The differences in physicochemical properties between HSA and HSA-AuNCs have been characterised. The molecules' light absorbance (UV-Vis), electrophoretic mobility, dynamic viscosity, density, hydrodynamic radius (DLS), absorption (QCM) and chemical bonding (XPS) characteristics were studied. UV-Vis and DLS studies indicate the formation of large HSA-AuNC aggregates between the pH range of 4 - 6 which is not observed for native HSA. This observation was further supported by QCM measurements showing a large increase in adsorbed mass at pH 6 for HSA-AuNCs in comparison to native HSA. The DLS data also revealed a hydrodynamic radius of 12 nm for HSA-AuNCs, nearly double that of 7 nm for native HSA at pH higher than 6, suggesting the formation of compact HSA-AuNCs dimers. Density and viscosity measurements of HSA-AuNCs agreed with the theory that dimers are formed upon AuNC synthesis.

Electrophoretic mobility experiments for both HSA and HSA-AuNCs were carried out and the resulting values were converted to zeta potentials. The zeta potential of HSA-AuNC was seen to be more negative between pH 6 - 12, suggesting that the protein surface is interacting with unreacted gold salt anions. X-ray photoelectron

spectroscopy (XPS) data also suggested that the protein surface and positive side chains play a major role in the initial synthesis stages.

In this chapter, it is concluded that HSA-AuNCs form dimers at natural and high pH. Between pH 4 - 6 HSA-AuNCs form very large aggregates limiting their use as a fluorescent probe in this pH range. Further to this we can conclude that the main cause for the lack of drug binding previously seen is a result of either the formation of dimers physically stopping warfarin from entering the drug binding site or the changes in protein surface chemistry radically alter the interactions between HSA and warfarin. The clear differences in physicochemical properties of HSA and HSA-AuNCs must also be considered when applying HSA-AuNCs as a fluorescent probe in biological imaging and sensing.

5.2 Introduction

Previously it was found that the synthesis of AuNCs inside HSA alters the binding affinity of warfarin to the major drug binding site, Sudlow I. However, the explicit reasons how AuNC synthesis affect the HSA proteins physico-chemical characteristics so that warfarin no longer binds remains unsolved. To better understand the changes HSA undergoes during synthesis a range of characterisation experiments were carried out on HSA-AuNCs and compared with native HSA. It is believed that by understanding the physical characteristics of HSA-AuNCs that any implications for drug binding and molecule transport *in vivo* experiments could be better understood. Secondly, it is hoped that a better understanding of the physical properties of HSA-AuNCs will allow for more intelligent strategies to be developed for enhancing the photo physical properties of the fluorophore.

Previous studies concerning changes to the secondary structure of HSA after AuNC synthesis were carried out using Circular Dichroism (CD) and Fourier-Transformed Infra-Red spectroscopy (FTIR)[208,209]. Santosh *et. al.* discovered that the secondary structure of HSA, which is mainly alpha-helical in nature, undergoes minor perturbations during AuNC synthesis and only minor changes occur to the secondary structure of HSA. Yong *et. al.* similarly discovered that the secondary structure of

HSA is not affected by the presence of AuNCs, however, the alpha-helical content of HSA can decrease irreversibly after the synthesis of HSA-AuNCs. Therefore, changes to the HSA natural function cannot be attributed to changes in secondary structure and must be due to other physical changes of the protein upon AuNC synthesis.

In this chapter DLS, electrophoretic mobility, UV-Vis, dynamic viscosity, QCM and XPS were applied to build up a well-rounded understanding of the physical properties of HSA and HSA-AuNCs under different pH conditions.

5.3 Experimental

5.3.1 Sample Preparation

HSA (crystallized and lyophilized powder), (≥ 99 %) and Gold(III) Chloride Hydrate were purchased from Sigma Aldrich and used without further purification. A stock solution of HSA-AuNCs was prepared using Xie's method as previously carried out in previous chapters and stored at 4 °C until use. A separate stock of HSA was prepared under the same conditions but without adding the gold salt during preparation. The stock solutions were diluted with NaCl (ionic strength, $I = 10^{-2}$ M) to a range of concentrations between 5 - 10,000 ppm immediately before use. Multiple stock solutions of HCl and NaOH at different concentrations were used to control the pH of all samples. Doubly distilled, degassed water was used for the preparation of all solutions. All experiments were carried out at 25 °C. All other chemicals used were procured from Sigma-Aldrich.

5.3.2 Experimental Methods

Viscosity and density measurements were carried out using a combined Anton Paar DMA 5000M digital vibrating U-tube densimeter with a precision of 5 x 10^{-6} g.cm^{-3} and an Anton Paar Lovis 2000 ME rolling ball microviscometer with a precision of 0.001 s. The viscosity and density of both HSA and HSA-AuNCs were measured across a concentration range of 50 – 10,000 ppm. All dilutions were carried out with degassed NaCl (concentration of I = 10^{-2} M).

DLS measurements were carried out using a Malvern Zetasizer Nano ZS with a measurement range of 0.6 nm – 0.6 μm. The diffusion coefficients of each sample (pH range of 1 - 12) were measured at a concentration of 1,000 ppm. The diffusion coefficients (D_{CF}) were determined by monitoring the fluctuations in the intensity of backscattered light from the samples due to the Brownian motion they undergo. The diffusion coefficients were calculated from the time correlation function shown in Equation 2.26. Using the Einstein-Smoluchowski relation (Equation 2.30), the hydrodynamic radii (R_H) were calculated from the diffusion coefficients and converted to a particle size distribution.

Zeta potential measurements were carried out using a Malvern Zetasizer Nano ZS with a measurement range of 3 nm – 10 μm and an accuracy of 0.12 μm.cm.V^{-1}s^{-1}, utilizing LDV. A voltage was applied across a folded capillary cell supplied by Malvern. The same cell was used for each measurement to minimize any differences between cell electrodes. The applied voltage causes charged particles to migrate to their oppositely charged electrode and their velocity is expressed as the electrophoretic mobility (μ_e). The electrophoretic mobility was measured for all samples at a concentration of 1,000 ppm across a pH range of 3 - 12. Using Henry's Equation (Equation 2.31) the electrophoretic mobility values were converted to zeta potentials.

UV-Vis measurements were carried out using a Perkin Elmer 25. All measurements were carried out at a concentration of 1,000 ppm.

QCM measurements were carried out using a Q-Sense E1 QCM-D. Sensors with gold electrode surfaces were used for all experiments. A constant flow of 500

$\mu L.min^{-1}$ was used throughout the experiment. Initially NaCl solution was passed over the sensor for 10 minutes to set a baseline for the adsorption. The sample solution was then passed over the sensor for 90 minutes at a concentration of 5 ppm and over a pH range of 4 - 9, during which time the adsorption was monitored. NaCl was then rinsed over the sensor surface for another 90 minutes to observe whether the adsorption of protein to the fold surface was irreversible. Before each measurement the sensor was cleaned using the same protocol. The Sauerbrey model (Equation 2.35) was utilized to correlate changes to the frequency at which the quartz crystal resonated at to the mass of protein adsorbed to the sensor surface. The decay of the quartz crystal oscillations, E_{dis}, were also recorded throughout all QCM experiments.

XPS measurements were carried out using a Gamma data Scienta SES R4000 hemispherical analyser. All measurements were performed using an Al Kα (E = 1486.6 eV) X-ray source operated at 200 W. The spectra were recorded in normal emission geometry with an energy resolution of 0.9 eV. Calibration was performed per normal procedures, ISO 15472:2001.

5.4 Results and Discussion

5.4.1 Determining the Hydrodynamic Diameter and Zeta Potential of HSA-AuNCs

To characterise the physicochemical differences between HSA and HSA-AuNCs the hydrodynamic radius R_H was determined from the diffusion coefficients using the DLS technique. The sample concentration was kept at 1,000 ppm and the pH was measured over a range of 1 - 12. The diameters for both HSA and HSA-AuNCs are shown in Figure 5.1.

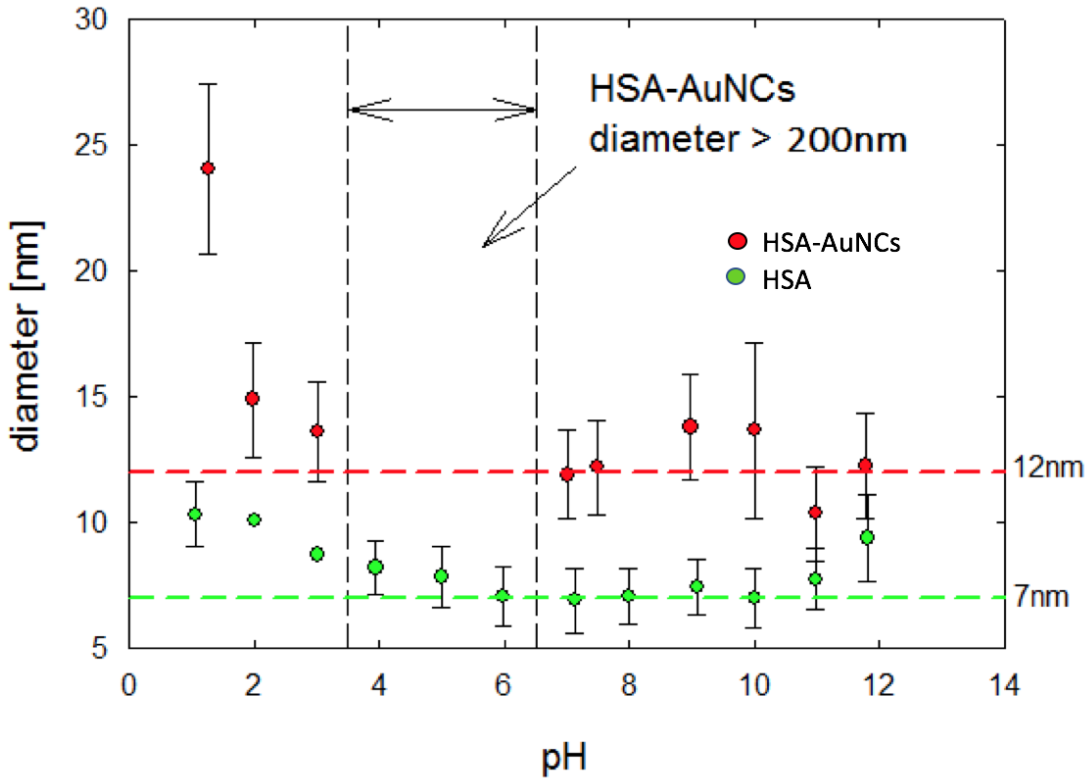

Figure 5.1: The hydrodynamic diameters as a function of pH. HSA is shown in green while HSA-AuNCs is shown in red. For the pH range 4 - 6 HSA-AuNCs were observed to form large aggregates which were poly disperse in nature and larger than 200 nm.

The hydrodynamic diameter of HSA was found to be 7 nm at neutral pH which compares well with previously published results[210,211]. The diameters of HSA-AuNCs across the pH range of 7 - 12 were nearly double at 12 nm. This suggests the formation of tightly packed dimers upon AuNC nucleation within the protein. Previously it has been shown that at low pH the protein structure beings to open, creating an unfolded conformation typically referred to as the "extended" form[174]. Shaw *et. al.* also report that at high pH the protein begins to swell due to hydrophobic pockets near the surface burying themselves further inside the protein to avoid solvent exposure. These observations agree with the observations seen here for both HSA and HSA-AuNCs whose diameters increase below pH 5 and the increase in diameter for HSA above pH 10. The diameter of HSA-AuNCs however remains unchanged upon increasing the pH above 10. The largest difference between HSA and HSA-AuNCs diameter was seen between pH 4 and 6. Previously HSA has been shown not to aggregate close to its pKa value of ~4.9 (solution conditions such as the buffer used can shift the pKa value slightly lower or higher)[212]. The results presented agree well with this, however HSA-AuNCs were seen to aggregate and become polydisperse with diameter values greater than 200 nm. Interestingly the aggregation was seen to be reversible upon immediately changing the pH outside the range of 4 - 6.

UV-Vis measurements of both HSA and HSA-AuNCs across a pH range of 1 - 12 were taken. It was found that at 280 nm the extinction of HSA is not affected by pH. However, an increase in extinction for HSA-AuNCs was observed between pH 4 -6, shown in Figure 5.2.

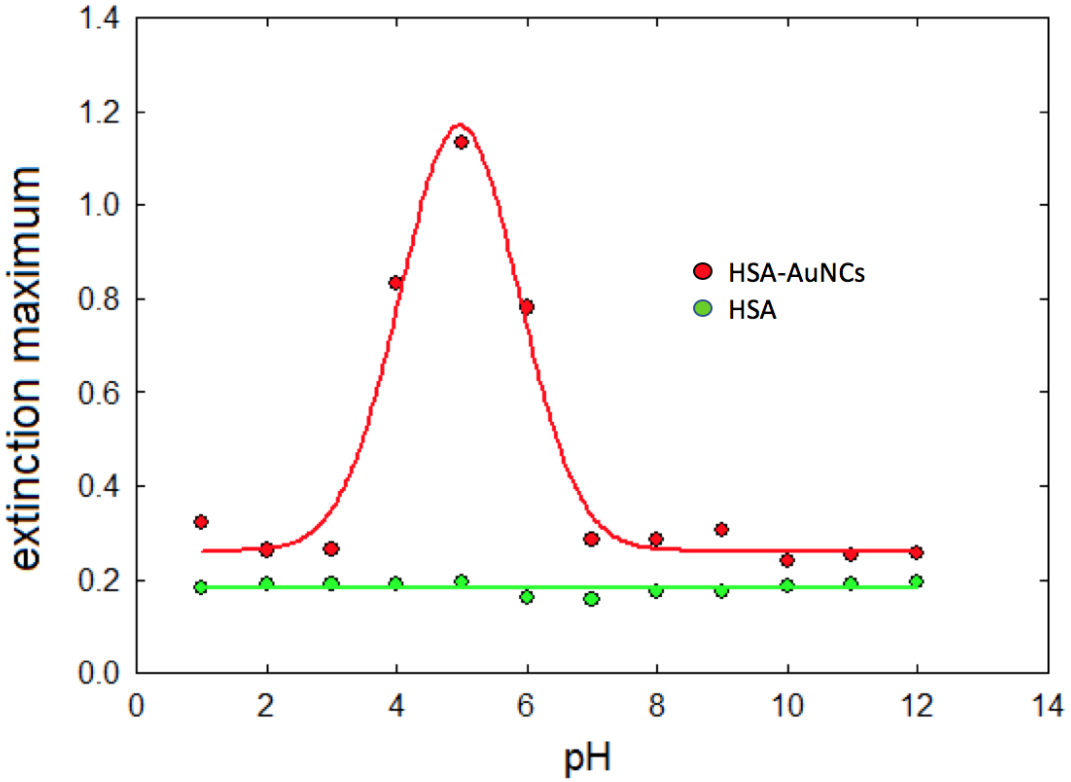

Figure 5.2: UV-Vis absorption at 280 nm as a function of pH for HSA is shown in green, while HSA-AuNCs is shown in red. The absorption maximum of HSA-AuNCs can be seen to dramatically increase between pH 4 - 6, showing that the fluorophore aggregates in this pH range.

This increase in extinction can be attributed to the aggregation of HSA-AuNCs as previously observed during the DLS measurements. As the protein aggregates the larger particles scatter more light than those in monomer form. In addition, the presence of the AuNC also influences the increase in the overall absorption of the molecule complex at 280 nm even in the proposed HSA-dimer form. It is likely that both factors contribute to the increase in extinction.

The electrophoretic mobility of both HSA and HSA-AuNCs were measured across a pH range of 3 - 12. Zeta potentials for both HSA and HSA-AuNCs were calculated from the electrophoretic mobility data. The dependence of the zeta potential on pH for both samples are shown in Figure 5.3.

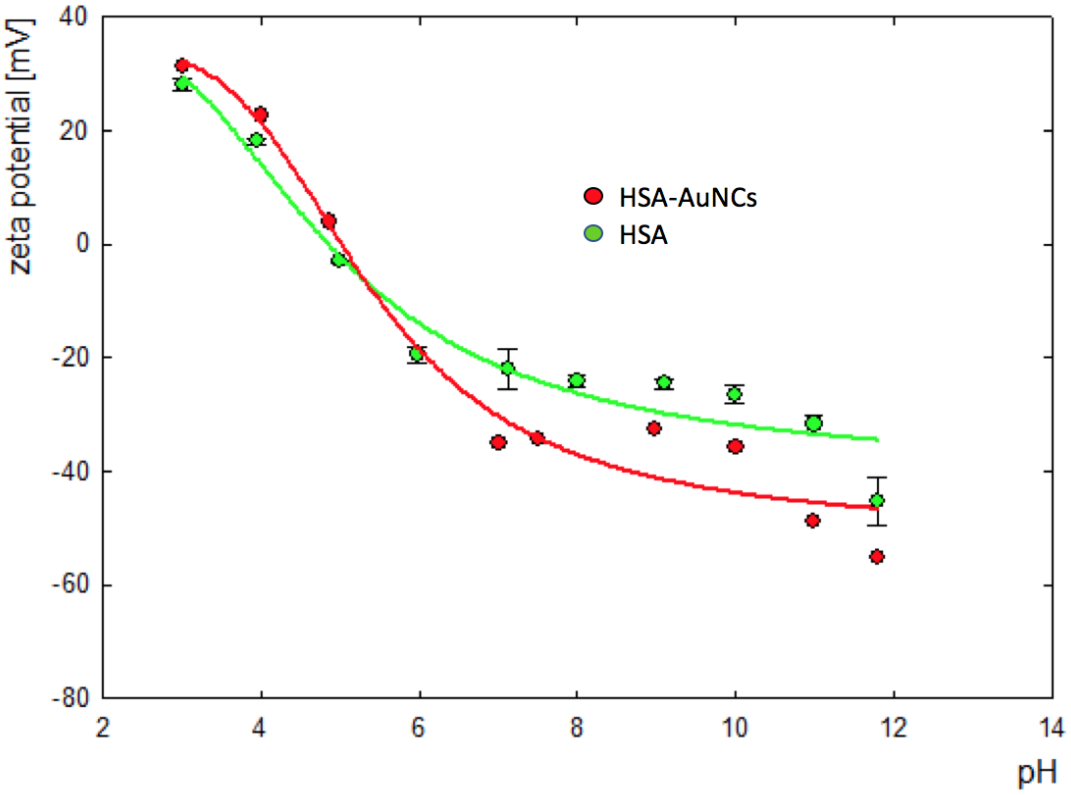

Figure 5.3: Zeta potentials of HSA and HSA-AuNCs as a function of pH. The zeta potentials of HSA are shown in green while the zeta potentials of HSA-AuNCs are shown in red.

The zeta potential curve as a function of pH with an ionic strength of 1 x 10^{-2} compares well with previously published work[212]. A large decrease in the zeta potential of HSA-AuNCs of 8 - 14 mV in comparison to the zeta potential of HSA was observed at pH greater than the isoelectric point (from pH 7 - 12). A slight increase of 3 - 4 mV in the zeta potential for HSA-AuNC in comparison to HSA was observed at pH below the isoelectric point (from pH 3 - 5). Both differences were seen to be much larger than the total error for each measurement. Error bars for each measurement were found to be small and insignificant to the comparison between both datasets. The decrease in zeta potential above the isoelectric point may be attributed to the reduction reaction that the gold salt undergoes during the synthesis of AuNCs. It is believed that at highly alkaline pH (pH greater than 10) tyrosine reduces the salt before the gold atoms nucleate and bond to sulphur found within

cysteine residues[51,213]. If this is true, then the phenol functional group would become more negatively charged after the reduction reaction and create a more negatively charged surface in comparison to native HSA. Another possibility is that all gold salt which initially interacts with the protein surface is reduced. The positively charged functional side chains of Lysine and Arginine residues on the surface of the protein could interact with the intermediary synthesis complex $AuCl_4^-$. This would also explain the more negative zeta potential of the HSA-AuNC complex compared to native HSA.

5.4.2 Determining the Density and Viscosity of HSA-AuNCs

The density of HSA and HSA-AuNCs was measured across a concentration range of 50 - 10,000 ppm, diluted from stock solution using degassed NaCl solution ($I = 1 \times 10^{-2}$). The pH of the HSA and HSA-AuNCs at 10,000 ppm was 6.83 and upon dilution the pH increased to a maximum of 7.12 at 5 ppm. The difference in density between HSA-AuNCs and HSA can be seen in Figure 5.4.

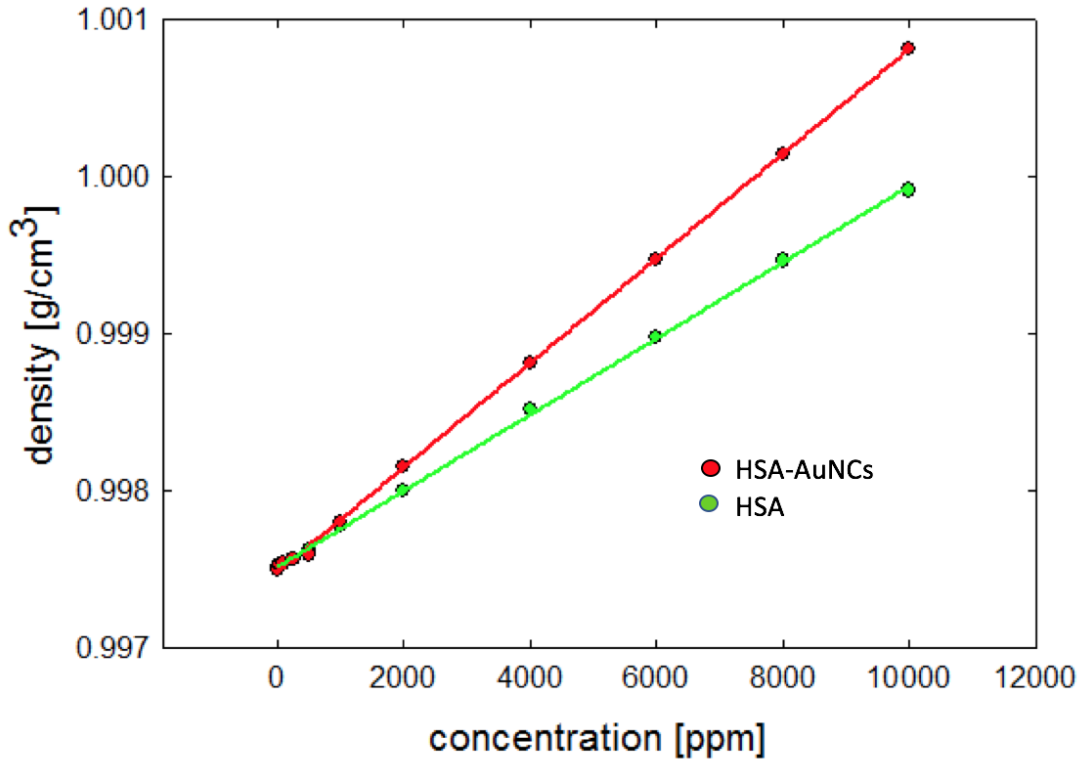

Figure 5.4: Density of HSA and HSA-AuNCs as a function of concentration. The densities of HSA are shown in green while the densities of HSA-AuNCs are shown in red.

Unsurprisingly, the density of HSA is seen to increase upon the formation of AuNCs within the protein. The density of HSA and HSA-AuNCs samples were both measured at pH levels higher than the range where aggregation of HSA-AuNCs was observed in both DLS and UV-Vis measurements. HSA-AuNCs were forming smaller aggregates seen at pH > 6, rather than the larger aggregates seen at pH < 6 from DLS and UV-Vis measurements. To better quantify the increase in density upon synthesis of AuNCs in HSA both values were converted to the relative density values.

The relative density of a material can be simply described as the ratio of the density of a substance to that of a reference solvent[212]. The NaCl solution used to dilute the samples was used as the reference material for the relative density calculations of HSA and HSA-AuNCs. For each measurement, the value was converted to density as a function of the weighted fraction of the solution, shown in Figure 5.5.

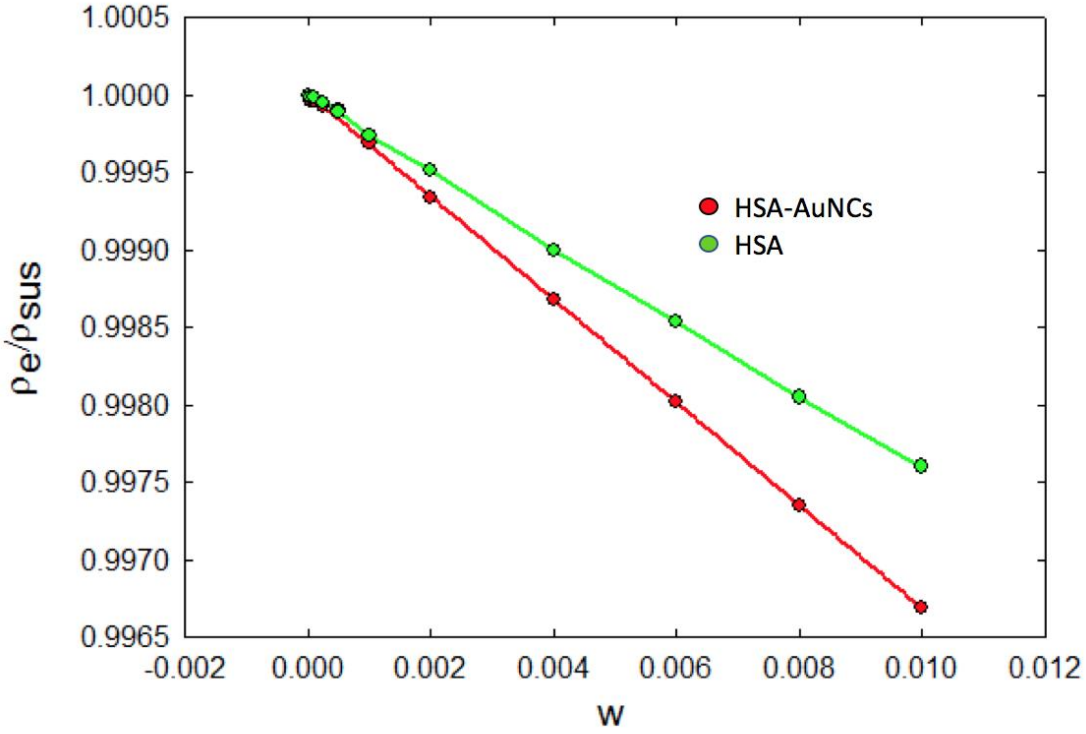

Figure 5.5: Relative density of HSA and HSA-AuNCs as a function of weighted fraction. The relative density gradients of HSA are shown in green while the relative densities of HSA-AuNCs are shown in red. The gradients for HSA and HSA-AuNCs were found to be -0.2413 and -0.3305 respectively; giving HSA a relative density of 1.32 g.cm^{-3} and HSA-AuNCs a relative density of 1.49 g.cm^{-3}.

HSA was found to have a relative density of 1.32 $g.cm^{-3}$. This compares well with the previously reported value of 1.33 $g.cm^{-3}$ for proteins[214,215]. The relative density value for HSA-AuNCs however was found to be much larger at a value of 1.49 $g.cm^{-3}$. The large increase in relative density upon AuNC synthesis can be directly correlated with the presence of the AuNCs inside the proteins since there was no introduction of other molecules outside of the synthesis and the formation of dimers or aggregates cannot account for such a large rise in relative density.

If the increase in relative density is attributed solely to AuNCs then an average of 43 gold atoms are present per protein. This number is higher than the expected 25 atoms per nanocluster; however unreacted gold salt attached to the protein and secondary, smaller non-fluorescent AuNCs bound to the protein could account for this.

The dynamic viscosity of both HSA and HSA-AuNCs was observed over a concentration range of 5 - 10,000 ppm to better understand how the formation of dimers affects the protein in solution at higher concentrations. Again, the pH of the HSA and HSA-AuNCs at 10,000 ppm was 6.83 and upon dilution increased to a maximum of 7.12 at 5 ppm. The trend in viscosity for both HSA and HSA-AuNCs as a function of concentration can be seen in Figure 5.6.

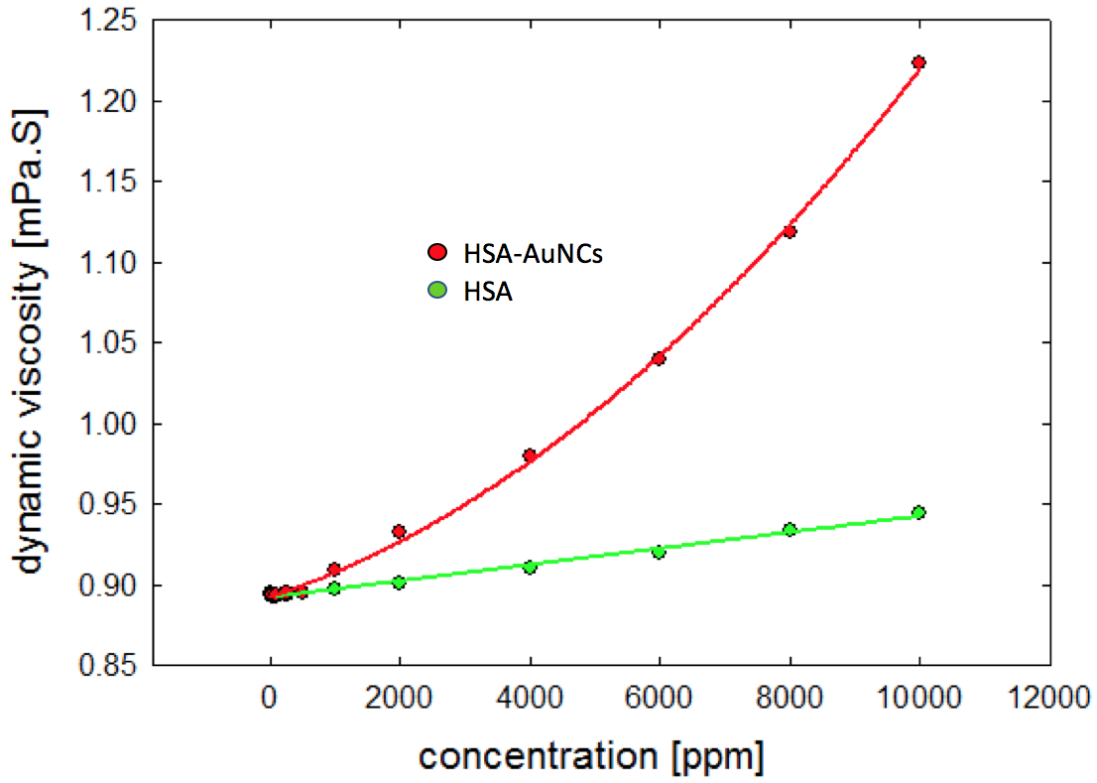

Figure 5.6: Dynamic viscosity of HSA and HSA-AuNCs as a function of concentration. The dynamic viscosity values of HSA are shown in green while the dynamic viscosity of HSA-AuNCs is shown in red.

The viscosity of native HSA increases linearly with concentration, however in the case of HSA-AuNCs the increase is non-linear, increasing at a faster rate than native HSA. The relative increase in viscosity agrees well with previous the measurements in this chapter showing the formation of HSA-AuNCs aggregates. Due to the pH being higher than 6, the increased viscosity in HSA-AuNCs is due to the formation of smaller aggregates such as dimers rather than larger aggregates seen in the pH range 4 - 6. This could give rise to potential problems using HSA-AuNCs as a fluorophore at high concentrations during *in vivo* experiments. An increase in HSA viscosity has been shown to be linked with multiple health problems such as cardio vascular disease, heart attacks and strokes[216,217].

5.4.3 Determining HSA-AuNCs Adsorption Characteristics

Differences in the adsorbed mass of HSA and HSA-AuNCs were studied using the QCM method. The samples were measured between a range of 4 - 9, using NaOH and HCl to alter the pH, and at a concentration of 5 ppm. The results of this experiment are shown in Figure 5.7.

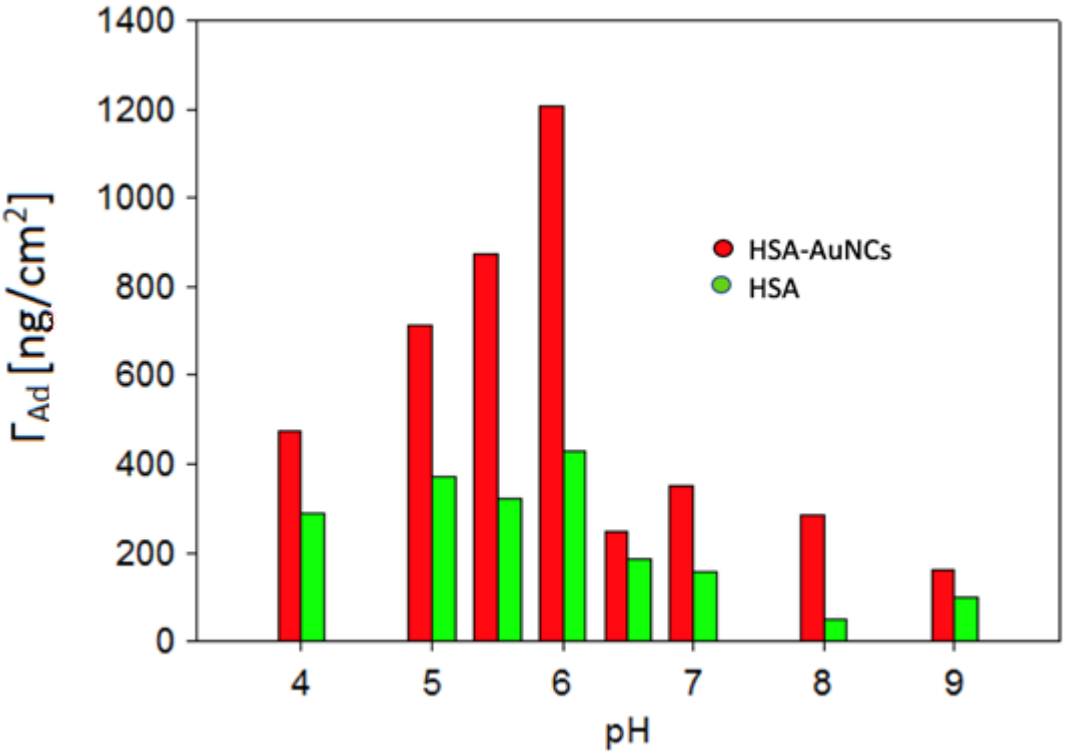

Figure 5.7: The mass of the adsorbed proteins is shown per unit of the geometrical sensor surface, depending on the pH of the solution. HSA is shown in green while HSA-AuNCs are shown in red. In both cases the maximum adsorption is observed at pH 6.

It was found that for both HSA and HSA-AuNCs the maximum adsorption took place when the pH of the solution was 6. The total mass of the adsorbed HSA-AuNCs is always seen to be higher across the whole pH range – this is unsurprising due to the additional mass associated with the attached AuNCs. The total additional adsorbed mass however is too large to attribute to the AuNCs alone. Between pH 4 -

6 the mass of HSA-AuNCs compared to HSA is 2 - 4 times larger. This result adds further weight to the idea that HSA-AuNCs do not exist in monomer form.

Differences in the physical features of HSA and HSA-AuNCs after adsorption onto the gold QCM sensor surface at pH 7 were studied using XPS. From the initial XPS survey it was observed that peaks attributed to Au 4f, O 1s, N 1s and S 2p were present. Of interest are the changes observed in the peak positions and atomic % for peaks in the N 1s band between HSA before and after AuNCs synthesis, since it is believed that the positively charged side chains of Arginine and Lysine could play a part in the synthesis of AuNCs in proteins[218]. The high-resolution spectra for the N 1s group are shown in Figure 5.8.

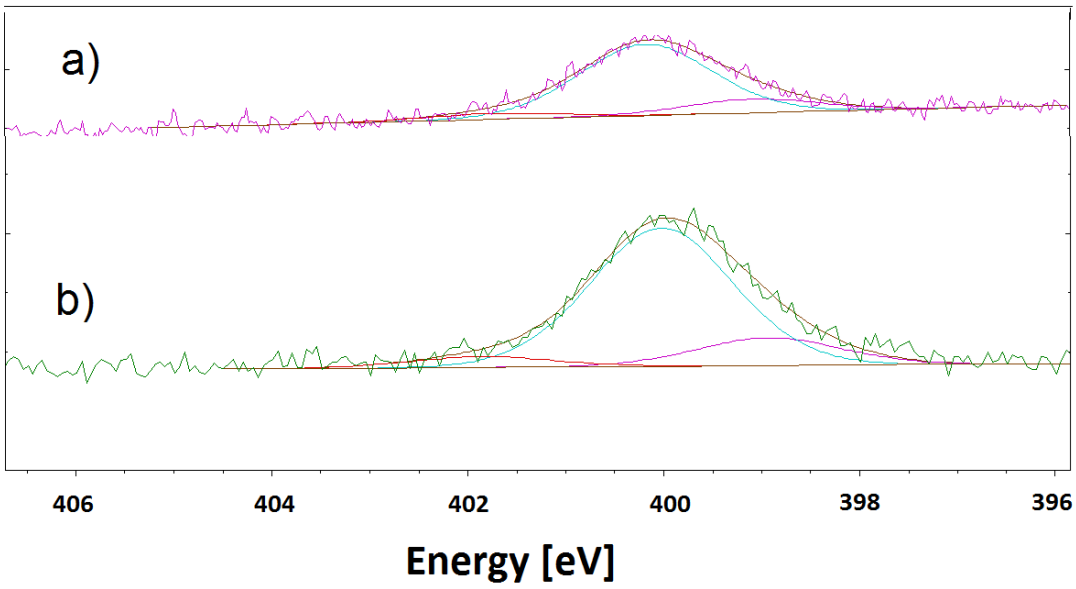

Figure 5.8: High resolution XPS spectra of the N 1s peak for HSA (spectrum a) and HSA-AuNCs (spectrum b) adsorbed on a gold surface at pH 7. The spectra were decomposed into 3 individual peaks associated with slightly different energies.

Both peaks were broken down into 3 peaks with distinct energies: 399.08 ± 0.20 eV, 400.18 ± 0.10 eV and 401.70 ± 0.40 eV. The first peak is attributed to amine or amide NH groups; the second peak is attributed to NH_2 and the third peak attributed to protonated amines NH_3^{+219}. The full set of data from decomposing the high-resolution N 1s peak is shown in Table 5.9.

Sample	HSA-AuNCs pH 7	HSA pH 7
Peak 1 (eV)	399.08	398.92
FWHM 1 (eV)	1.600	1.713
Atomic %	15.40	15.74
peak 2 (eV)	400.18	400.02
FWHM 2 (eV)	1.600	1.713
Atomic %	77.99	78.16
peak 3 (eV)	401.70	401.85
FWHM 3 (eV)	1.600	1.713
Atomic %	6.60	6.10

Table 5.9: Peak positions of the decomposed N 1s peak and the calculated parameters taken from the high resolution XPS spectra shown in Figure 5.4.3.3.

The relative decrease in atomic % for peak 3 indicates an overall decrease in protonated amines NH_3^+. This coincides with peak shifts to lower energies for both peak 1 and 2 suggesting that the protonated amines are reacting with negatively charged species on the protein surface; most likely gold salt intermediates, such as $AuCl_4^-$, which have not undergone full reduction. This result agrees well with the zeta potential measurements for HSA and HSA-AuNCs at pH 7. The zeta potential was seen to be 13 mV more negative in the case of HSA-AuNCs at pH 7 compared to HSA. This more negative zeta potential could also be explained by the presence of unreacted salt on the protein surface.

5.5 Conclusions

Important changes concerning the physicochemical characteristics of HSA were observed upon synthesising AuNCs within the protein using the one-pot method. It was found that HSA forms aggregates upon synthesising AuNCs; DLS measurements of HSA-AuNCs found that aggregates, most likely tightly packed dimers form at all pH apart from the range of 4 - 6 where larger aggregates with a diameter greater than 200 nm were formed. Differences in adsorbed mass to a gold surface also indicated the formation of small HSA-AuNCs aggregates. Concentration of protein was also ruled out as a factor; HSA at 1000 ppm were dimers or larger aggregates. The increase in viscosity can also be attributed to the formation of small aggregates of HSA-AuNCs in comparison to natural HSA. The formation of dimers must be considered if HSA-AuNCs are to be utilized as a fluorescent probe *in vivo*, since natural protein function and behaviour will be altered in the dimer form observed in this study.

The shift to a more negative zeta potential and changes to the atomic % from the XPS data suggests that while the AuNCs are formed inside the protein, not all of the gold salt fully reacts and migrates to the nucleation sites for AuNCs inside HSA. This could point to positively charged amino acid side changes on the protein surface interacting with negatively charged $AuCl_4^-$. The changes to the surface chemistry of the protein may alter the binding affinity of molecules which are typically transported by the HSA protein within the body. This raises questions as to whether AuNCs can be used as an intrinsic probe to study natural protein dynamics if the behaviour of the protein itself is altered upon AuNC synthesis. Further questions as to what extent AuNCs affect other proteins upon synthesis also remain unanswered. The final AuNC fluorescent properties have been reported previously to be very similar in several different proteins when the correct residues are present for the reduction of salt and stabilisation of gold atoms are present[181]. Do the physicochemical properties of other proteins used for AuNC encapsulation become altered in the same way as HSA? And does it have implications towards the utilisation of other protein encapsulated AuNCs? To test this idea, further physicochemical characterisations of another commonly studied system Lysozyme-AuNCs will be carried out in the next Chapter.

6 Uncovering the Physicochemical Properties of Ly-AuNCs

6.1 Abstract

In the previous chapter, it was shown that HSA undergoes many physicochemical changes upon AuNCs synthesis, critically that it forms tightly packed dimer/trimer aggregates at body pH (7.4) and that between pH 3 - 6 very large aggregates greater than 200 nm in size reversible form. The formation of aggregates could lead to complications when using the HSA-AuNCs fluorophore as an *in vivo* probe.

The formation of aggregates in HSA-AuNCs raised further questions about other protein-encapsulated AuNCs. Lysozyme is another commonly used protein for the synthesis of AuNCs and has the potential to be used as a tool to better understand the formation of lysozyme aggregates in brain diseases such as Parkinson's. However, for Ly-AuNCs to be used successfully as a method to study aggregation we must first understand the physicochemical differences between native Lysozyme and Ly-AuNCs – if the characteristics are radically different then AuNCs would not make an ideal probe for lysozyme aggregation.

The physicochemical properties of both lysozyme and Ly-AuNCs are presented. The molecules light absorbance (UV-Vis), electrophoretic mobility, dynamic viscosity, density, hydrodynamic radius (DLS), adsorption (QCM) and adsorption monolayer thickness (QCM) was studied. It was found that lysozyme forms small dimer/trimer aggregates upon the synthesis of AuNCs within the protein. The diameter for Ly-AuNCs was found to be 8.0 nm across a pH range of 2 - 11, with large aggregates with diameters greater than 20 nm forming between pH 3 - 5. The formation of larger aggregates limits Ly-AuNCs use as a fluorescent probe in this pH range. A large shift in the proteins isoelectric point was also observed, shifting from 11 to 4 upon AuNC synthesis. This resulted in major changes to the adsorption characteristics of lysozyme, observed during QCM. A monolayer of 8 nm was seen for Ly-AuNCs at pH 4, offering further evidence the proteins form small aggregates, unlike the natural monomer form of lysozyme. The adsorption of Ly-AuNCs was seen to decrease as

pH was increased; this is in major contrast with lysozyme absorption behaviour. At pH 7 however it was observed that absorption characteristics for lysozyme and Ly-AuNCs was similar suggesting that while the characteristics of both systems are different, it may be possible that Ly-AuNCs can be utilised to probe natural lysozyme aggregation in the future.

6.2 Introduction

The physicochemical characteristics of HSA have been shown to change dramatically upon the synthesis of AuNCs. While their use as a fluorescent dye in the labelling of *in vitro* cells for imaging or as a sensor for heavy ions should not be affected, it raises questions to their viability as a sensor in more complex *in vivo* situations. Another commonly used protein for the encapsulation of AuNCs is lysozyme due to its relatively cheap cost and abundance. It is hoped that through a physicochemical study of Ly-AuNCs it can be determined whether AuNCs could be used to study the aggregation of lysozyme.

Lysozyme is of interest to this study due to the role that it plays in human physiology. It is a relatively small bio-molecule with a molecular weight of 14,307 Da, comprising of two domains and a cleft in the protein centre which acts as the active site[219]. The secondary structure of each domain differs significantly, with one domain mainly β-sheet in structure and the other mainly helical[219]. Its main role is to attack the cell walls of bacteria, breaking the cell wall and causing the bacteria to burst under their own internal pressure[220]. Lysozyme AuNCs (Ly-AuNCs) have been shown to make excellent probes for the detection of mercury[55] and glutathione[221]. However, these have been *in vitro* experiments and to date no experiments using Ly-AuNCs *in vivo* as fluorescent probes have been carried out. The functionality of Lysozyme after AuNC synthesis has been shown to still be present to some degree as Liu et. al. successfully showed Ly-AuNCs still possessed good bio recognition for e. Coli[202].

A major problem that arises when protein structure changes in human physiology is the formation of large aggregate particles. The misfolding of Lysozyme has been shown to cause the formation of Amyloid fibrils; which have been linked to many human diseases such as Alzheimer's and Parkinson's disease[158,222,223] due to their insoluble nature. Therefore, it is important to understand how native lysozyme changes upon the nucleation of an AuNC within the protein for any future use of Ly-AuNCs as an in vivo probe.

In this work, we applied, electrophoretic mobility, UV-Vis, density, viscosity and QCM, measurement techniques to characterise the physicochemical properties of Lysozyme and Ly-AuNCs under different pH conditions to better understand how AuNC nucleation affects Lysozyme's natural state.

6.3 Experimental

6.3.1 Sample Preparation

Lysozyme (crystallized and lyophilized powder, from chicken egg white), (≥ 99 %) and Gold(III) Chloride Hydrate were purchased from Sigma Aldrich and used without further purification. A stock solution of Ly-AuNCs was prepared using Wei's *et. al.* method[55] and stored at 4 °C until use, a separate stock of Lysozyme was prepared, dissolving in purified water. The stock solutions were then diluted with NaCl (concentration of I = 10^{-2} M) to a range of concentrations between 5 - 5,000 ppm immediately before use. Multiple stock solutions of HCl and NaOH at differing concentrations were used to control the pH of all samples. Doubly distilled, degassed water was used for the preparation of all solutions. All experiments were carried out at 25 °C. All other chemicals used were procured from Sigma-Aldrich.

6.3.2 Experimental Methods

All DLS, Electrophoretic mobility, UV-Vis, Viscosity, Density and QCM measurements and analysis was carried out to the same methods as used in Chapter 5 (see **5.3.2 Experimental Methods** for details).

To determine the thickness of adsorbed mass in QCM measurements the Sauerbrey mass adsorbed to the sensor surface (Γ_{AD}) was divided by the density value of lysozyme[224], widely reported as 1330 kg.m^{-3}, as shown in Equation 6.1.

$$d_{eff} = \frac{\Gamma_{AD}}{\rho_{eff}} \qquad [6.1]$$

6.4 Results and Discussion

6.4.1 Determining the Hydrodynamic Diameter and Zeta Potential of Ly-AuNCs

Initially the hydrodynamic radius, R_H was determined for both lysozyme and Ly-AuNCs as a function of pH, across a pH range of 2 - 11, at a sample concentration of 1,000 ppm. The radius for each sample was calculated from the diffusion coefficient of the measured sample using the DLS technique. The determined diameters for Lysozyme and Ly-AuNCs are shown in Figure 6.1.

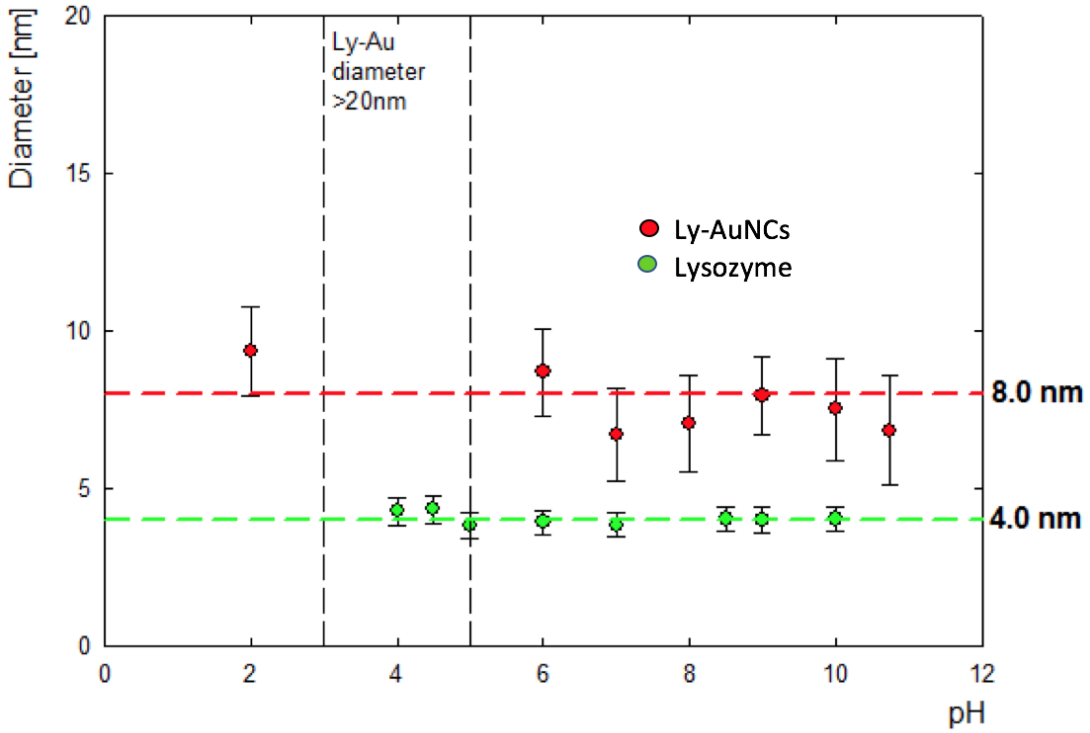

Figure 6.1: Hydrodynamic diameter of Lysozyme (green) and Ly-AuNCs (red) as a function of pH. For the pH range 3 - 5 Ly-AuNCs diameter are > 20 nm and polydisperse.

The hydrodynamic diameter by volume of Lysozyme was found to be 4.0 nm, between pH 4 - 10. The diameter of Lysozyme compares well with previous studies[225,226] and is stable at lower pH due to the smaller, more robust nature of the protein. The diameter of Ly-AuNCs was found to be significantly higher at 8.0 nm across the pH range. This suggests that the proteins are forming dimers or tightly packed trimers upon the synthesis of AuNCs. Between pH 3 - 5 the diameter of Ly-AuNCs was found to be greater than 20 nm and polydisperse, indicating the formation of large aggregates. The aggregation of protein encapsulated AuNCs at this pH has previously been observed, suggesting that the presence of AuNCs within the protein is directly responsible. The aggregation was also seen to be reversible by lowering or increasing the pH above or below the window of aggregation, indicating that no irreversible bonding between the lysozyme proteins takes place.

UV-Vis absorption spectroscopy measurements were taken of both Lysozyme and Ly-AuNCs under the same conditions as the DLS measurements shown previously, shown in Figure 6.2.

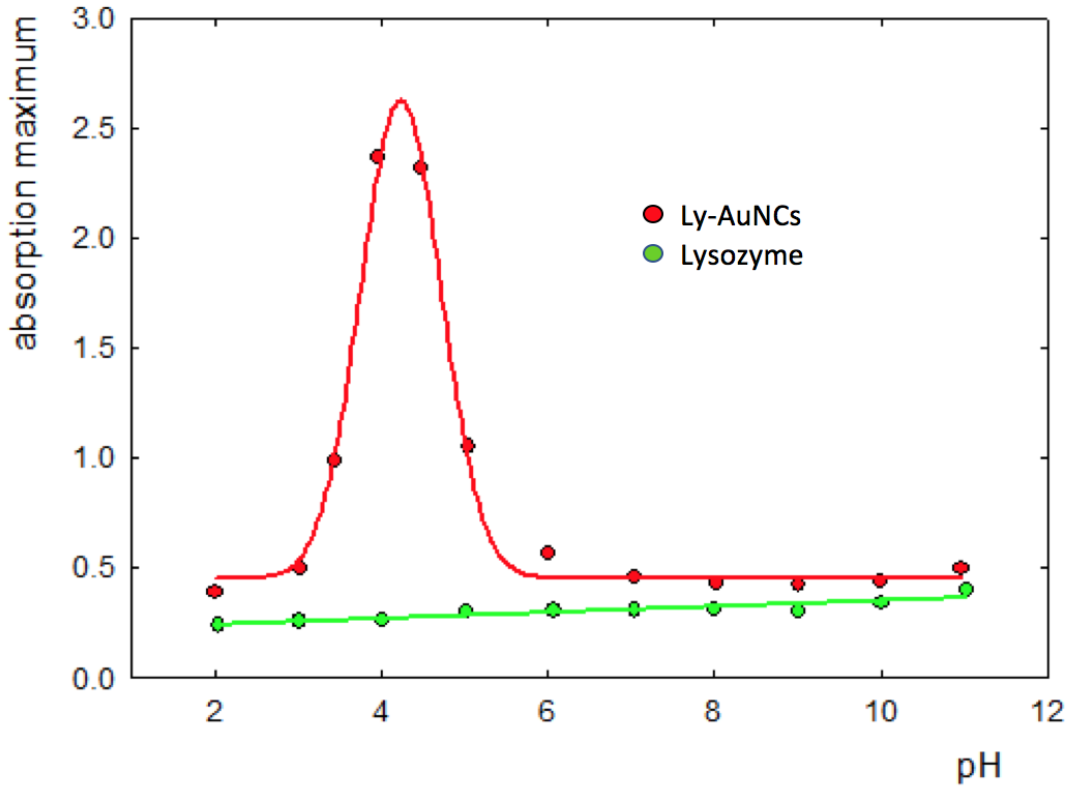

Figure 6.2: Maximum UV-Vis absorption of Ly-AuNCs (red) and Lysozyme (green) at 300 nm as a function of pH.

The absorption of Lysozyme can be seen slowly increasing as the pH approaches the isoelectric point at pH 11. The absorption of Ly-AuNCs is seen to be much higher across the whole pH range, due to the presence of the AuNCs. Between pH 3 - 6 the absorption of Ly-AuNCs increases dramatically, peaking around pH 4. This large increase coincides with a change in colour from clear to cloudy and matches the pH range at which aggregation of Ly-AuNCs was seen from DLS experiments, confirming the previous result. This result agrees well with the pH induced aggregation of HSA-AuNCs seen in chapter 5.

The electrophoretic mobility of both Lysozyme and Ly-AuNCs was measured across a pH range of 3 - 11, at a concentration of 1,000 ppm in both cases. The associated zeta potentials were calculated using Henry's Equation (Equation 2.31) and displayed in Figure 6.3.

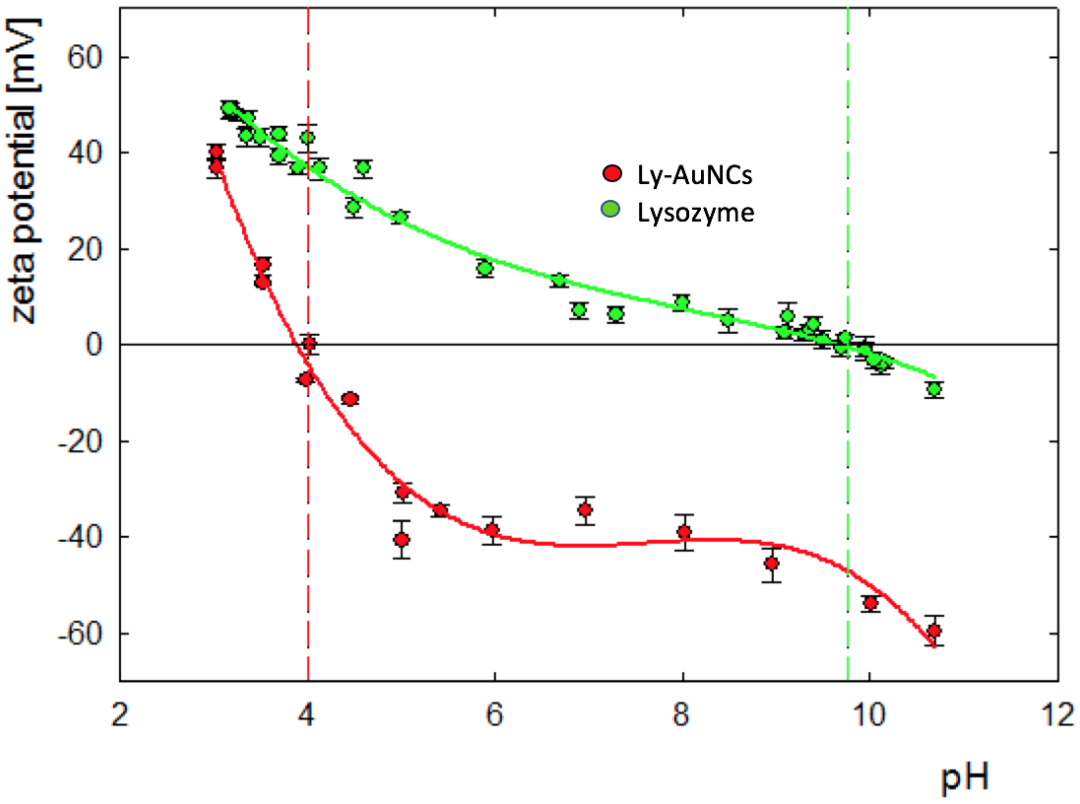

Figure 6.3: Zeta potential of Lysozyme and Ly-AuNCs as a function of pH. The zeta potentials of Lysozyme and Ly-AuNCs are indicated in green and red respectively.

The zeta potential curve for Lysozyme in a solution with ionic strength I = 1 x 10^{-2} M compares well with previously published results[227].The isoelectric point of Lysozyme in this case is approximately 10, in agreement with previous results[226]. In the case of lysozyme AuNC nucleation dramatically changes the zeta potential. From pH 5 to 11, there is a significant difference between lysozyme and Ly-AuNCs equal to 50 mV. Additionally, the shift in isoelectric point changes from 10 to 4. The zeta potentials across the pH range of Ly-AuNCs were found to be remarkably different.

Between pH 3 - 6 the surface charge of Ly-AuNCs was seen to drop rapidly from 40 mV to -40 mV. After pH 6 the surface charge was seen to continue to decrease at a lower rate, dropping to -60 mV at pH 11. The major changes to the zeta potential profile of Ly-AuNCs can be directly attributed to either the presence of the AuNCs or unreacted gold salt still attached to the protein surface[28]. The isoelectric point of Ly-AuNCs is like that of HSA-AuNCs, suggesting that the nucleation of AuNCs within proteins may result in the shifting of the isoelectric point to around 4.0, regardless of the proteins natural isoelectric point. This could have major implications of using protein encapsulated AuNCs in any situation where the pH of the environment being imaged or probed is close to this isoelectric value. Another factor which must be addressed is the change from a positive surface charge for natural lysozyme to a negatively charged surface for Ly-AuNCs at body pH (7.4). The charge decreases from 17 mV to -35 mV. The net positive charge of the lysozyme protein has been reported to play an important role in the initiation of its lytic action and its efficiency against the negatively charged cell walls of certain bacteria[228]. This result therefore raises questions to lysozyme's ability to function correctly after the synthesis of AuNCs.

6.4.2 Determining the Density and Viscosity of Ly-AuNCs

The density of lysozyme and Ly-AuNCs was measured across a concentration range of 0 – 5,000 ppm which was diluted from stock using degassed NaCl solution (I = 1 x 10^{-2} M). The difference between lysozyme and Ly-AuNCs density is shown in Figure 6.4.

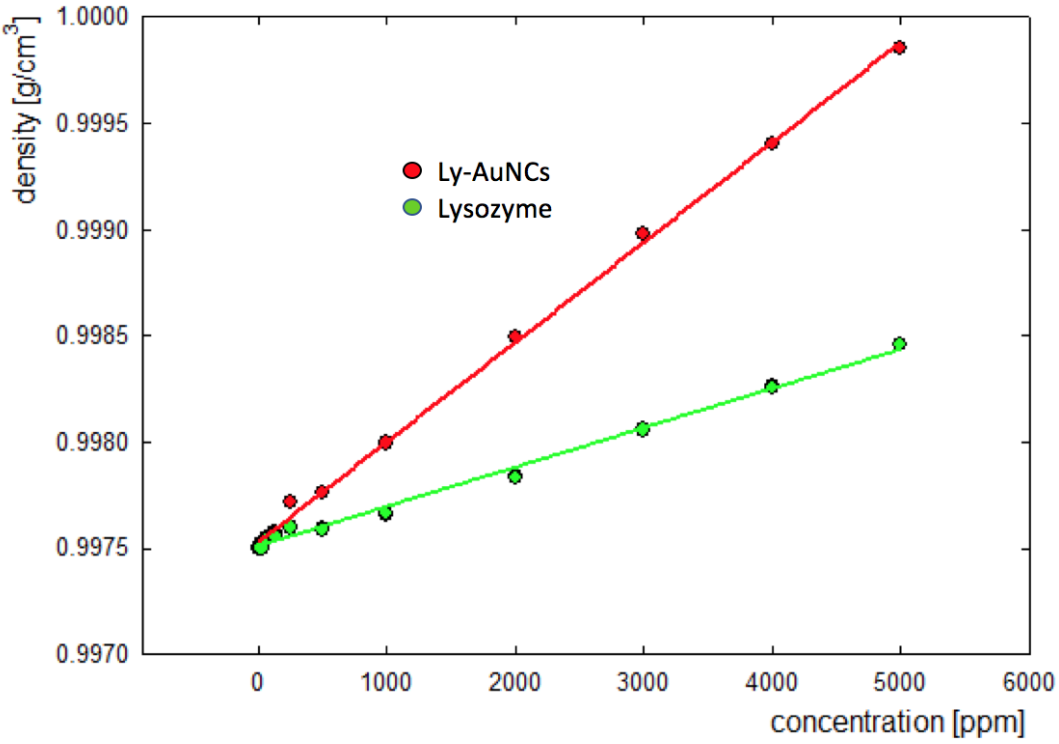

Figure 6.4: Lysozyme and Ly-AuNCs density as a function of concentration are shown. The density of lysozyme is represented by green while Ly-AuNCs density is represented by red.

The density of Ly-AuNCs is seen to be higher than Lysozyme due to the extra mass the presence of the AuNCs adds to the lysozyme protein. To properly quantify the increase in relative density the AuNCs have on the lysozyme protein, the values from Figure 6.4 were converted to relative density values and shown in Figure 6.5.

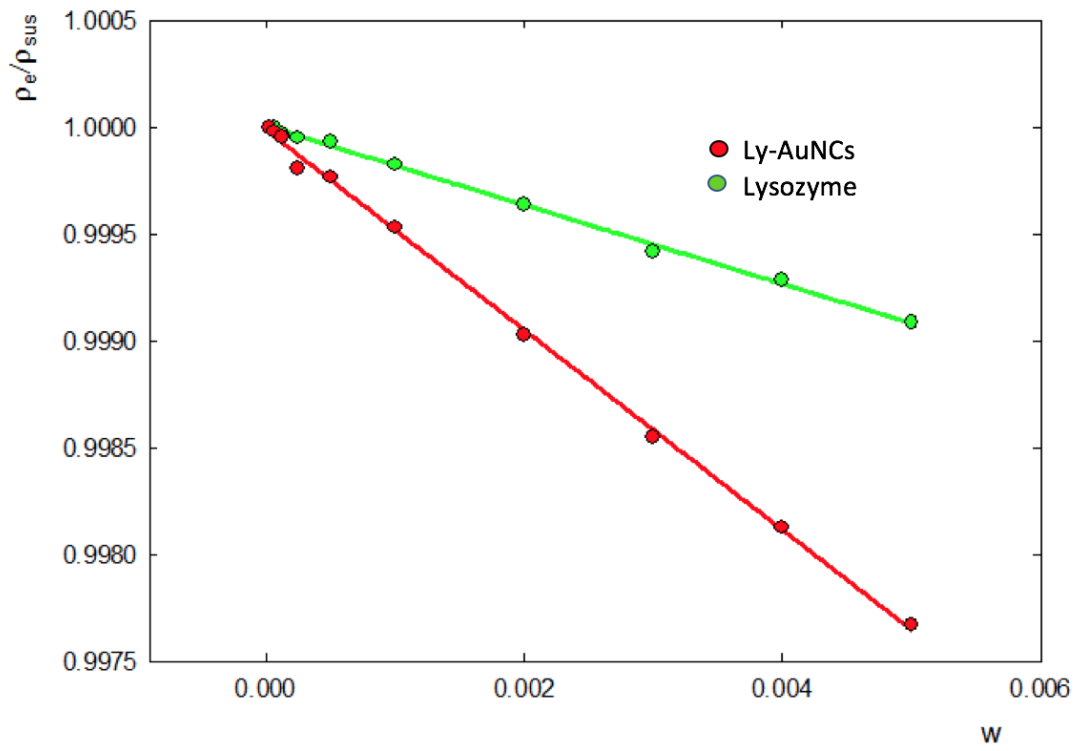

Figure 6.5: Relative density of lysozyme and Ly-AuNCs as a function of weighted fraction. The relative density gradient of lysozyme is shown in green while the relative density gradient of Ly-AuNCs is shown in red. The gradients for lysozyme and Lysozyme-AuNCs were found to be -0.1985 and -0.4680 respectively; this gave lysozyme a relative density of 1.33 while Ly-AuNCs had a relative density of 1.87.

The relative density of a material can be described as the ratio of the density of a substance to that of the reference solvent[228], in this case NaCl was used to dilute the lysozyme and Ly-AuNCs. For lysozyme, a relative density value of 1.33 $g.cm^{-3}$ was calculated, matching the previously reported value of 1.33 $g.cm^{-3}$ for proteins[214]. The relative density of Ly-AuNCs was found to be far more than the normal protein relative density, at a value of 1.87 $g.cm^{-3}$. This increase in relative density upon synthesising AuNCs within lysozyme is even greater than the increase seen for HSA-AuNCs in chapter 5. The only possible reason for the increase can only be attributed to the mass of AuNCs and possible excess gold salt attached to the protein surface,

since no other molecules were introduced to the samples after synthesis and dilution. All positively charged residues that make up the lysozyme primary structure are located on the protein surface. This gives the protein a highly positive surface charge making it likely that negatively charged chloride ions, created because of the gold salt reduction, are bound to the protein surface. The increase in density between lysozyme and Ly-AuNCs is 0.54 $g.cm^{-3}$. Attributing this value solely to the mass of gold, we can find that the average amount of gold atoms per lysozyme protein is 29 atoms. If every lysozyme present has an encapsulated AuNC then this value is close to the expected number of atoms within red emitting AuNCs at 25 atoms. The increase in amount of gold per lysozyme can be attributed again to unreacted gold salt on the protein surface, or it is possible that in some lysozyme smaller, AuNC intermediate products have formed which contain less gold atoms and are not fluorescent. Combining the molecular weights of Lysozyme and the added weight assuming it is that of the AuNCs then we can estimate that the molecular weight of Ly-AuNCs is 20,020 Da.

The dynamic viscosity of lysozyme and Ly-AuNCs was measured over a concentration range of 0 – 5,000 ppm to study the effects of the aggregation seen in previous experiments, as seen in Figure 6.6.

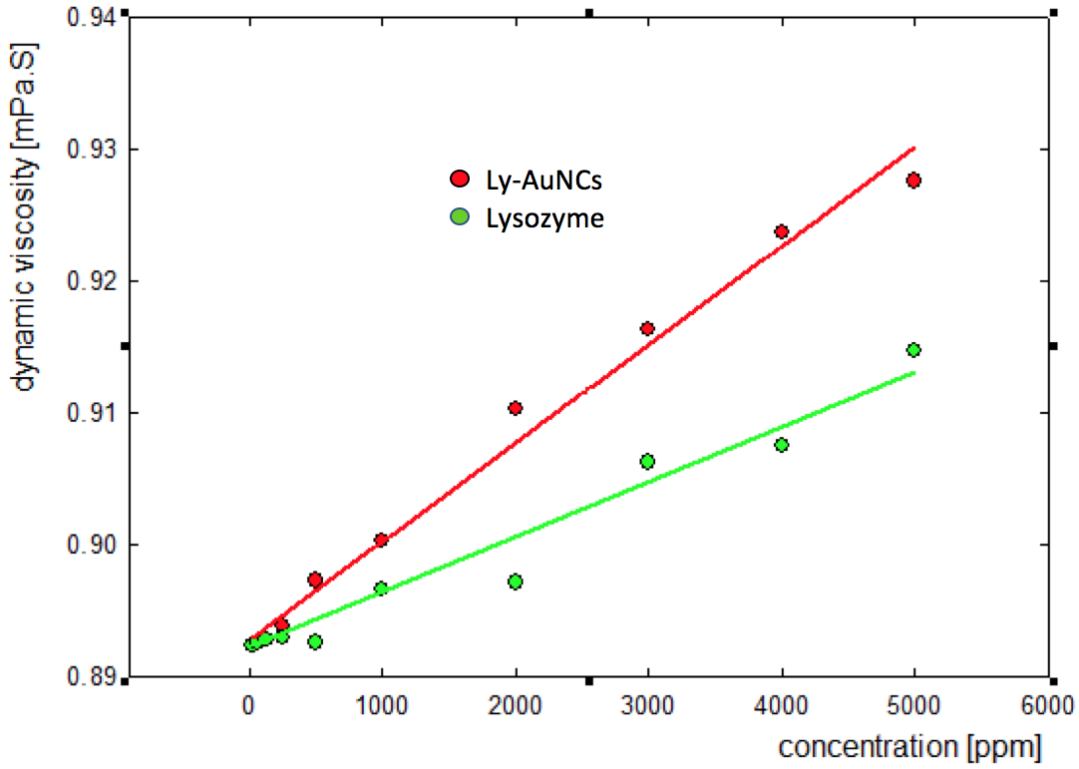

Figure 6.6: Dynamic viscosity of lysozyme and Ly-AuNCs as a function of concentration. The dynamic viscosity values for lysozyme are shown in green while Ly-AuNCs viscosity is shown in red.

The viscosity of Ly-AuNCs is considerably higher than that of lysozyme. The higher viscosity of Ly-AuNCs than that of natural lysozyme is unsurprising. This observation can be explained by the formation of dimers seen previously from the DLS experiment. In both cases the increase in viscosity in respect to the concentration was seen to be linear, suggesting that while the Ly-AuNCs viscosity is higher, it does not reach a critical viscosity at which the protein complex no longer flows in solution. The increase in viscosity for Ly-AuNCs can be attributed to a decrease in the rate of diffusion which arises due to the higher molecular weight of Ly-AuNCs.

6.4.3 Determining Ly-AuNCs Adsorption Characteristics

The adsorption of lysozyme and Ly-AuNCs to a gold surface was studied as a function of pH using QCM. A pH range of 4 - 10 was used in both cases at a constant sample concentration of 5 ppm. It was found that the presence of AuNCs had a major effect on the adsorption mass of Ly-AuNCs at different pH in comparison to natural lysozyme, shown in Figure 6.7.

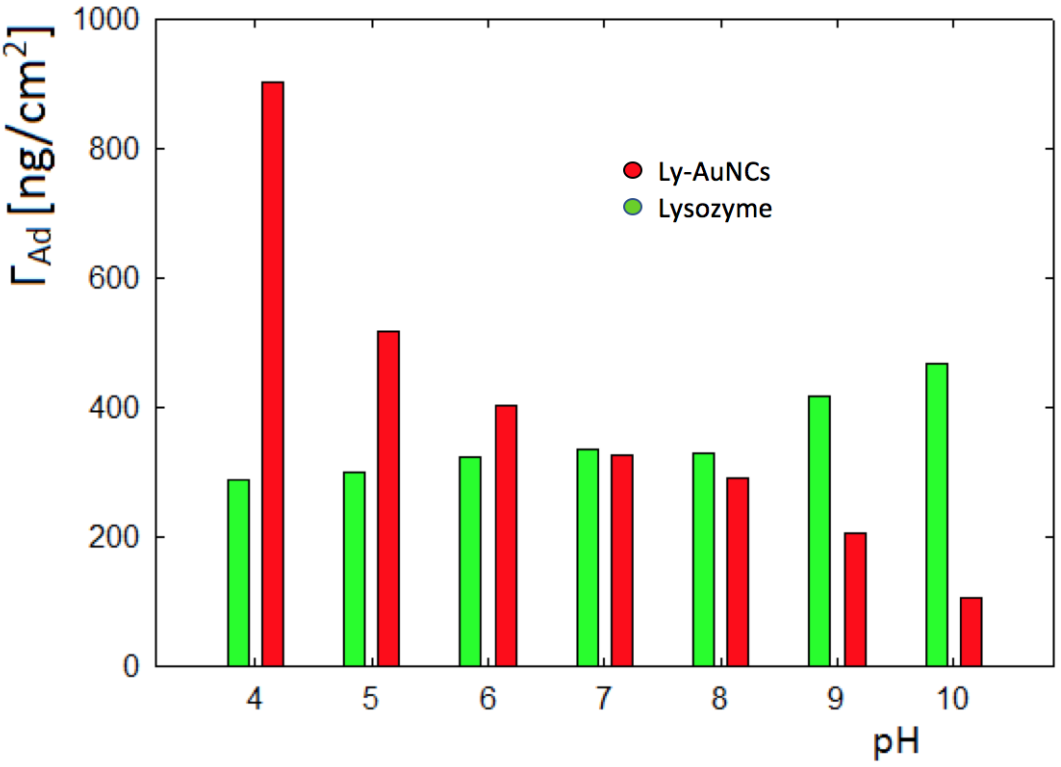

Figure 6.7: The mass of adsorbed molecules per geometrical unit of the gold surface, Γ_{Ad} [ng.cm^{-2}], as function of pH is shown. Lysozyme masses are represented in green while Ly-AuNCs are displayed in red.

The adsorption maxima for lysozyme and Ly-AuNCs are seen to be remarkably different. The adsorption maximum was found to be 900 ng.cm^{-2} at pH 4 for Ly-AuNCs while the adsorption maximum for lysozyme was found to be 450 ng.cm^{-2} at pH 10. The adsorption maxima in both cases occur at the isoelectric point for each molecule. Between pH 5 – 10 the adsorbed mass is seen to be relatively the same.

The higher adsorption of Ly-AuNCs at pH 4.0 can be attributed to aggregation effects earlier observed at this pH. The effectiveness of adsorption in both cases is directly linked to the overall magnitude of the charge, with the larger charge resulting in less effective adsorption. However, it is important to note that the polarity of the charge does not seem to be important for the adsorption to the gold surface to take place. This can be more effectively visualised by plotting the overall mass adsorbed in each case against the zeta potential, as shown in Figure 6.8.

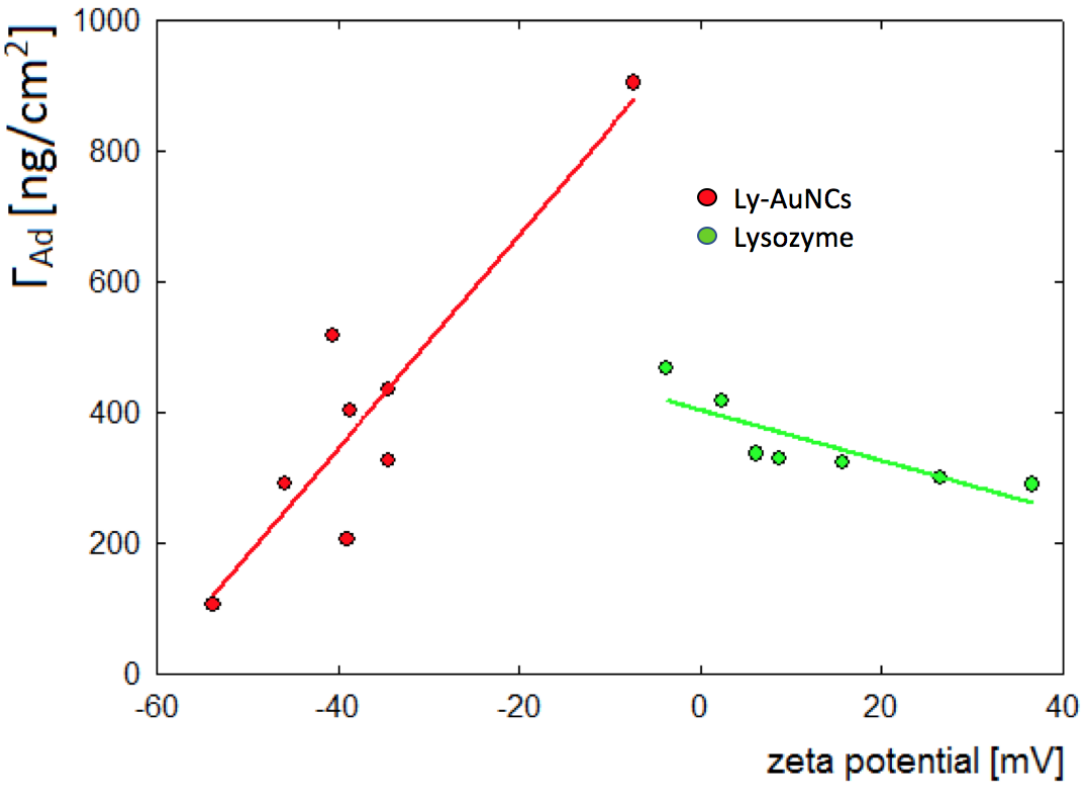

Figure 6.8: The mass of adsorbed molecules per geometrical unit of the gold surface, Γ_{Ad} [ng.cm^{-2}], as a function of pH is shown. The result for lysozyme is shown in green while Ly-AuNCs are displayed in red.

To better understand the effect of AuNCs on the adsorption of lysozyme the thickness of the adsorption layer formed on the gold surface was observed, seen in Figure 6.9.

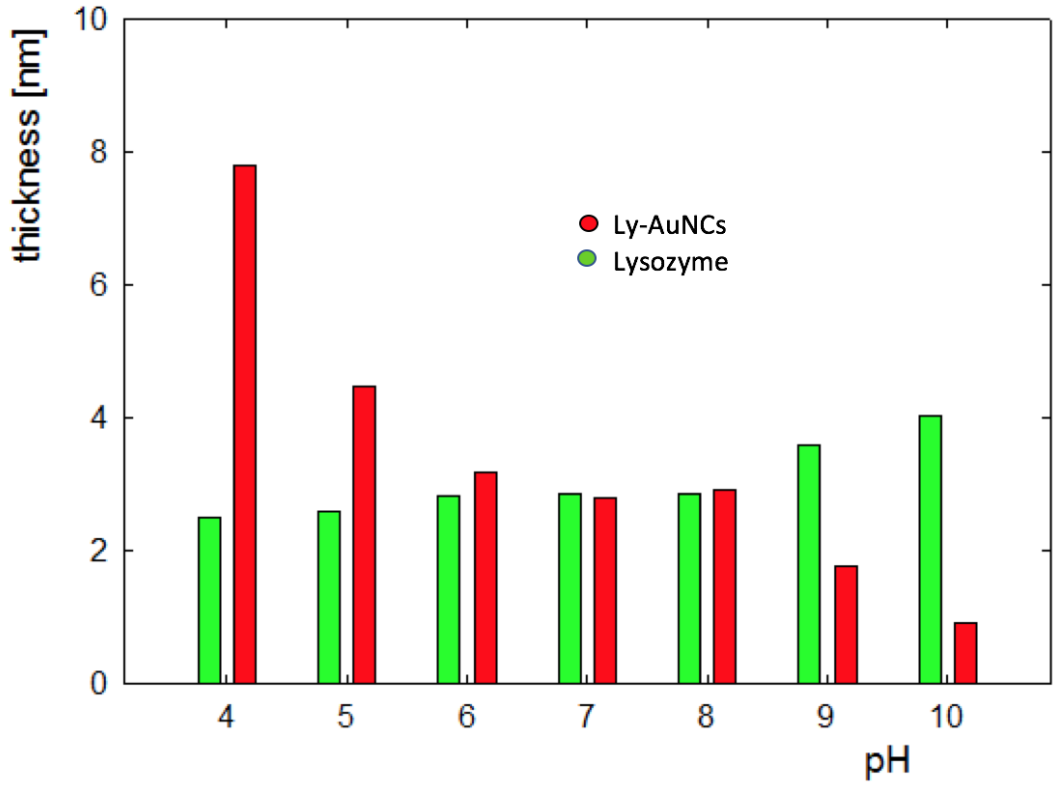

Figure 6.9: The thickness of the adsorbed layer as a function of pH on a gold surface is shown. The thickness of the lysozyme adsorption layer is shown in green while the thickness of Ly-AuNCs is shown in red.

It can be seen across the pH range that lysozyme forms layers with thicknesses between 2 - 4 nm. Ly-AuNCs can be seen to form layers with a much wider range of thicknesses from 1 - 8 nm. It is observed that the further from the molecules isoelectric point, the smaller the total mass adsorbed and the layer thickness, suggesting that the proteins at different pH contact and adsorb to the gold at different angles, with lower surface coverage being observed at lower layer thicknesses. In both cases the maximum thickness layer is equal to the hydrodynamic diameter found during the DLS experiments previous. The QCM result therefore suggests that at the isoelectric point in each case the proteins form tightly packed monolayers, with the proteins in a geometry that has a minimal amount of contact with the gold surface. This again suggests that the Ly-AuNCs exist in a small aggregated form, resulting in a thicker monolayer in comparison to natural lysozyme. This result

bodes well for the utilisation of Ly-AuNCs at body pH (7.4) as the adsorption behaviour of Ly-AuNCs and lysozyme have been seen to be similar in regards to total mass and thickness of monolayers adsorbed to a surface and while dimers have been seen from previous experiments, they do not negatively affect the proteins adsorption behaviour at neutral pH.

6.5 Conclusions

Important changes to the physicochemical characteristics of lysozyme upon the synthesis of AuNCs using the one-pot method to grow the AuNC within the protein have been observed. Lysozyme was seen to form small aggregates of dimer/trimer size upon the nucleation of AuNCs within the protein. The nature of these dimer/trimers formed requires further study. Aggregates were seen to be present across a pH range of 2 - 11 and larger reversible aggregation of the Ly-AuNCs was observed between pH 3 - 6. Between pH 3 - 6, studying the aggregation of lysozyme from its monomer form would of course not be possible, however there may be scope to study changes in the fluorescence emission of Ly-AuNCs as pH is slowly decreased and larger aggregates form. The reversible larger aggregates were confirmed to form due to the massive shift in the isoelectric point of lysozyme from 10 to 4. It is intriguing that the isoelectric point of both HSA-AuNCs and Ly-AuNCs is both around 4 despite the natural isoelectric points of both proteins being drastically different at 4.1 and 10 respectively. This suggests that an isoelectric point of 4 could be common for all other protein encapsulated AuNCs prepared using the one-pot method and that this shift in isoelectric point can been directly attributed to the formation of AuNCs within the protein. Questions remain however as to the reason of the common isoelectric point. From this Chapter and Chapter 5 it can be concluded the common isoelectric point is due to the presence of either unreacted gold salt, the by-products of the synthesis reaction or the AuNC inside the protein. Viscosity and density measurements of both lysozyme and Ly-AuNCs also suggested the formation of aggregates. QCM measurements of both Ly-AuNCs and lysozyme unveiled significant differences in the absorption behaviour of both molecules. The maximum absorptions of Lysozyme and Ly-AuNCs were found to take place at pH

10 and pH 4, respectively, explained by the massive shift in isoelectric point. The adsorption mass and layer thickness at neutral pH however was found to be near identical, suggesting that Ly-AuNCs characteristics may be similar enough that it is possible to utilise them as a fluorescent probe to track natural lysozyme aggregation.

7 Conclusions and Future Work

The work carried out in the thesis has added to the knowledge and understanding of protein encapsulated AuNCs. Understanding the location of AuNCs within serum albumin proteins and the effect it has on the sudlow I binding site (Chapter 3 and 4) has allowed for the development of intelligent strategies for the tailored modification of serum albumin encapsulated AuNCs. Following on from this body of work, studies have been carried out on the binding affinity of the Sudlow II major binding site, located in domain IIIA of the protein, using L-Dopa. Excitingly, it has been found that L-Dopa which has a strong binding affinity at this site still can bind HSA after the synthesis of AuNCs. The binding was tracked via a fluorescence decrease in L-Dopa emission upon binding at the site, as shown in Figure 7.1.

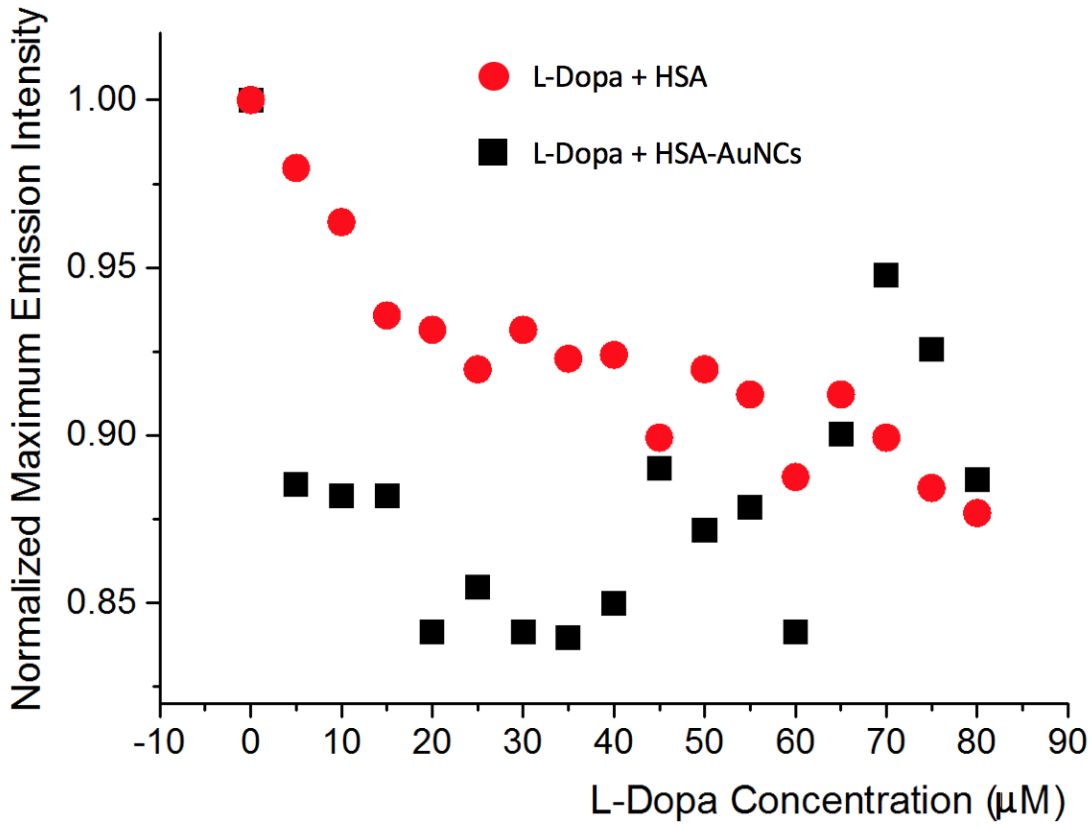

Figure 7.1: Normalised peak fluorescence intensity of L-dopa in solution with HSA (red) and L-dopa in solution with HSA-AuNCs (black). Excitation wavelength of 290 nm, emission wavelength of 325 nm.

The quenching in both cases agrees well with Yeggoni *et. al.*, indicating that L-dopa is bound to the Sudlow site II[229]. Thus, the synthesis of AuNCs within HSA does not hinder the binding affinity of this site. The increase in fluorescence intensity of HSA-AuNCs has been attributed to free dye in solution; since at 40 µm of L-dopa in solution the ratio between HSA protein and L-dopa should be 1:1 and is no longer binding once all available sites are taken. This is not the case with native HSA however, suggesting that other binding sites are available for L-dopa when AuNCs are not present within the protein. It was also found that AuNCs could be synthesised with L-Dopa prebound to the protein. The fluorescence intensity of the growing AuNCs was tracked over time during synthesis, shown in Figure 7.2.

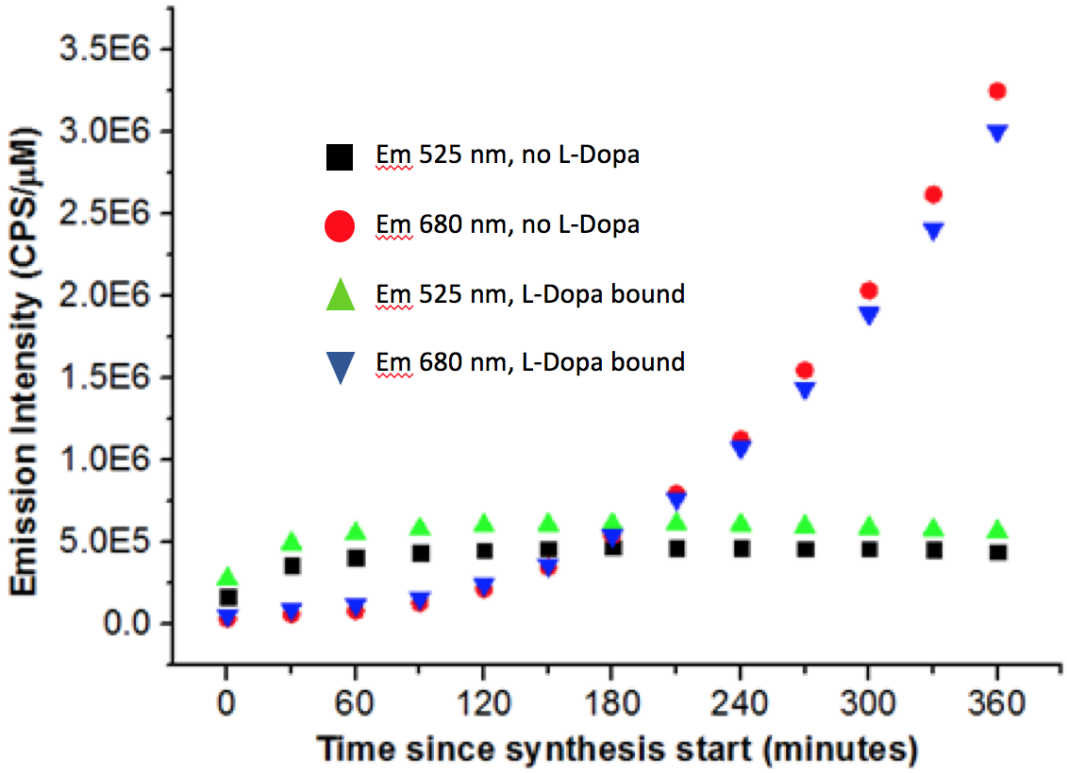

Figure 7.2: Peak fluorescence emission of HSA-AuNCs (with and without L-dopa pre-bound to HSA) during synthesis. Emission maximum of HSA-AuNCs at 525 nm (black) and at 680 nm (red). Emission maximum of L-dopa-HSA-AuNCs at 525 nm (green) and at 680 nm (blue). Excitation wavelength of 470 nm in all cases.

The availability of Sudlow site II is of upmost importance, as it offers an easily targeted site on the HSA protein which could be used as a means of functionalising the HSA-AuNC fluorophore for targeted sensing of molecules of interest. The ability of L-Dopa to freely bind to HSA is also interesting as it shows that despite the changes to the characteristics of HSA after AuNC synthesis, shown in Chapter 5, the functionality of the protein remains partially.

The observation that Ly-AuNCs do not form large aggregates after synthesis, shown in chapter 6, has already led to some interesting developments. The initial stages of lysozyme aggregation are still poorly understood due to the current fluorescence methods used to study protein aggregation. ThT has been typically used as a fluorescent probe for protein aggregation as its intensity dramatically increases upon binding between beta sheet formations; typically associated with protein aggregation. Since at the early stages of protein aggregation no beta sheets are formed, there is no fluorescence response from the ThT molecule. AuNCs are different to ThT as they behave like intrinsic fluorophores and the initial stages of aggregation affect their fluorescence intensity. Lysozyme aggregation induced via heating at 65 ºC results in the formation of large aggregates over a long period; however there is a lot of information which can be obtained in the early stages by AuNCs. Preliminary studies show that AuNCs have a much larger dynamic sensitivity to lysozyme aggregation both at the initial stages and over a longer period, in comparison to ThT, as shown in Figure 7.3.

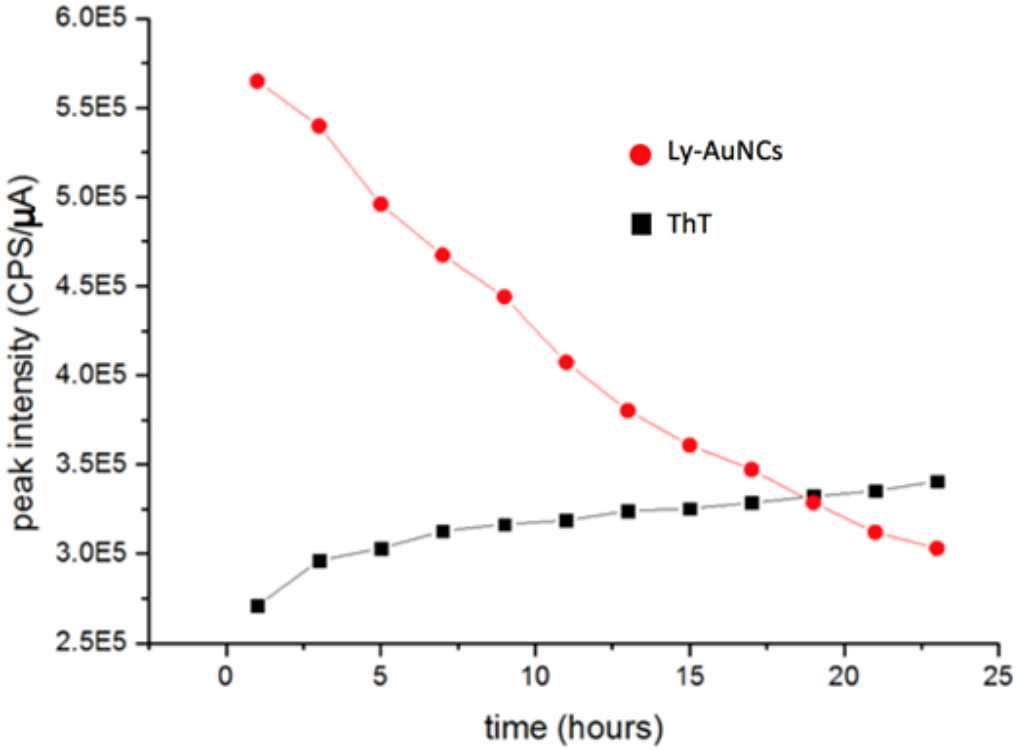

Figure 7.3: Heat induced aggregation (65 ^{0}C) of Ly-AuNCs. Fluorescence emission of ThT (ex 340 nm, em 380 nm) is shown in black, while AuNC emission is shown in red (ex 470 nm, em 670 nm).

The major difference is that AuNC emission is quenched during aggregation, whereas the ThT fluorescence is enhanced, however the dynamic range of AuNCs during aggregation is much larger and the brightness of the emission is initially much brighter allowing for the early stages to be probed. It is hoped that changes to the extremely long fluorescence lifetime of AuNCs could also be used to track the formation of lysozyme aggregates since it is concentration independent and as such could be used in low concentrations so that the natural aggregation path way is affected by AuNC presence in as small a manner as possible. The use of AuNCs to track protein aggregation could see wide use in the detection of amyloidosis type diseases in the future.

Other preliminary work has been undertaken to enhance the fluorescence brightness of HSA-AuNCs by rigidifying the structure using polymers to encapsulate the fluorophore complex. It has been observed that in the correct ratios of protein and

polymer, Polyallylamine hydrochloride (PAH), a positively charged polymer chain used in cell encapsulation, can enhance fluorescence emission brightness.

To summarize, there remains protein much potential for protein encapsulated AuNCs to be utilized as a fluorescent tool for many applications in the field of fluorescence imaging and spectroscopy.

8 References

1 L. A. Munishkina and A. L. Fink, *Biochim. Biophys. Acta - Biomembr.*, 2007, **1768**, 1862–1885.

2 F. Leblond, S. C. Davis, P. A. Valdes and B. W. Pogue, *J Photochem Photobiol B*, 2010, **98**, 77–94.

3 L. Bachmann, *Appl. Spectrosc. Rev.*, 2006, **41**, 575–590.

4 M. Kozubek and P. Matula, *J. Microsc.*, 2000, **200**, 206–217.

5 S. Bolte and F. P. Cordelieres, *J. Microsc.*, 2006, **224**, 13–232.

6 W. Manz, G. Arp, G. Schumann-Kindel, U. Szewzyk and J. Reitner, *J. Microbiol. Methods*, 2000, **40**, 125–134.

7 D. W. Cromey, *Cell Imaging Techniques*, 2013, vol. 931.

8 W. R. Zipfel, R. M. Williams, R. Christie, A. Y. Nikitin, B. T. Hyman and W. W. Webb, *Proc. Natl. Acad. Sci.*, 2003, **100**, 7075–7080.

9 C. P. Toseland, *J. Chem. Biol.*, 2013, **6**, 85–95.

10 M. Lippitz, W. Erker, H. Decker, K. E. van Holde and T. Basché, *Proc. Natl. Acad. Sci.*, 2002, **99**, 2772–2777.

11 R. Dixit, R. Cyr and S. Gilroy, *Plant J.*, 2006, **45**, 599–615.

12 Y. Fang and D. L. Spector, *Mol. Biol. Cell*, 2005, **16**, 5710–5718.

13 Y. S. Wang, C. M. Motes, D. R. Mohamalawari and E. B. Blancaflor, *Cell Motil. Cytoskeleton*, 2004, **59**, 79–93.

14 D. M. Gore, A. Margineanu, P. French, D. O'Brart, C. Dunsby and B. D. Allan, *Investig. Ophthalmol. Vis. Sci.*, 2014, **55**, 2476–2481.

15 V. Artym and K. Matsumoto, *Curr. Protoc. Cell Biol.*, 2010, 1–23.

16 S. Even-Ram and K. M. Yamada, *Curr. Opin. Cell Biol.*, 2005, **17**, 524–532.

17 A. W. Knight and N. Billinton, *Biophotonics Int.*, 2001, **8**, 42–50.

18 O. S. Wolfbeis, *Chem. Soc. Rev. Chem. Soc. Rev*, 2015, **44**, 4743–4768.

19 S. N. Baker and G. A. Baker, *Angew. Chemie - Int. Ed.*, 2010, **49**, 6726–6744.

20 S. Kochmann, T. Hirsch and O. S. Wolfbeis, *TrAC - Trends Anal. Chem.*, 2012, **39**, 87–113.

21 J. Shang, L. Ma, J. Li, W. Ai, T. Yu and G. G. Gurzadyan, *Sci. Rep.*, 2012, **2**, 792.

22 E. Petryayeva, W. R. Algar and I. L. Medintz, *Appl. Spectrosc.*, 2013, **67**, 215–252.

23 X. He, Z. Li, M. Chen and N. Ma, *Angew. Chemie - Int. Ed.*, 2014, **53**, 14447–14450.

24 J. Zhou, G. Chen, Y. Zhu, L. Huo, W. Mao, D. Zou, X. Sun, E. Wu, H. Zeng, J. Zhang, L. Zhang, J. Qiu and S. Xu, *J. Mater. Chem. C*, 2014, **3**, 364–369.

25 L. A. Dykman and N. G. Khlebtsov, *Chem. Rev.*, 2014, **114**, 1258–1288.

26 H. He, C. Xie and J. Ren, *Anal. Chem.*, 2008, **80**, 5951–5957.

27 I. Díez and R. H. A. Ras, *Nanoscale*, 2011, **3**, 1963–1970.

28 C. M. Li and S. N. Ding, *Anal. Methods*, 2015, **7**, 4348–4354.

29 J. Rao, A. Dragulescu-Andrasi and H. Yao, *Curr. Opin. Biotechnol.*, 2007, **18**, 17–25.

30 T. a Robertson, F. Bunel and M. S. Roberts, *Cells*, 2013, **2**, 591–606.

31 M. M. Pires and J. Chmielewski, *Org. Lett.*, 2008, **10**, 837–840.

32 X. Yang, C. Shi, R. Tong, W. Qian, H. E. Zhau, R. Wang, G. Zhu, J. Cheng, V. W. Yang, T. Cheng, M. Henary, L. Strekowski and L. W. K. Chung, *Clin. Cancer Res.*, 2010, **16**, 2833–2844.

33 M. Hassan, J. Riley, V. Chernomordik, P. Smith, R. Pursley, S. B. Lee, J.

Capala and A. H. Gandjbakhche, *Mol. Imaging*, 2012, **6**, 229–36.

34 B. Chazotte, *Cold Spring Harb. Protoc.*, 2011, **6**, 80–83.

35 R. M. Martin, H. Leonhardt and M. C. Cardoso, *Cytom. Part A*, 2005, **67**, 45–52.

36 F. Zhang, H. Zhong, C. Chen, X. G. Wu, X. Hu, H. Huang, J. Han, B. Zou and Y. Dong, *ACS Nano*, 2015, **9**, 4533–4542.

37 H. Kawasaki, K. Hamaguchi, I. Osaka and R. Arakawa, *Adv. Funct. Mater.*, 2011, **21**, 3508–3515.

38 M. L. Landry, T. E. Morrell, T. K. Karagounis, C. H. Hsia and C. Y. Wang, *J. Chem. Educ.*, 2014, **91**, 274–279.

39 A. Elsaesser and C. V. Howard, *Adv. Drug Deliv. Rev.*, 2012, **64**, 129–137.

40 M. Y. Berezin, W. J. Akers, K. Guo, G. M. Fischer, E. Daltrozzo, A. Zumbusch and S. Achilefu, *Biophys. J.*, 2009, **97**, L22–L24.

41 T. J. Sørensen, E. Thyrhaug, M. Szabelski, R. Luchowski, I. Gryczynski, Z. Gryczynski and B. W. Laursen, *Methods Appl. Fluoresc.*, 2013, **1**, 1–12.

42 M. Nasilowski, P. Spinicelli, G. Patriarche and B. Dubertret, *Nano Lett.*, 2015, **15**, 3953–3958.

43 K. Rurack and M. Spieles, *Anal. Chem.*, 2011, **83**, 1232–1242.

44 J. R. Lakowicz, H. Szmacinski, K. Nowaczyk and M. L. Johnson, *Proc. Natl. Acad. Sci. U. S. A.*, 1992, **89**, 1271–5.

45 Z. Y. Li, Y. T. Wu and W. L. Tseng, *ACS Appl. Mater. Interfaces*, 2015, **7**, 23708–23716.

46 H. Liu, Lund University, 2014.

47 L. Y. Chen, C. W. Wang, Z. Yuan and H. T. Chang, *Anal. Chem.*, 2015, **87**, 216–229.

48 Y. Negishi, Y. Takasugi, S. Sato, H. Yao, K. Kimura and T. Tsukuda, *J. Am. Chem. Soc. Commun.*, 2004, **38**, 6518–6519.

49 T. G. Schaaff and R. L. Whetten, *J. Phys. Chem. B*, 2000, **104**, 2630–2641.

50 Y. Negishi, K. Nobusada and T. Tsukuda, *J. Am. Chem. Soc.*, 2005, **127**, 5261–5270.

51 J. Xie, Y. Zheng and J. Y. Ying, *J. Am. Chem. Soc.*, 2009, **131**, 888–889.

52 A. R. Garcia, I. Rahn, S. Johnson, R. Patel, J. Guo, J. Orbulescu, M. Micic, J. D. Whyte, P. Blackwelder and R. M. Leblanc, *Colloids Surf. B. Biointerfaces*, 2013, **105**, 167–72.

53 X. Le Guével, N. Daum and M. Schneider, *Nanotechnology*, 2011, **22**, 275103.

54 X. Mu, L. Qi, P. Dong, J. Qiao, J. Hou, Z. Nie and H. Ma, *Biosens. Bioelectron.*, 2013, **49**, 249–55.

55 H. Wei, Z. Wang, L. Yang, S. Tian, C. Hou and Y. Lu, *Analyst*, 2010, **135**, 1406–1410.

56 M. Naldi, M. Baldassarre, M. Nati, M. Laggetta, F. A. Giannone, M. Domenicali, M. Bernardi, P. Caraceni and C. Bertucci, *J. Pharm. Biomed. Anal.*, 2015, **112**, 169–175.

57 L. Helmfors, A. Boman, L. Civitelli, S. Nath, L. Sandin, C. Janefjord, H. McCann, H. Zetterberg, K. Blennow, G. Halliday, A. C. Brorsson and K. Kågedal, *Neurobiol. Dis.*, 2015, **83**, 122–133.

58 L. M. Campbell, D. G. Dixon and R. E. Hecky, *A review of mercury in Lake Victoria, East Africa: implications for human and ecosystem health*, 2003, vol. 6.

59 N. Pirrone, S. Cinnirella, X. Feng, R. B. Finkelman, H. R. Friedli, J. Leaner, R. Mason, A. B. Mukherjee, G. B. Stracher, D. G. Streets and K. Telmer, *Atmos. Chem. Phys.*, 2010, **1010**, 5951–5964.

60 D. Hu, Z. Sheng, P. Gong, P. Zhang and L. Cai, *Analyst*, 2010, **135**, 1411–1416.

61 L. Shang, L. Yang, F. Stockmar, R. Popescu, V. Trouillet, M. Bruns, D. Gerthsen and G. U. Nienhaus, *Nanoscale*, 2012, **4**, 4155–4160.

62 S. Bothra, Y. Upadhyay, R. Kumar, S. K. Ashok Kumar and S. K. Sahoo, *Biosens. Bioelectron.*, 2017, **90**, 329–335.

63 C. V Durgadas, C. P. Sharma and K. Sreenivasan, *Analyst*, 2011, **136**, 933–940.

64 Y. S. Ho, H. L. Liu, J. S. Duh, R. J. Chen, W. L. Ho, J. H. Jeng, Y. J. Wang and J. K. Lin, *Mol. Carcinog.*, 1999, **26**, 201–211.

65 P. C. Pauly and D. A. Harris, *J. Biol. Chem.*, 1998, **273**, 33107–33110.

66 D. W. Domaille, L. Zeng and C. J. Chang, *J. Am. Chem. Soc.*, 2010, **132**, 1194–1195.

67 F. Wen, Y. Dong, L. Feng, S. Wang, S. Zhang and X. Zhang, *Anal. Chem.*, 2011, **83**, 1193–6.

68 Y. Liu, K. Ai, X. Cheng, L. Huo and L. Lu, *Adv. Funct. Mater.*, 2010, **20**, 951–956.

69 H. G. Gorchev and G. Ozolins, *WHO Chron.*, 2011, **38**, 104–108.

70 R. Kaushik, A. Ghosh, A. Singh, P. Gupta, A. Mittal and D. A. Jose, *ACS Sensors*, 2016, acssensors.6b00519.

71 X. Lou, Y. Zhang, J. Qin and Z. Li, *Sensors Actuators, B Chem.*, 2012, **161**, 229–234.

72 L. Hu, S. Han, S. Parveen, Y. Yuan, L. Zhang and G. Xu, *Biosens. Bioelectron.*, 2012, **32**, 297–299.

73 L. Tian, W. Zhao, L. Li, Y. Tong, G. Peng and Y. Li, *Sensors Actuators, B Chem.*, 2017, **240**, 114–124.

74 X. Zhang, F. G. Wu, P. Liu, N. Gu and Z. Chen, *Small*, 2014, **10**, 5170–5177.

75 H. Li, Y. Cheng, Y. Liu and B. Chen, *Talanta*, 2016, **158**, 118–124.

76 B. Valeur and M. N. Berberan-Santos, *J. Chem. Educ.*, 2011, **88**, 731–738.

77 S. E. Braslavsky, *Pure Appl. Chem.*, 2007, **79**, 293–465.

78 P. T. C. So and C. Y. Dong, *Encycl. Life Sci.*, 2002, 1–4.

79 S. P. Mulvaney, M. D. Musick, C. D. Keating and M. J. Natan, *Langmuir*, 2003, **19**, 4784–4790.

80 B. Valeur, *Molecular Fluorescence Principles and Applications*, 2001, vol. 8.

81 B. Nikoobakht and M. A. El-Sayed, *Chem. Mater.*, 2003, **15**, 1957–1962.

82 M. J. Holden, in *Standardization and Quality Assurance in Fluorescence Measurements II*, ed. O. Wolfbeis, 2008, vol. 6, pp. 489–508.

83 W. Smith, Z.-Y. Zhang and Y.-P. Zhao, *J. Vac. Sci. Technol. B Microelectron. Nanom. Struct.*, 2007, **25**, 1875.

84 S. J. Torkelson and Q. H. Gibson, 1978, **253**, 7331–7335.

85 R. J. Strasser, A. Srivastava and M. Tsimilli-Michael, *Probing Photosynthesis: Mechanism, Regulation and Adaptation.*, 2000, 443–480.

86 A. S. Kristoffersen, S. R. Erga, B. Hamre and Ø. Frette, *J. Fluoresc.*, 2014, **24**, 1015–1024.

87 N. Boens, W. Qin, N. Basaric, J. Hofkens, M. Ameloot, J. Pouget, J.-P. Lefevre, B. Valeur, E. Gratton, M. VandeVen, J. Silva, Norberto D., Y. Engelborghs, K. Willaert, A. Sillen, G. Rumbles, D. Phillips, A. J. W. G. Visser, A. van Hoek, J. R. Lakowicz, H. Malak, I. Gryczynski, A. G. Szabo, D. T. Krajcarski, N. Tamai and A. Miura, *Anal. Chem.*, 2007, **79**, 2137–2149.

88 D. Magde, R. Wong and P. G. Seybold, *Photochem. Photobiol.*, 2002, **75**, 327–34.

89 J. R. Albani, *J. Fluoresc.*, 2014, **24**, 93–104.

90 M. Sauer, J. Hofkens and J. Enderlein, in *Handbook of Fluorescence Spectroscopy and Imaging from Ensemble to Single Molecules*, Wiley-VCH, 2011, pp. 1–30.

91 T. a C. Kennedy, J. L. MacLean and J. Liu, *Chem. Commun. (Camb).*, 2012, **48**, 6845–7.

92 X. Le Guével, B. Hötzer, G. Jung, K. Hollemeyer, V. Trouillet and M. Schneider, *J. Phys. Chem. C*, 2011, **115**, 10955–10963.

93 L. E. Morrison, *Mol. Biotechnol.*, 2010, **44**, 168–176.

94 M. R. Eftink and C. A. Ghiron, *Radiat. Environ. Biophys.*, 1976, **15**, 672–680.

95 T. Markello, A. Zlotnick, J. Everett, J. Tennyson and P. W. Holloway, *Biochemistry*, 1985, **24**, 2895–2901.

96 S. C. Quay, A. Heropoulos, K. Commes and V. J. Dzau, *J. Biol. Chem.*, 1985, **260**, 15055–15058.

97 D. Silva, C. M. Cortez and S. R. W. Louro, *Spectrochim. Acta - Part A Mol. Biomol. Spectrosc.*, 2004, **60**, 1215–1223.

98 S. Faulkner and D. Sykes, in *Lanthanide Luminescence Photophysical, Analytical and Biological Aspects*, eds. P. Hanninen and H. Harma, Springer, 2011, vol. 7, pp. 161–182.

99 J. R. Lakowicz and G. Weber, *Biochemistry*, 1973, **12**, 4161–4170.

100 J. R. Lakowicz and G. Weber, *Biochemistry*, 1973, **12**, 4171–4179.

101 R. Ware, *Union Carbide Corp.*, 1962, **1**, 1949–1952.

102 W. M. Vaughan and G. Weber, *Biochemistry*, 1970, **9**, 464–473.

103 D. Andsager, J. Hilliard, J. M. Hetrick, L. H. Abuhassan, M. Plisch and M. H. Nayfeh, *J. Appl. Phys.*, 1993, **74**, 4783–4785.

104 B. Bakaeean, M. Kabiri, H. Iranfar, M. R. Saberi and J. Chamani, *J. Solution Chem.*, 2012, **41**, 1777–1801.

105 M. Royzen, Z. Dai and J. W. Canary, *J. Am. Chem. Soc.*, 2005, **127**, 1612–1613.

106 R. Giri, *Spectrochim. Acta - Part A Mol. Biomol. Spectrosc.*, 2004, **60**, 757–763.

107 C. D. Geddes, *J. Photochem. Photobiol. A Chem.*, 2000, **137**, 145–153.

108 D. B. Calhoun, J. M. Vanderkooi, G. V Woodrow III and S. W. Englander, *Biochemistry*, 1983, **22**, 1526–1532.

109 S.-H. Hong and W. Maret, *Proc. Natl. Acad. Sci. U. S. A.*, 2003, **100**, 2255–2260.

110 Y. Zhang, G. Wei, J. Yu, D. J. S. Birch and Y. Chen, *Faraday Discuss.*, 2015, **178**, 383–394.

111 C. Huitema and L. D. Eltis, *J. Biomol. Screen.*, 2010, **15**, 224–229.

112 J. C. Pickup, F. Hussain, N. D. Evans, O. J. Rolinski and D. J. S. Birch, *Biosens. Bioelectron.*, 2005, **20**, 2555–65.

113 I. H. Stein, V. Schüller, P. Böhm, P. Tinnefeld and T. Liedl, *ChemPhysChem*, 2011, **12**, 689–695.

114 S. S. Vogel, B. Wieb van der Meer and P. S. Blank, *Methods*, 2014, **66**, 131–138.

115 J. J. McCann, U. B. Choi, L. Zheng, K. Weninger and M. E. Bowen, *Biophys. J.*, 2010, **99**, 961–970.

116 S. A. Hussain, *Energy*, 2009, **132**, 1–4.

117 P. Held, *An Introduction to Fluorescence Resonance Energy Transfer (FRET) Technology and its Application in Bioscience*, 2012.

118 B. G. Abraham, K. S. Sarkisyan, A. S. Mishin, V. Santala, N. V. Tkachenko

and M. Karp, *PLoS One*, 2015, **10**, 1–15.

119 H. Sahoo, D. Roccatano, A. Hennig and W. M. Nau, 2007, **129**, 9762–9772.

120 T. Kato, H. Kashida, H. Kishida, H. Yada, H. Okamoto and H. Asanuma, *J. Am. Chem. Soc.*, 2013, **135**, 741–750.

121 P. C. Ray, Z. Fan, R. A. Crouch, S. S. Sinha and A. Pramanik, *Chem. Soc. Rev.*, 2014, **43**, 6370–404.

122 S. Preus and L. M. Wilhelmsson, *ChemBioChem*, 2012, **13**, 1990–2001.

123 J. W. Borst, S. P. Laptenok, A. H. Westphal, R. Kühnemuth, H. Hornen, N. V Visser, S. Kalinin, J. Aker, A. van Hoek, C. A. M. Seidel and A. J. W. G. Visser, *Biophys. J.*, 2008, **95**, 5399–5411.

124 R. Karoui and C. Blecker, *Food Bioprocess Technol.*, 2011, **4**, 364–386.

125 T. Deschaines, J. Hodkiewicz, P. Henson, *Application Note:51735*, Thermo Fisher Scientific, 2009.

126 M. Z. Bieroza, J. Bridgeman and A. Baker, *Drink. Water Eng. Sci.*, 2010, **3**, 63–70.

127 M. R. Siddiqui, Z. a. Al-Othman and N. Rahman, *Arab. J. Chem.*, 2013, **10**, 1409-1421.

128 R. S. Gabor, K. Eilers, D. M. McKnight, N. Fierer and S. P. Anderson, *Soil Biol. Biochem.*, 2014, **68**, 166–176.

129 M. J. Welsh and R. Fick, *J. Clin. Invest.*, 1987, **80**, 1523–1526.

130 A. C. V Mattar, E. N. Gomes, F. V Adde, C. Leone and J. C. Rodrigues, *J. Pediatr. (Rio. J).*, 2010, **86**, 109–114.

131 E. Urbano, H. Offenbacher and O. S. Wolfbeis, *Anal. Chem.*, 1984, **56**, 427–429.

132 B. P. Cosentino, B. Grossman, C. Shieh, S. Doi, H. Xi and P. Erbland, *J. Geotech. Eng.*, 1995, **121**, 610–617.

133 E. A. Nothnagel, *Anal. Biochem.*, 1987, **163**, 224–237.

134 M. Schmitt, *Macromol. Chem. Phys.*, 2011, **212**, 1276–1283.

135 Z. Li, C. Kübel, V. I. Pârvulescu and R. Richards, *ACS Nano*, 2008, **2**, 1205–1212.

136 A. Quaranta, D. J. McGarvey, E. J. Land, M. Brettreich, S. Burghardt, H. Schönberger, A. Hirsch, N. Gharbi, F. Moussa, S. Leach, H. Göttinger and R. V. Bensasson, *Phys. Chem. Chem. Phys.*, 2003, **5**, 843–848.

137 R. Thatipamala, G. A. Hill and S. Rohani, *Can. J. Chem. Eng.*, 1993, **71**.

138 F. L. S. Cuppo, S. L. Gómez and A. M. F. Neto, *Eur. Phys. J. E*, 2004, **13**, 327–333.

139 M. Andorn and K. H. Bar-Eli, *J. Chem. Phys.*, 1971, **55**, 5017–5021.

140 F. Peral and E. Gallego, *Spectrochim. Acta - Part A Mol. Biomol. Spectrosc.*, 2003, **59**, 1223–1237.

141 V. L. Singer, L. J. Jones, S. T. Yue and R. P. Haugland, *Anal. Biochem.*, 1997, **249**, 228–238.

142 Y. Yamashita and E. Tanoue, *Mar. Chem.*, 2003, **82**, 255–271.

143 M. A. H. Muhammed, P. K. Verma, S. K. Pal, R. C. A. Kumar, S. Paul, R. V. Omkumar and P. Thalappil, *Chem. - A Eur. J.*, 2009, **15**, 10110–10120.

144 M. Konishi, a Olson, S. Hollingworth and S. M. Baylor, *Biophys. J.*, 1988, **54**, 1089–1104.

145 W. W. Ward and S. H. Bokman, *Biochem. J. Physiol*, 1982, **21**, 4535–4540.

146 B. P. Wittmershaus, V. M. Woolf and W. F. Vermaas, *Photosynth. Res.*, 1992, **31**, 75–87.

147 M. Zhang, Y.-Q. Dang, T.-Y. Liu, H.-W. Li, Y. Wu, Q. Li, K. Wang and B. Zou, *J. Phys. Chem. C*, 2013, **117**, 639–647.

148 R. K. Henderson, a. Baker, K. R. Murphy, a. Hambly, R. M. Stuetz and S. J. Khan, *Water Res.*, 2009, **43**, 863–881.

149 H. L. Stewart, P. Yip, M. Rosenberg, T. J. Sørensen, B. W. Laursen, A. E. Knight and D. J. S. Birch, *Meas. Sci. Technol.*, 2016, **27**, 45007.

150 S. Raut, R. Chib, R. Rich, D. Shumilov, Z. Gryczynski and I. Gryczynski, *Nanoscale*, 2013, **5**, 3441–6.

151 C. Li, J. U. Sutter, D. J. S. Birch and Y. Chen, in *Proceedings of the IEEE Conference on Nanotechnology*, 2012, pp. 23–26.

152 G. Kresse and J. Furthmüller, *Phys. Rev. B*, 1996, **54**, 11169–11186.

153 M. G. Paterlini and D. M. Ferguson, *Chem. Phys.*, 1998, **236**, 243–252.

154 J. A. Lzaguirre, D. P. Catarello, J. M. Wozniak and R. D. Skeel, *J. Chem. Phys.*, 2001, **114**, 2090–2098.

155 H. P. Erickson, *Proc. Natl. Acad. Sci. U. S. A.*, 1994, **91**, 10114–10118.

156 I. Wagner and H. Musso, *Angew. Chemie Int. Ed. English*, 1983, **22**, 816–828.

157 J. B. F. Lloyd, in *Standards in Fluorescence Spectrometry Ultraviolet Spectrometry Group*, ed. J. N. Miller, Chapman and Hall, 1981, pp. 27–43.

158 C. M. Dobson, *Semin. Cell Dev. Biol.*, 2004, **15**, 3–16.

159 R. F. Chen, J. R. Knutson, H. Ziffer and D. Porter, *Biochemistry*, 1991, **30**, 5184–5195.

160 J. Qian, Y. Xu, S. Zhang and X. Qian, *J. Fluoresc.*, 2011, **21**, 1015–20.

161 A. S. Dvornikov, H. Zhang and P. M. Rentzepis, *J. Photochem. Photobiol. A Chem.*, 2009, **201**, 57–61.

162 M. R. Jones, R. J. Macfarlane, B. Lee, J. Zhang, K. L. Young, A. J. Senesi and C. a Mirkin, *Nat. Mater.*, 2010, **9**, 913–7.

163 M. a. a Islam, *Phys. Scr.*, 2004, **70**, 120–125.

164 M. Kaszuba, J. Corbett, F. M. Watson and A. Jones, *Philos. Trans. A. Math. Phys. Eng. Sci.*, 2010, **368**, 4439–51.

165 C. L. Nehl, N. K. Grady, G. P. Goodrich, F. Tam, N. J. Halas and J. H. Hafner, *Nano Lett.*, 2004, **4**, 2355–2359.

166 C. K. O'Sullivan and G. G. Guilbault, *Biosens. Bioelectron.*, 1999, **14**, 663–670.

167 M. Cassiède, J. Pauly, M. Milhet, M. Rivaletto, I. M. Marrucho, J. a P. Coutinho and J.-L. Daridon, *Meas. Sci. Technol.*, 2008, **19**, 65704.

168 S. K. Vashist and P. Vashist, *J. Sensors*, 2011, **2011**.

169 Z. A. Talib, Z. Baba, Z. Kurosawa, H. A. A. Sidek, A. Kassim and W. M. M. Yunus, *Am. J. Appl. Sci.*, 2006, **3**, 1853–1858.

170 P. Lee and X. Wu, *Curr Pharm Des*, 2015, **21**, 1862–1865.

171 B. X. Huang, H.-Y. Kim and C. Dass, *J. Am. Soc. Mass Spectrom.*, 2004, **15**, 1237–47.

172 D. M. Lavin, L. Zhang, S. Furtado, R. A. Hopkins and E. Mathiowitz, *Acta Biomater.*, 2013, **9**, 4569–4578.

173 M. L. Ferrer, R. Duchowicz, B. Carrasco, J. G. de la Torre and A. U. Acuña, *Biophys. J.*, 2001, **80**, 2422–30.

174 M. Dockal, D. C. Carter and F. Rüker, *J. Biol. Chem.*, 2000, **275**, 3042–3050.

175 A. K. Shaw and S. K. Pal, *J. Photochem. Photobiol. B Biol.*, 2008, **90**, 69–77.

176 S. S. Krishnakumar and D. Panda, 2002, 7443–7452.

177 S. M. Lystvet, S. Volden, G. Singh, M. Yasuda, Ø. Halskau and W. R. Glomm, *RSC Adv.*, 2013, **3**, 482–495.

178 Y. Tao, Y. Lin, J. Ren and X. Qu, *Biosens. Bioelectron.*, 2013, **42**, 41–46.

179 N.-Y. Hsu and Y.-W. Lin, *New J. Chem.*, 2016, **40**, 1155–1161.

180 L. Chen, P. Wang, J. Liu, B. Liu, Y. Zhang, S. Zhang and Y. Zhu, *J. Fluoresc.*, 2011, **21**, 765–73.

181 Y. Xu, J. Sherwood, Y. Qin, D. Crowley, M. Bonizzoni and Y. Bao, *Nanoscale*, 2014, **6**, 1515–24.

182 X. Wen, P. Yu, Y. R. Toh and J. Tang, *J. Phys. Chem. C*, 2012, **116**, 11830–11836.

183 S. Wang, X. Zhu, T. Cao and M. Zhu, *Nanoscale*, 2014, **6**, 5777–81.

184 D. Patra, N. N. Malaeb, M. J. Haddadin and M. J. Kurth, *J. Fluoresc.*, 2012, **22**, 707–17.

185 T. S. Figueiras, M. T. Neves-Petersen and S. B. Petersen, *J. Fluoresc.*, 2011, **21**, 1897–906.

186 A. K. Gaigalas and L. Wang, in *Standardization and Quality Assurance in Fluorescence Measurements II*, ed. O. Wolfbeis, 2008, vol. 6, pp. 371–398.

187 G. A. Evingur and Ö. Pekcan, *J. Fluoresc.*, 2011, **21**, 865–71.

188 H. Heinz, R. A. Vaia, B. L. Farmer and R. R. Naik, *J. Phys. Chem. C*, 2008, **112**, 17281–17290.

189 Y. Wang, H. Yu, X. Shi, Z. Luo, D. Lin and M. Huang, *J. Biol. Chem.*, 2013, **288**, 15980–15987.

190 X.-L. Cao, H.-W. Li, Y. Yue and Y. Wu, *Vib. Spectrosc.*, 2013, **65**, 186–192.

191 K. Yamasaki, V. T. G. Chuang, T. Maruyama and M. Otagiri, *Biochim. Biophys. Acta*, 2013, **1830**, 5435–5443.

192 O. K. Abou-Zied, *Curr. Pharm. Des.*, 2015, **21**, 1800–1816.

193 O. J. Rolinski, A. Martin and D. J. S. Birch, *J. Biomed. Opt.*, 2008, **12**, 34013.

194 G. Sudlow, D. J. Birkett and D. N. Wade, *Mol. Pharmacol.*, 1975, **11**, 824–832.

195 H. Mandula, J. M. R. Parepally, R. Feng and Q. R. Smith, *J. Pharmacol. Exp. Ther.*, 2006, **317**, 667–675.

196 I. Petitpas, A. A. Bhattacharya, S. Twine, M. East and S. Curry, *J. Biol. Chem.*, 2001, **276**, 22804–22809.

197 K. J. Fehske, W. E. Muller and U. Wollert, *Mol. Pharmacol.*, 1979, **16**, 778–789.

198 K. S. Joseph, A. C. Moser, S. B. G. Basiaga, J. E. Schiel and D. S. Hage, *J. Chromatogr. A*, 2009, **1216**, 3492–3500.

199 B. C. G. Karlsson, A. M. Rosengren, P. O. Andersson and I. A. Nicholls, *J. Med. Chem.*, 2010, **53**, 7932-7937 .

200 C. E. Petersen, C.-E. Ha, S. Curry and N. V Bhagavan, *Proteins*, 2002, **47**, 116–25.

201 B. C. G. Karlsson, A. M. Rosengren, P. O. Andersson and I. A. Nicholls, *J. Phys. Chem. B*, 2009, **113**, 7945–7949.

202 J. Liu, L. Lu, S. Xu and L. Wang, *Talanta*, 2015, **134**, 54–59.

203 V. Maes, Y. Engelborghs, J. Hoebeke, Y. Maras and A. Vercruysse, *Mol. Pharmacol.*, 1982, **21**, 100–107.

204 L. Trynda-Lemiesz and M. Luczkowski, *Bioinorg. Chem. Appl.*, 2003, **1**, 141–150.

205 A. M. Rosengren, B. C. G. Karlsson and I. A. Nicholls, *ACS Med. Chem. Lett.*, 2012, **3**, 650–652.

206 D. J. S. Birch, *Meas. Sci. Technol.*, 2011, **22**, 52002.

207 M. O. and J. H. P. J Wilting, W F van der Giesen, L H Janssen, M M Weideman, *J. Biol. Chem.*, 1980, **10**, 3032–3037.

208 R. V Rote, D. P. Shelar, S. R. Patil, S. S. Shinde, R. B. Toche and M. N. Jachak, *J. Fluoresc.*, 2011, **21**, 453–9.

209 Y. Yu, S. Y. New, J. Xie, X. Su and Y. N. Tan, *Chem. Commun. (Camb).*, 2014, **50**, 13805–8.

210 J. M. Park, B. B. Muhoberac, P. L. Dubin and J. Xia, 1992, **25**, 290–295.

211 J. M. Ruso, P. Taboada, L. M. Varela, D. Attwood and V. Mosquera, *Biophys. Chem.*, 2001, **92**, 141–53.

212 B. Jachimska, M. Wasilewska and Z. Adamczyk, *Langmuir*, 2008, **24**, 6866–6872.

213 B. Mali, A. I. Dragan, J. Karolin and C. D. Geddes, *J. Phys. Chem. C*, 2013, **117**, 16650–16657.

214 J. Tsai, R. Taylor, C. Chothia and M. Gerstein, *J. Mol. Biol.*, 1999, **290**, 253–66.

215 J. Vörös, *Biophys. J.*, 2004, **87**, 553–561.

216 P. C. DeRose, M. V. Smith, K. D. Mielenz, D. H. Blackburn and G. W. Kramer, *J. Lumin.*, 2009, **129**, 349–355.

217 G. D. O. Lowe, a. J. Lee, a. Rumley, J. F. Price and F. G. R. Fowkes, *Br. J. Haematol.*, 1997, **96**, 168–173.

218 V. Lebec, J. Landoulsi, S. Boujday, C. Poleunis, C. M. Pradier and a Delcorte, *J. Phys. Chem. C*, 2013, **117**, 11569–11577.

219 R. E. Canfield, *J. Biol. Chem.*, 1963, **228**, 2698–2707.

220 S. Leysen, J. M. Van Herreweghe, L. Callewaert, M. Heirbaut, P. Buntinx, C. W. Michiels and S. V. Strelkov, *J. Mol. Biol.*, 2011, **405**, 1233–1245.

221 Y. Lester, I. Ferrer, E. M. Thurman, K. a Sitterley, J. a Korak, G. Aiken and K. G. Linden, *Sci. Total Environ.*, 2015, **512**–**513**, 637–644.

222 C. M. Dobson, *Philos. Trans. R. Soc. Lond. B. Biol. Sci.*, 2001, **356**, 133–45.

223 D. R. Booth, M. Sunde, V. Bellotti, C. V Robinson, W. L. Hutchinson, P. E. Fraser, P. N. Hawkins, C. M. Dobson, S. E. Radford, C. C. Blake and M. B.

Pepys, *Nature*, 1997, 385, 787–793.

224 H.-D. Deng, G.-C. Li, Q.-F. Dai, M. Ouyang, S. Lan, V. a Trofimov and T. M. Lysak, *Nanotechnology*, 2013, **24**, 75201.

225 J. M. Bezemer, D. W. Grijpma, P. J. Dijkstra, C. A. Van Blitterswijk and J. Feijen, *J. Control. Release*, 1999, **62**, 393–405.

226 A. Valstar, W. Brown and M. Almgren, *Langmuir*, 1999, **15**, 2366–2374.

227 K. Kubiak-ossowska, B. Jachimska and P. A. Mulheran, *Phys. Chem. Chem. Phys.*, 2015, **17**, 1–20.

228 H. R. Ibrahim, A. Kato and K. Kobayashi, *J. Agric. Food Chem.*, 1991, **39**, 2077–2082.

229 D. P. Yeggoni and R. Subramanyam, *Mol. Biosyst.*, 2014, **10**, 3101-3110.